# THE MECHANICAL BEHAVIOR OF HIGH PERFORMANCE POLYMER FIBERS

by

JOHN EDWARD MOALLI

B.S. Civil Engineering
Northeastern University 1987

SUBMITTED TO THE DEPARTMENT OF
MATERIALS SCIENCE AND ENGINEERING
IN PARTIAL FULFILLMENT OF THE
REQUIREMENTS FOR THE DEGREE OF

DOCTOR OF SCIENCE

at the

MASSACHUSETTS INSTITUTE OF TECHNOLOGY

June 1992



Signature of Author _____
Department of Materials
Science And Engineering
May 1, 1992

Certified by _____
Professor Frederick J. McGarry
Thesis Supervisor

Accepted by _____
Linn W. Hobbs
Professor Of Materials Science
Chairman, Departmental Committee on Graduate Students

**The Mechanical Behavior of High Performance Polymer Fibers**

by

John E. Moalli

Submitted to The Department of Materials Science and Engineering on May 1, 1992 in partial fulfillment of the requirements for the Degree of Doctor of Science.

## Abstract

The mechanical behavior of high performance polymer fibers was investigated. In order to better characterize the mechanical properties of these fibers several novel test methods were developed and improvements were made on older ones. A device which simplifies fiber cutting for the tensile recoil test was constructed. A new method to evaluate the transverse strength index of single fibers has been devised. The index is found to be similar among a variety of fibers suggesting that lateral properties depend more on interfibrillar morphology than interchain properties. The same instrument can also be modified to perform three point bending tests on single fibers. This permitted the determination of flexural stiffness and compressive modulus. The compressive modulus is found to be considerably less than the tensile modulus for most high performance polymer fibers.

Compressive failure of high performance polymer fibers is modeled by buckling of fibril structural units. Using the compressive modulus from three point bending tests, fibril diameters from scanning electron microscopy and single mode fibril buckling lengths from several methods, Euler's equation is employed to predict the compressive strength of single fibers. Agreement with experimental data is reasonable and the model is shown to be especially useful for predicting relative compressive strength among fibers of similar composition subjected to different processing conditions.

Based on the modeling of fibril buckling initiating compressive failure, a new method is introduced to improve compressive strength in which rigid ceramic coatings are applied to the fiber exterior. Aluminum oxide coatings applied by physical vapor deposition are shown to increase compressive strength well beyond that predicted by a rule of mixtures. Alumina coatings also are shown to reduce the radial thermal expansion coefficient by a factor of two.

Thesis Supervisor: Frederick J. McGarry
Title: Professor of Materials Science and Engineering

Dedicated to the memory of my Grandfather,
Luciano Moalli
whose courage and ambition brought my family into this country, and whose morals and ethics will always be with me.

**Acknowledgments**

I would first like to thank Professor Frederick McGarry whose guidance, friendship and support made this work possible. The long discussions, often not related to science, and constant advice have had an influence on my professional development and character that cannot be measured. Many other faculty members are acknowledged for their input and advice, including but not limited to: Professor David Roylance, Professor Michael Rubner, and Professor Peggy Cebe.

For the financial support of Dow Chemical, and the fruitful discussions with its employees I am grateful. Many thanks to Dr. Steve Allen of DuPont for supplying Kevlar® and PPTA fibers, and for encouraging input on this work.

The staff at MIT has also been instrumental to the completion of this work: machining and design done by Arthur and Steven Rudolph was nothing short of spectacular and my time spent in their lab is most memorable. Mike Frongillo provided microscopy instruction and advice with humor and style that are unparalleled. Rich Perilli's help with PVD and equipment acquisition is greatly appreciated. John Martin provided great help in the surface lab. The constant help (and harassment) from Maria Raposo often pushed me over those barriers we all encounter.

And what would have I done without the UROP's ? Those who contributed substantially to this project are: Betty Chang, Amy Chiang, Maureen Fahey, Francis Lee, Rafy Levine, Troy Morrison, Rodrigo Rubiano, Shari Schuchmann and Becky Wittry. The company and friendship of UROP's on other projects is also recognized: Lynore Abbott, Nate Getrich, Mike Groleau, Daphne Karydas and Helen Shaugnessy. I would also like to thank the brothers of Phi Gamma Delta for their friendship.

My fellow graduate students have also provided help and friendship that was so important: Haskell Beckham, Francois Billaut, Jeff Carbeck, Mary Chan, Hans Foulger, Sue James, Sun-Wook Kim, Georgios Margaritis, Susan Noe, Ambuj Sagar, Ramnath Subramaniam and the entire PPST clan. There are many others who are not mentioned but are definitely remembered.

My most special friend, Shari, has provided unselfish love and friendship. The happiness and enjoyment she has added to my life have made MIT much more enjoyable.

Finally, my family must be acknowledged: Mom, Dad, Glenna, George, Grandma's, Michelle, Dan and Mary Ann, Maria, Pam and Mike, Andrea and Dave have always been there with support and love. Thank you all so much.

## List of Figures

## List of Tables

# Chapter 1. Introduction

High performance fibers are those described as having strength and moduli many times that of glass fibers. Almost since their inception, high performance polymer fibers have provoked much excitement: their tensile properties, combined with their low specific gravity, promise extraordinary benefits for structural composites, especially in mobile applications. The performance of many aircraft, missiles, land vehicles and boats could be measurably improved by using structural materials with higher specific properties. Unfortunately this has not proved out in practice; the low compressive strengths of the fibers have severely constrained their utility since relatively few structural components or systems function exclusively under tension.

Most high performance fibers are derived from rigid aromatic polymers. A few of the more common ones are illustrated in Figure 1-1: poly(p-phenylene benzobisoxazole), PBO; poly(p-phenylene benzobisthiazole), PBT; poly(p-phenylene-terepthalamide), PPTA. The former two are experimental fibers while the latter is produced by Dupont under the trade name Kevlar®. Extended chain poly (ethylene) has also been

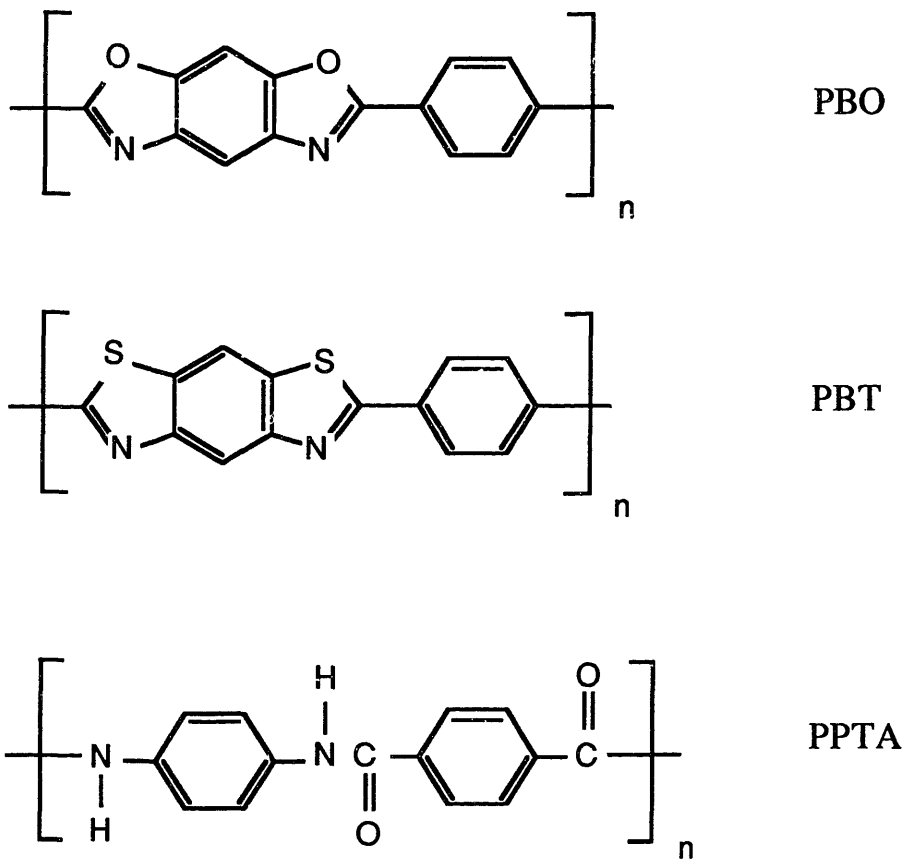


**Figure 1-1.** Aromatic Polymers Spun Into High Performance Fibers.

made into high performance fibers by Allied Signal under the trade name Spectra®.

The aromatic polymers form liquid crystalline solutions in strong solvents and are dry jet wet spun from these solutions at low concentrations into fibers. The alignment of chains during spinning results in fibers with a high degree of axial order[1]. Heat treatment under tension is then employed to further increase order and resultant properties. The aliphatic polymers are gel spun which results in extended chains and good axial alignment. All high performance polymer fibers display a unique fibrillar morphology, illustrated for the above systems in Figures 1-2 to 1-4 which are SEM micrographs of split fibers.

This fibrillar morphology leads to anisotropic mechanical behavior. Under axial tension, the fibers are very strong but under axial compression the fibrils buckle and form kink bands as shown in Figure 1-5. Since the fibrils are held together only by weak secondary forces, the lateral tensile strength of the fibers is also low. Axial chain alignment also manifests itself in anisotropic thermal expansion behavior: typically high performance polymer fibers have negative coefficients of thermal expansion in the axial direction and very large positive ones in the transverse

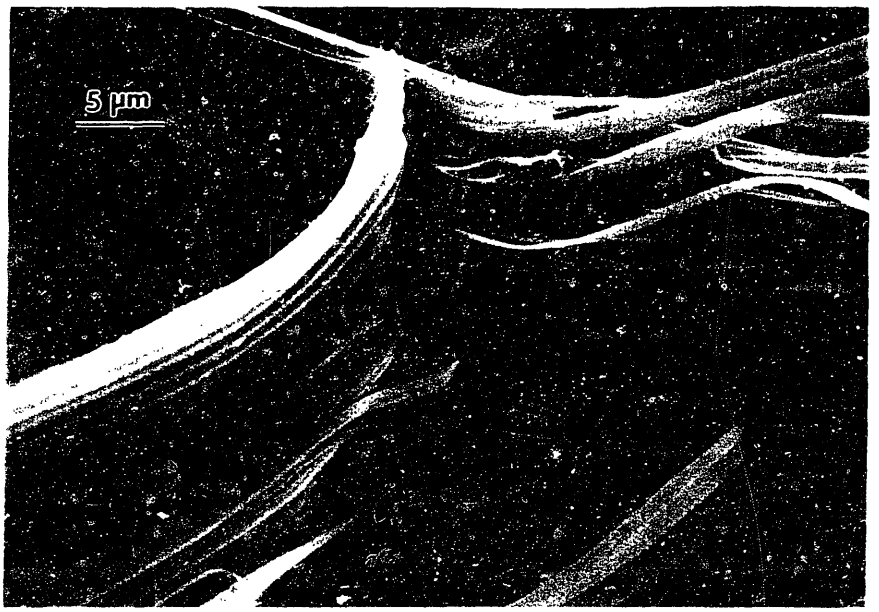


**Figure 1-2.** SEM Micrograph of Split PBO Fiber Showing Fibrillar Morphology in Fiber Interior.


**Figure 1-3.** SEM Micrograph of Split PPTA Fiber Showing Fibrillar Morphology in Fiber Interior.

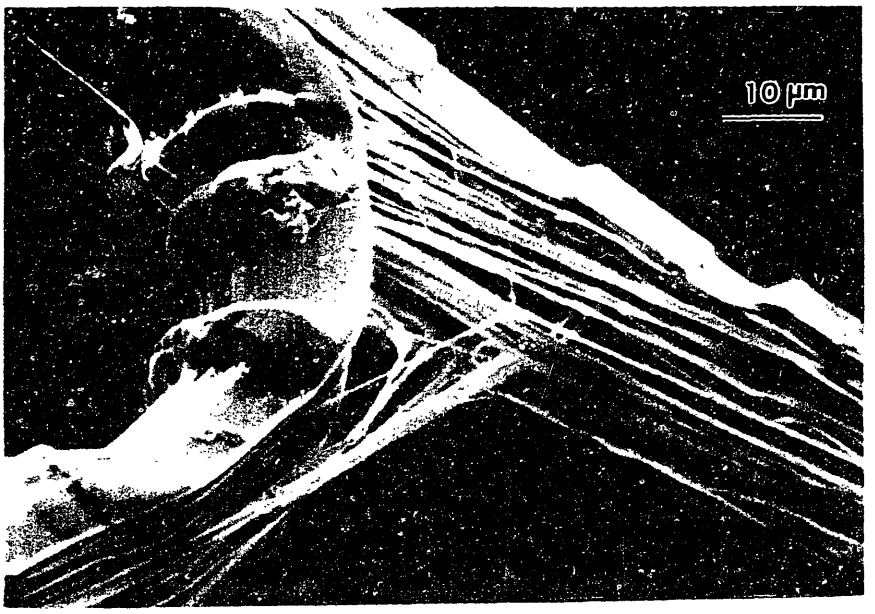


**Figure 1-4.** SEM Micrograph of Split Polyethylene Fiber Showing Fibrillar Morphology in Fiber Interior.

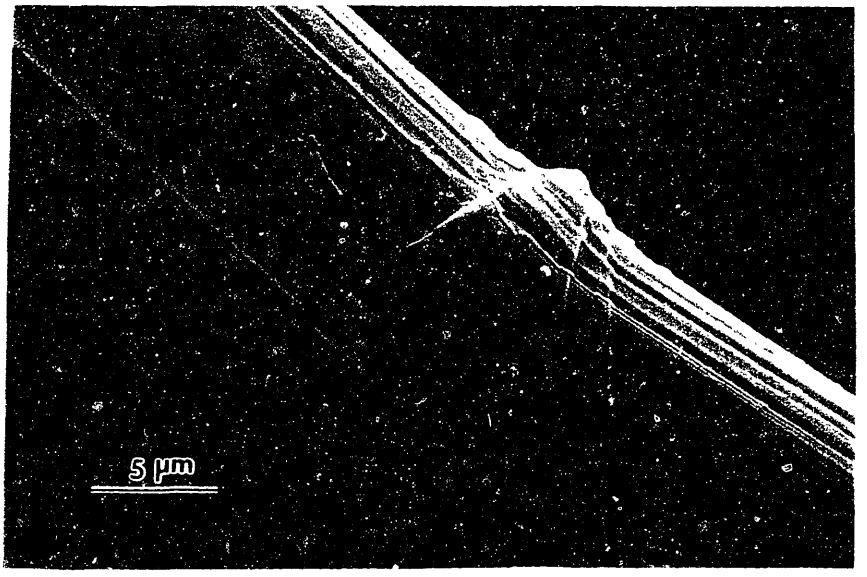


**Figure 1-5.** SEM Micrograph of Kink Band In PBO Fiber.

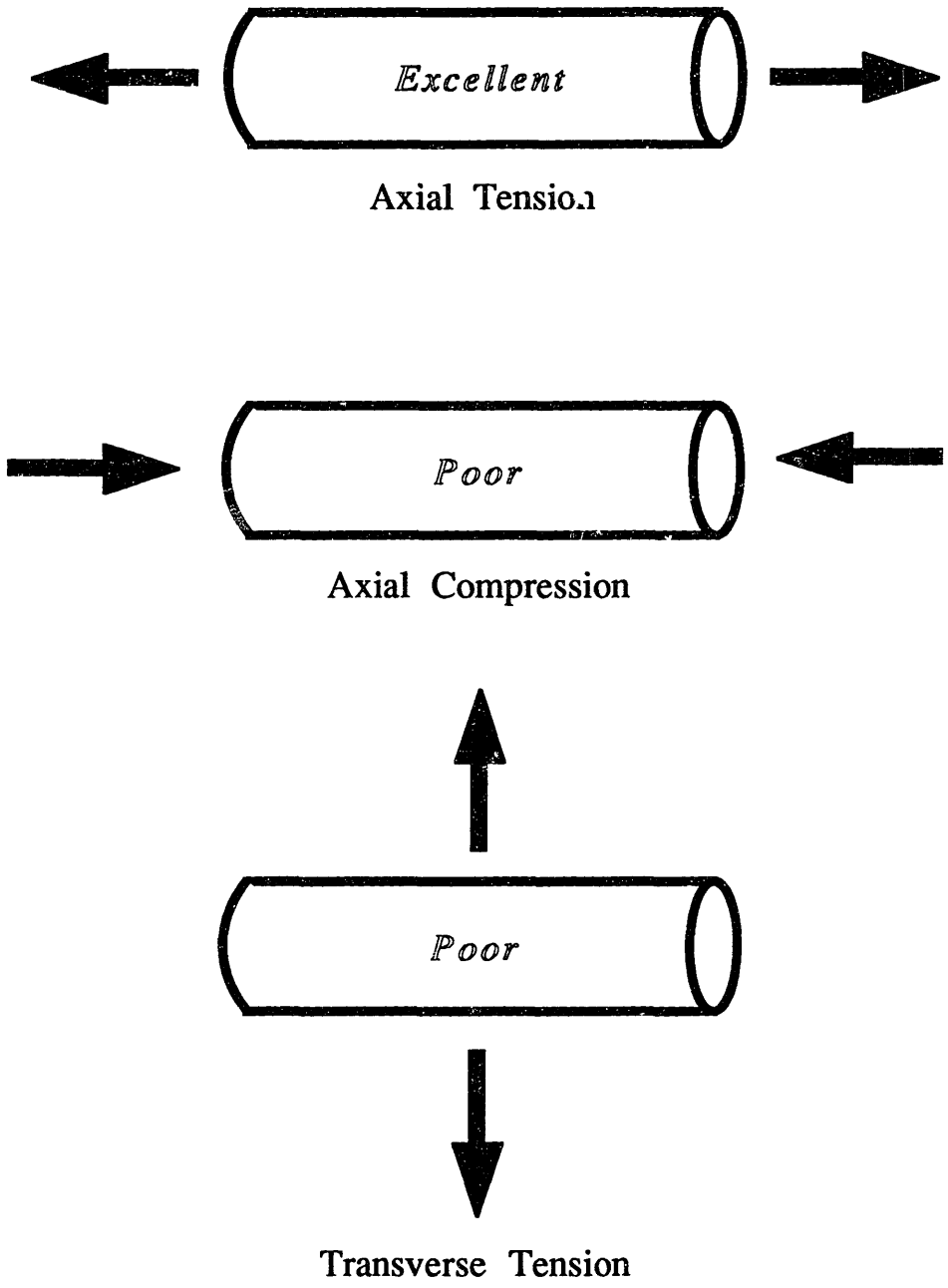


**Figure 1-6.** Anisotropy in Mechanical Behavior of High Performance Polymer Fibers

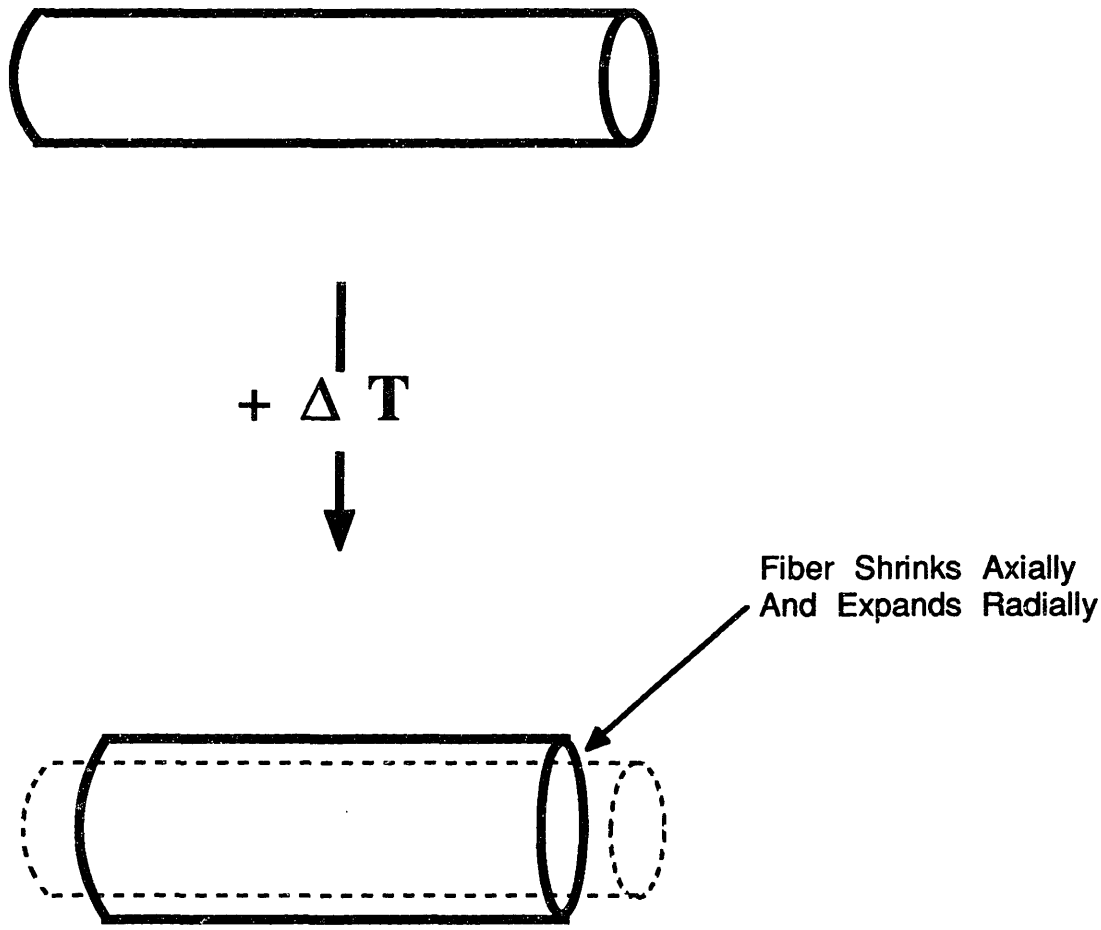


**Figure 1-7.** Anisotropy in Thermal Expansion Behavior of High Performance Polymer Fibers

direction. These anisotropic characteristics are schematized in Figures 1-6 and 1-7.

The need to correct this deficiency, to increase the axial compressive strength, has been apparent for some time, and many efforts to do so have been made. Principally these have been chemical in nature, seeking to provide primary bonding transversely across the fiber[2]. The motivating idea was, and still is, that if the axially aligned polymer chains could be crosslinked in some way, their resistance to compressive failure would be increased. (Implicit is the assumption that the failure mechanism is by buckling of the chain and, indeed, there have been attempts to quantitatively model the fiber behavior on this basis[3]) The crosslinks would laterally stabilize the chain and thereby increase its buckling load: the compressive strength of the fiber would improve. These attempts have not been very successful. Despite the apparent achievement of crosslinking, modest changes in fiber compressive strength have been reported often at the expense of tensile strength.

This research sought to elucidate the specific mechanism of compressive failure in high performance polymer fibers and find a way to delay it with the hope of discovering methods to produce fibers with less anisotropic mechanical properties. In Chapter 2, an overview of the anisotropic

elasticity resultant from the fiber microstructure is presented. In order to effectively assess any improvements in mechanical properties, methods had to be developed to evaluate them. Chapter 3 describes the measurement of mechanical properties of single fibers including axial compressive strength, lateral tensile strength and axial compressive modulus. Improvements on older test methods are made and some novel testing techniques are developed. Chapter 4 describes a new method of modeling the compressive failure of high performance fibers and correlates the model to measured properties. Based on observations of compressive failure and the modeling from Chapter 4, Chapter 5 introduces a new method to improve the compressive strength of high performance polymer fibers using rigid coatings on the fiber exterior. Effects of rigid coatings on the thermal expansion behavior of the fibers is also discussed. Chapter 6 highlights the findings of the research and makes suggestions for future work.

# Chapter 2. General Mechanical Behavior of High Performance Fibers

## 2.1. Anisotropic Elasticity

The fibrillar structure and axial chain alignment of high performance polymer fibers manifests itself in peculiar mechanical behavior. Loads applied axially to the fiber are carried by covalent bonds while those applied transversely are held by weaker secondary forces. If we examine a fiber in a polar coordinate system, one with r, $\theta$, and z axes as shown in Figure 2-1, it is not difficult to realize that the fiber will react differently to loads imposed on the r and z axes (transverse or axial loads). It is not entirely clear, however, if loads on the r and $\theta$ axes ( radial and hoop) will invoke dissimilar responses. If the r and $\theta$ planes behave identically, the system is said to be transversely isotropic. The more general case, though, is the orthotropic one, where the fiber possess symmetry with respect to three mutually orthogonal axes. These two systems produce very different responses to applied forces as described below. For a thorough discussion on this topic, the reader is referred to Allen[4].

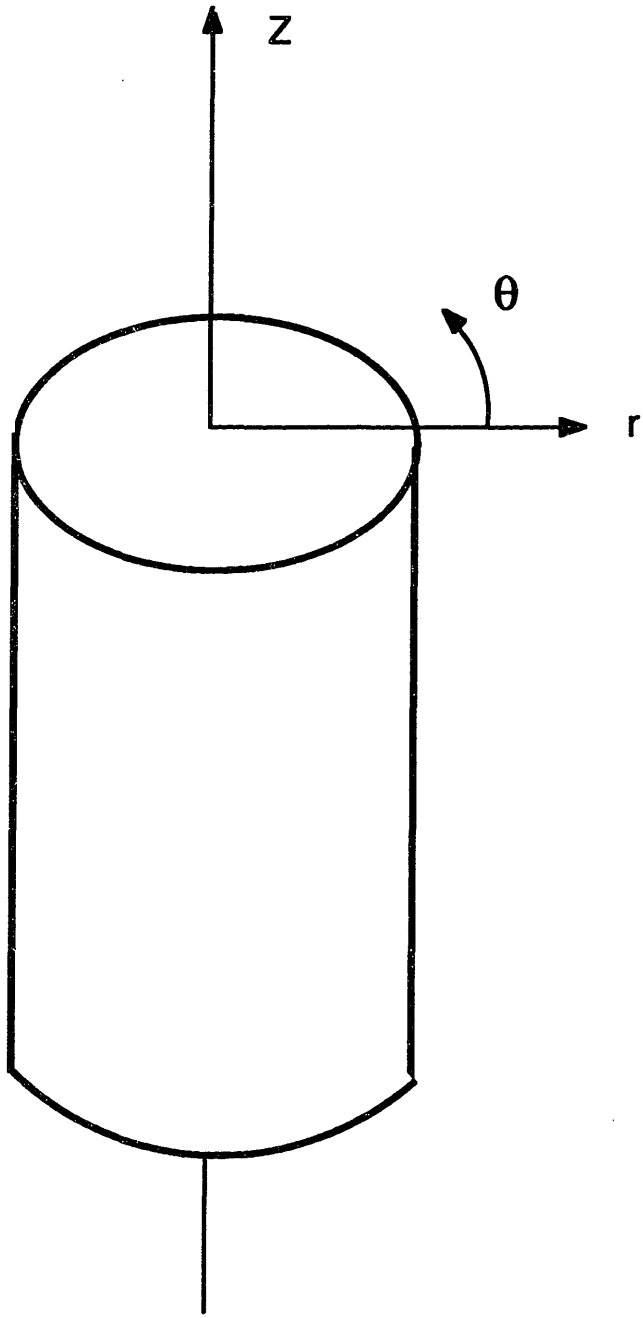


**Figure 2-1.** Polar Coordinates For A Single Fiber. Z=Axial, r=Radial and θ=Hoop directions.

### 2.1.1. The Cylindrically Orthotropic Fiber

A completely anisotropic material has 21 independent elastic constants. It can be shown that for the orthotropic case only 9 of these constants are independent. The stiffness matrix then becomes

$$\begin{pmatrix} E_{rr} & E_{r\theta} & E_{rz} & 0 & 0 & 0 \\ E_{r\theta} & E_{\theta\theta} & E_{\theta z} & 0 & 0 & 0 \\ E_{rz} & E_{\theta z} & E_{zz} & 0 & 0 & 0 \\ 0 & 0 & 0 & G_{\theta z} & 0 & 0 \\ 0 & 0 & 0 & 0 & G_{rz} & 0 \\ 0 & 0 & 0 & 0 & 0 & G_{r\theta} \end{pmatrix} \qquad (2.1)$$

where Eij's are the principal moduli. The presence of both rz and $\theta$z terms indicates that application of axial loads will produce radial and hoop stresses in the fiber. If the mechanical behavior of the system is based on chain forces only, then some systems will indeed be cylindrically orthotropic. Kevlar®, for example, has been shown to be composed of radially oriented hydrogen bonded sheets[5]. This implies that the radial direction stiffness would be related to hydrogen bonding, the hoop direction to Van Der Waals forces and the axial direction to covalent bonding; as the magnitudes of these interactions differ, an orthotropic system is the result.

### 2.1.2. The Transversely Isotropic Fiber

If mechanical behavior is based on fibril interactions, then the radial and hoop directions should be indistinguishable and the stiffness matrix becomes

$$\begin{pmatrix} E_{rr} & E_{r\theta} & E_{rz} & 0 & 0 & 0 \\ E_{r\theta} & E_{rr} & E_{rz} & 0 & 0 & 0 \\ E_{rz} & E_{rz} & E_{zz} & 0 & 0 & 0 \\ 0 & 0 & 0 & G & 0 & 0 \\ 0 & 0 & 0 & 0 & G & 0 \\ 0 & 0 & 0 & 0 & 0 & K \end{pmatrix} \qquad (2\text{-}1)$$

where $K = (E_{rr} - E_{r\theta})/2$, and only 5 independent constants exist. This type of model does not consider any differences in radial or hoop properties that may be derived from a skin/core structure in the fiber.

## 2.2. Consequences Of Anisotropic Elasticity

It has been shown[6] that a cylindrically orthotropic system will produce radial and hoop stresses when an axial load is applied. This implies that axial compression on a fiber may produce transverse tension, a combination of forces that is obviously detrimental to the fibrillar structure. For the transversely isotropic system, no coupling exists between axial and other directions. As will be evident in later Chapters, this research offers evidence that fibril interactions control mechanical behavior, hence all analysis are conducted assuming transverse isotropy in the fibers.

It must also be recognized that the fiber supramolecular structure (for example the pleated sheet arrangement in Kevlar®) can result in anisotropy in a single elastic constant depending on the sign of the applied load. Specifically, fibers may have different tensile and compressive moduli. This would imply that separate stiffness matrices would have to be compiled for tensile and compressive loadings.

# Chapter 3. Measurement of Fiber Mechanical Properties

## 3.1. Axial Compressive Strength

As described previously, rigid rod polymer fibers have low axial compressive strengths; several methods are available to measure this. Most of them mark failure by the onset of visible kink band formation. They include the elastica loop test[7], matrix shrinkage[8] and beam bending[3,9] . In these tests compressive strength is calculated from the product of the tensile modulus and the critical strain for kinking, thus it is assumed that the fiber behaves in a linear elastic fashion to compressive failure and that the tensile and compressive moduli are identical. These assumptions cause substantial uncertainty so a more direct measurement of single fiber axial compressive strength is desirable. The tensile recoil test developed by Allen is such a method[10]. Fibers are loaded in tension to various levels and then cut and the elastic recoil stresses created from tensile failure reflect from the grip surface and cause compressive damage in the fiber. It is assumed that no damping occurs during reflection such that the magnitude of the resulting compressive stress is equal to the tensile stress at failure. The compressive strength is determined by fracturing a number of tensile specimens at different stress levels to find the minimum value which just

initiates kink band formation. Obviously this requires tensile failure at different stress levels and several cutting techniques have been developed for the purpose. They include spot etching, heat cutting, prior localized mechanical damage, and scissor cutting[10]. Reproducibility in the first three is poor and scissor cutting induces undesirable increases in the applied stress because of the shearing action. A new device has been developed for symmetrical cutting of the fiber during recoil testing which gives a more accurate assessment of the axial compressive strength.

Another method which may be used to evaluate fiber compressive strength is by using composites. If sufficient fiber is available, a high quality composite can be made and compression tested. The composite must be free of voids which have been shown to substantially reduce compressive strength in unidirectional composites. Fiber alignment must also be perfect as strength and modulus decrease rapidly with increasing misalignment of fibers. If these conditions are met, the fiber compressive strength can be calculated using micromechanical theories, a method which has many disadvantages. Among the latter are matrix hardening and differential thermal shrinkage effects, differential Poisson's Ratio effects, specimen end friction and difficulty of perfect alignment. Also it is very difficult to monitor fiber compressive failure details in such assemblages,

compared to a single fiber specimen. Nonetheless, composite methods are desirable as they provide data for fiber properties during end use applications. Hence, a new method has been developed which allows for the construction of highly aligned void free composites for compression testing.

## 3.2. Transverse Strength

The transverse strength of rigid rod polymer fibers also is very low. Several researchers have measured the transverse strength by lateral compression of a single fiber[11] which produces tension on the midplane of the fiber. This procedure is shown in Figure 3-1. A major deficiency of this test is fiber crushing and the resultant frictional forces which are developed at the fiber base during deformation. Such forces tend to change the assumed stress state, a condition which is exacerbated by low lateral strength. Furthermore, the exact nature of load attenuation in the fiber is difficult to determine unless all of the fiber elastic constants are known. In order to avoid such effects it is desirable to perform lateral testing on free standing fibers. Therefore, a test has been developed in which an opening mode crack is propagated axially in high performance polymer fibers. The crack initiation force provides a measure of a transverse fiber mechanical property.

## 3.3. Compressive Modulus

The most common technique for evaluating fiber compressive modulus is with unidirectionally reinforced composites, usually with a thermosetting polymer matrix[12,13] . The fiber modulus is calculated through application of micromechanical theories to composite properties, a method which has many disadvantages as mentioned previously. Other researchers have used cantilever bending on large diameter fibers (250 - 500 um) to calculate fiber compressive modulus[14]. To the authors knowledge, no such flexural tests have been performed on high performance polymer fibers which typically have diameters from 10 um to 20 um. This research presents the development of a single fiber three point bending test for evaluation of fiber compressive modulus.

## 3.4. Experimental

### 3.4.1. Axial Compressive Strength

#### 3.4.1.1. Recoil Testing

The analysis of the tensile recoil test has been presented by Allen[10]. Since zero attenuation of the reflected wave is desirable and the amplitude of the reflected wave is given by

$$A_{refl} = A_{inc} \frac{(\rho_m c_m - \rho_f c_f)}{(\rho_m c_m + \rho_f c_f)} \qquad (3.1)$$

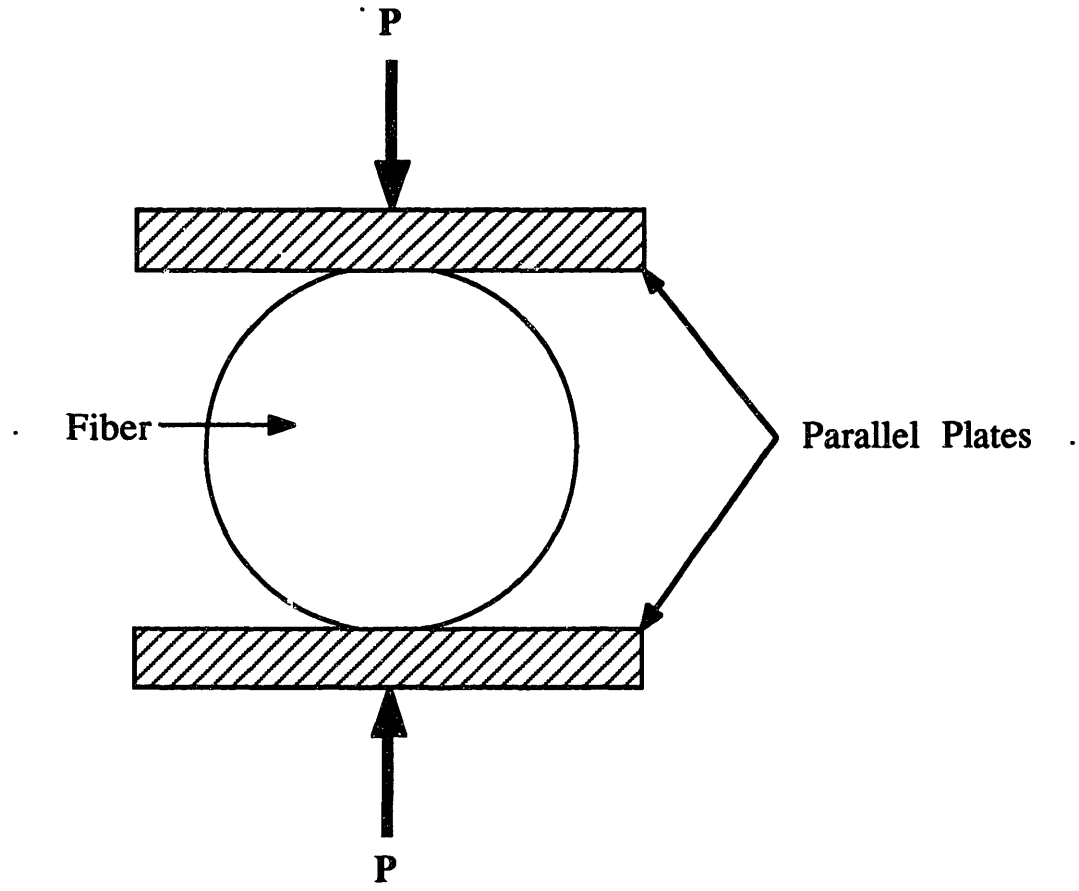


**Figure 3-1.** Lateral compression of a single fiber between parallel plates.

where the wave velocity, $c_i$ is

$$c_i = \sqrt{\frac{E_i}{\rho_i}}$$

and E is the modulus and $\rho$ is the density, it is obvious that the fiber and gripping medium must have different impedances. This is readily accomplished by placing the fiber ends in epoxy resin which typically has modulus values 40 to 80 times less than that of the fiber. The epoxy is used to mount the fibers onto cardboard tabs, the center of which is a hole of the desired gauge length. The fiber/tab assembly is placed in a tensile testing machine (Instron 4505 with 2000 g load cell at 20 g full scale load) and gripped. The edges of the tab are then cut away such that only the fiber is loaded.

The most difficult part of the test is finding a suitable method to cause tensile failure in the fibers. If breaking is not done with great care, large increases (spikes) in the applied load will occur. If the spikes are too large, the test is invalid because the exact stress state in the fiber becomes unknown. Although some researchers have found that surgical scissors can provide reasonable reproducibility, problems exist with this technique. The blades cut by a shearing action, and as shown schematically in Figure 3-2, this imposes a twist on the fiber causing an increase in the applied load. Another problem arises when the blades do not cut symmetrically: both blades do not come in contact with

the fiber at the same time. The fiber is displaced laterally, as shown in Figure 3-3, which also causes a spike in the load. Both of these effects are more pronounced as the fiber modulus increases.

To remedy these problems a device named FI-RE-CUT (FIber-REcoil-CUTter) was made, a photograph of which is shown in Figure 3-4. It employs scalpel blades mounted on blocks which are supported by linear bearings. The blades remain co-planar, avoiding any shearing action. The blocks are connected to a drive rod with opposing left and right handed threads; when the rod is rotated it brings the blades together smoothly at a uniform rate. The entire device is mounted on a micrometer substage which facilitates precision centering of the fiber between the blades and prevents unsymmetrical cutting.

### 3.4.1.2. Composite Testing

The method developed for composite manufacture, similar to that of Piggot[13] is a pultrusion technique. Four inch lengths of fibers were cut and placed on top of a small wire. After a sufficient number of fibers were in place the wire was looped over the fibers which were pulled by the wire into a hollow glass tube of 20 mm diameter. A smaller glass tube (5 mm) lined with rubber was then placed over the wire just above the fibers. Next, epoxy resin (Dow Tactix 123) was

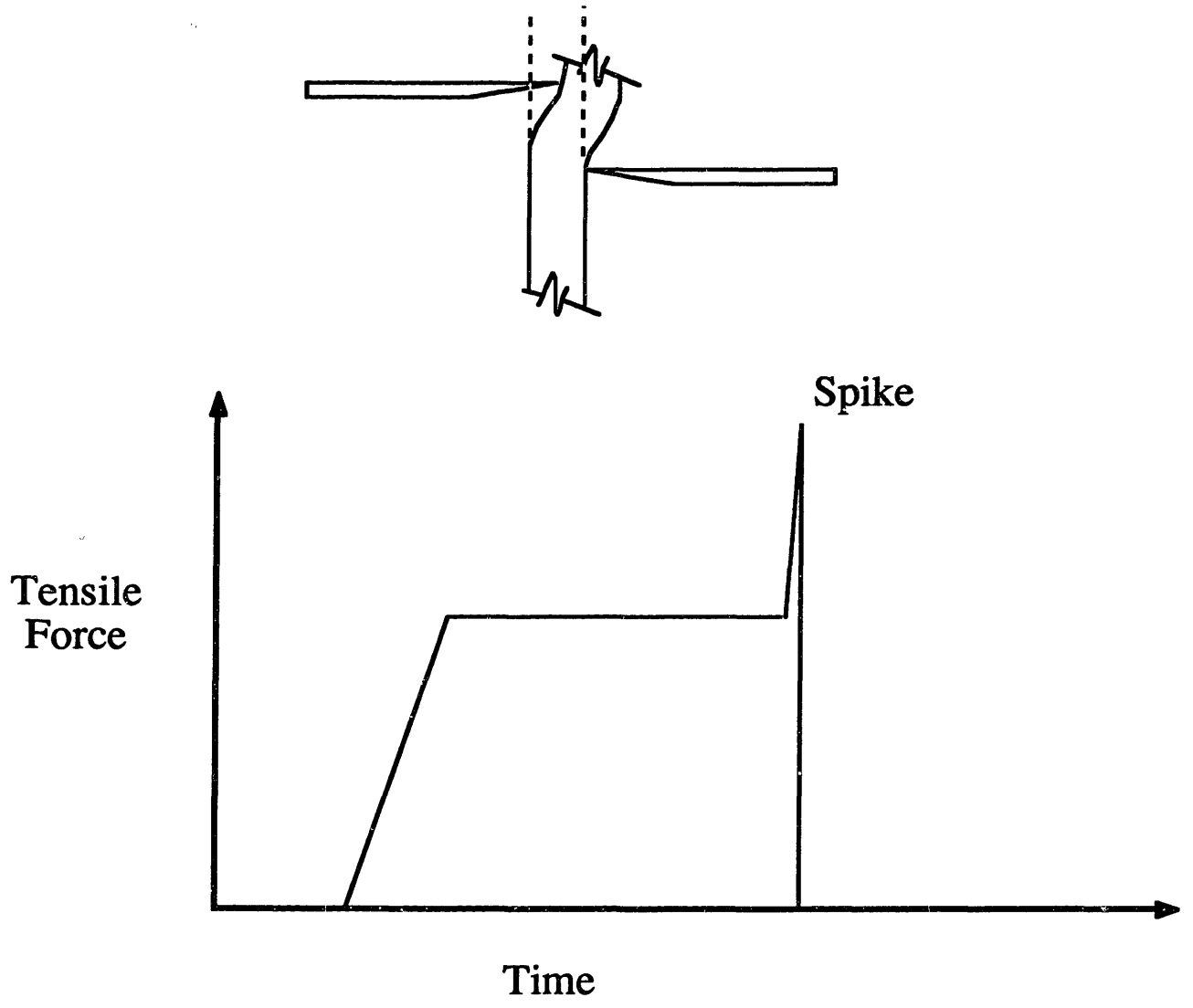


**Figure 3-2.** Schematic of Spike in Load During Tensile Recoil Testing Caused by Shearing Action of Scissors.

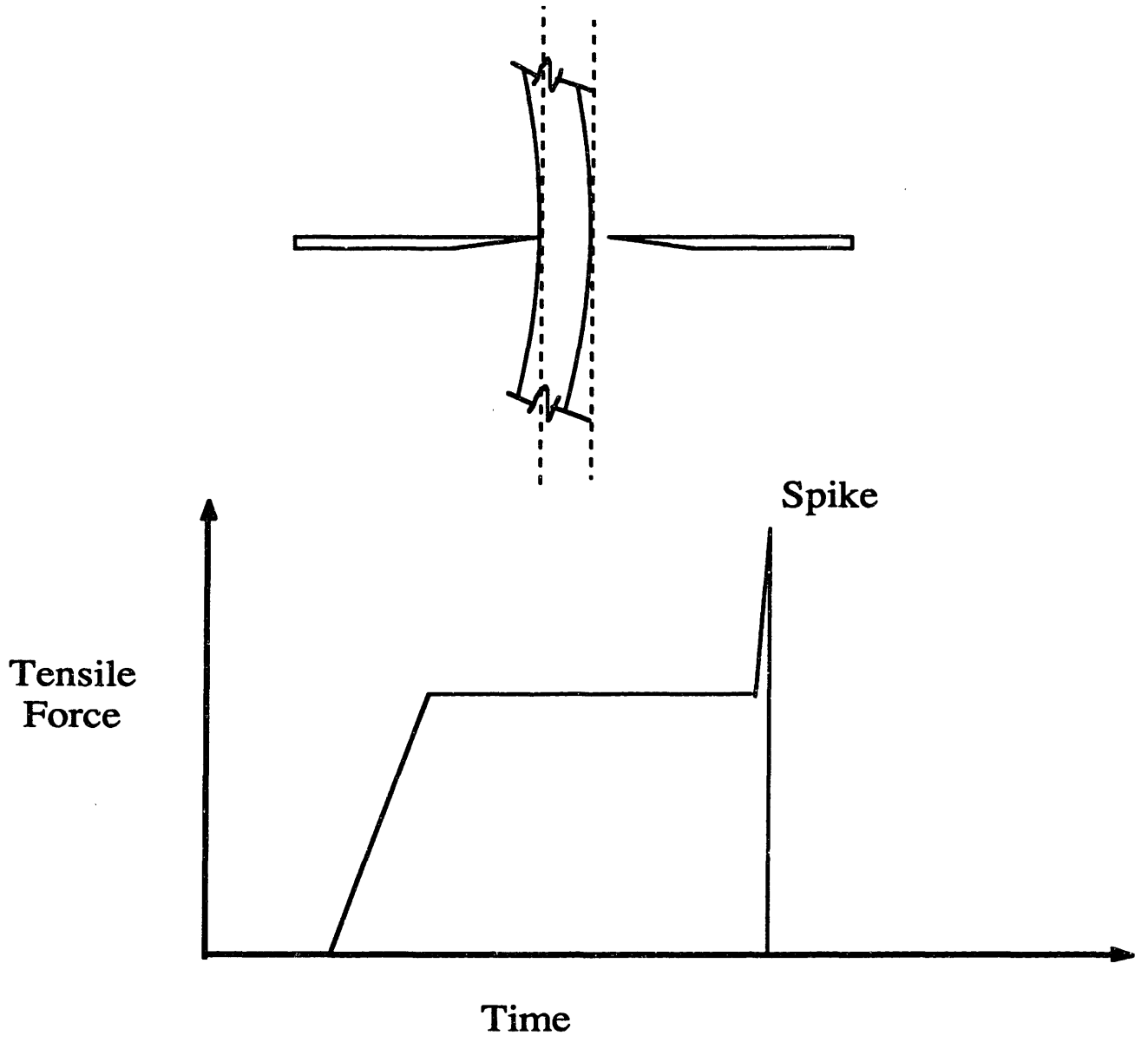


**Figure 3-3.** Schematic of spike in load during tensile recoil testing caused by unsymmetrical cutting.

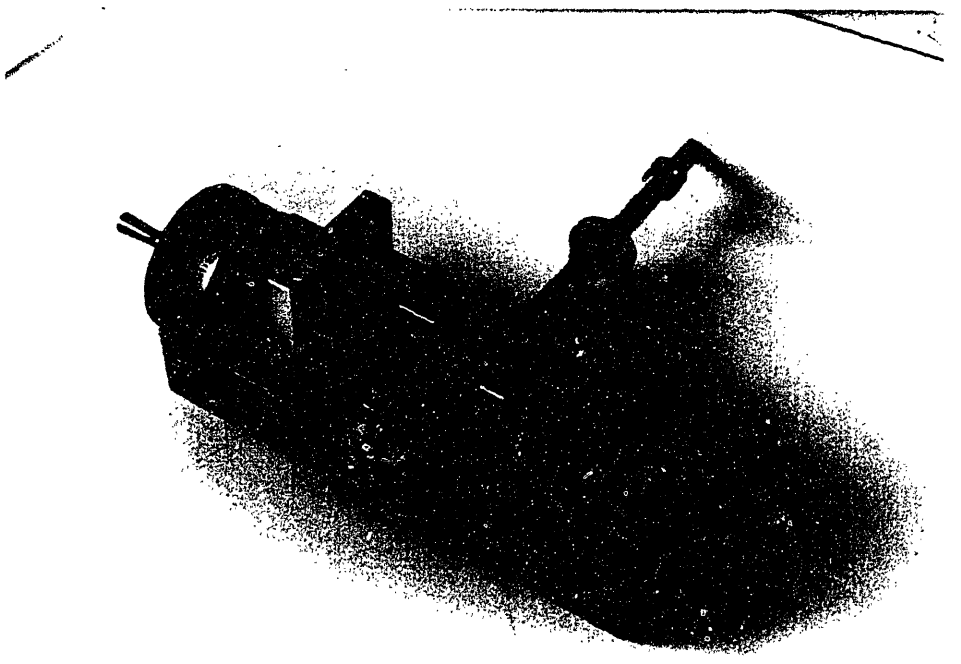

**Figure 3-4.** Photograph of FI-RE-CUT device.

poured into the large tube over the fibers and the entire assembly (Figure 3-5) placed in a vacuum oven. After degassing, the resin soaked fibers were pulled through the small glass tube and cured. Void free, high fiber volume fraction composites were produced using this method. A cross section of a typical composite is shown in Figure 3-6.

Composites were cut to 12.5 mm lengths with a diamond saw in a specially designed jig to ensure that specimens ends were parallel. Specimens were loaded unsupported, end on, in direct compression in an Instron 4505 at a crosshead speed of 1 mm/min. Teflon was placed between the loading platens and the specimen ends to minimize frictional end constraints.

### 3.4.2. Transverse Strength

The poor lateral integrity of rigid rod polymer fibers makes them susceptible to damage from handling. It was observed that a fiber of circular cross section could easily be flattened with tweezers or other instruments. Then if the end was split, the force required could give some idea of the transverse strength. Using a micromanipulator , one end of a fiber which is a few centimeters in length is flattened. A vee shaped segment is removed defining two ligaments (usually this operation is easily performed on the rigid rod polymer fibers because of their high orientation and directionality; with other less oriented fibers such as nylon it may be more difficult). This whole procedure is sketched

in Figure 3-7 and, experimentally, such specimens have been made with a micromanipulator. An optical micrograph is shown in Figure 3-8. The loads involved in splitting fibers are extremely small and difficult to measure. To determine the critical crack propagating force an instrument which operates with dead weights has been constructed; a schematic is shown in Figure 3-9 and photographs are given in Figures 3-10 and 3-11. The operation is quite simple: one ligament of the notched fiber is placed in a fixed grip and the other in a movable grip (it is necessary to keep the axis of the fiber specimen approximately perpendicular to the line defined by the two grips and the weighing cable, to ensure successful splitting of the fiber). The moveable grip is supported by a gas bearing which eliminates friction effects. Attached to the movable grip is a cable running over a gas bearing supported shaft. The cable ends at a bucket in which the weights are placed. [Since the loads required for crack propagation are in the milligram range, the gas bearings are critical: frictional forces in conventional bearings easily exceed the loads of the test.] To balance the system before testing, the entire device is slightly elevated on the right end causing the movable grip to displace to the left. Weights are added until the movable grip is in a neutral position. Then the fiber is inserted into the grips and more weights are added until the fiber splits. The entire test

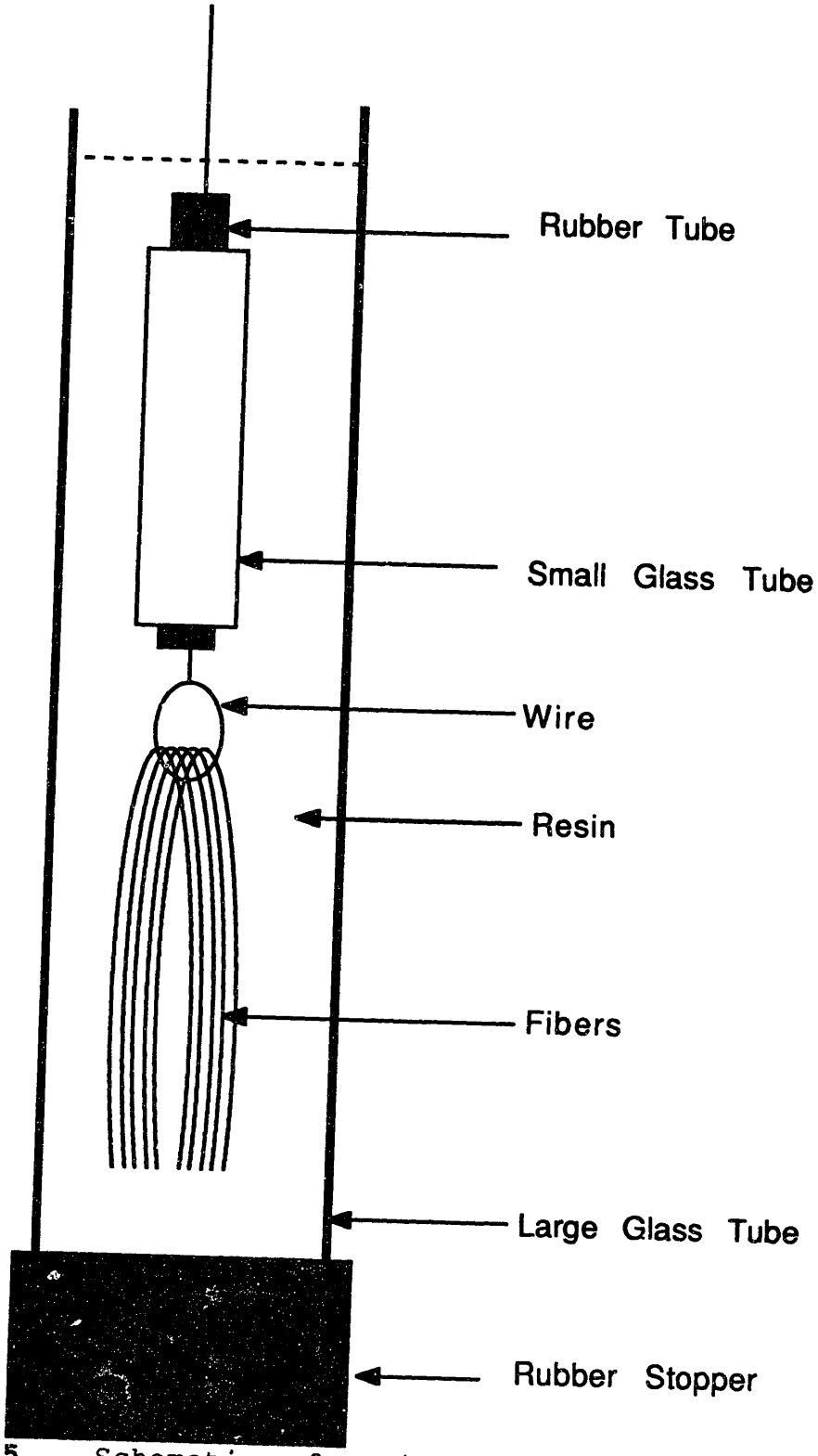


**Figure 3-5.** Schematic of Mini-composite manufacturing procedure.

**Figure 3-6.** Cross section of mini-composite showing good distribution of fibers and fiber volume fraction of 50 percent.

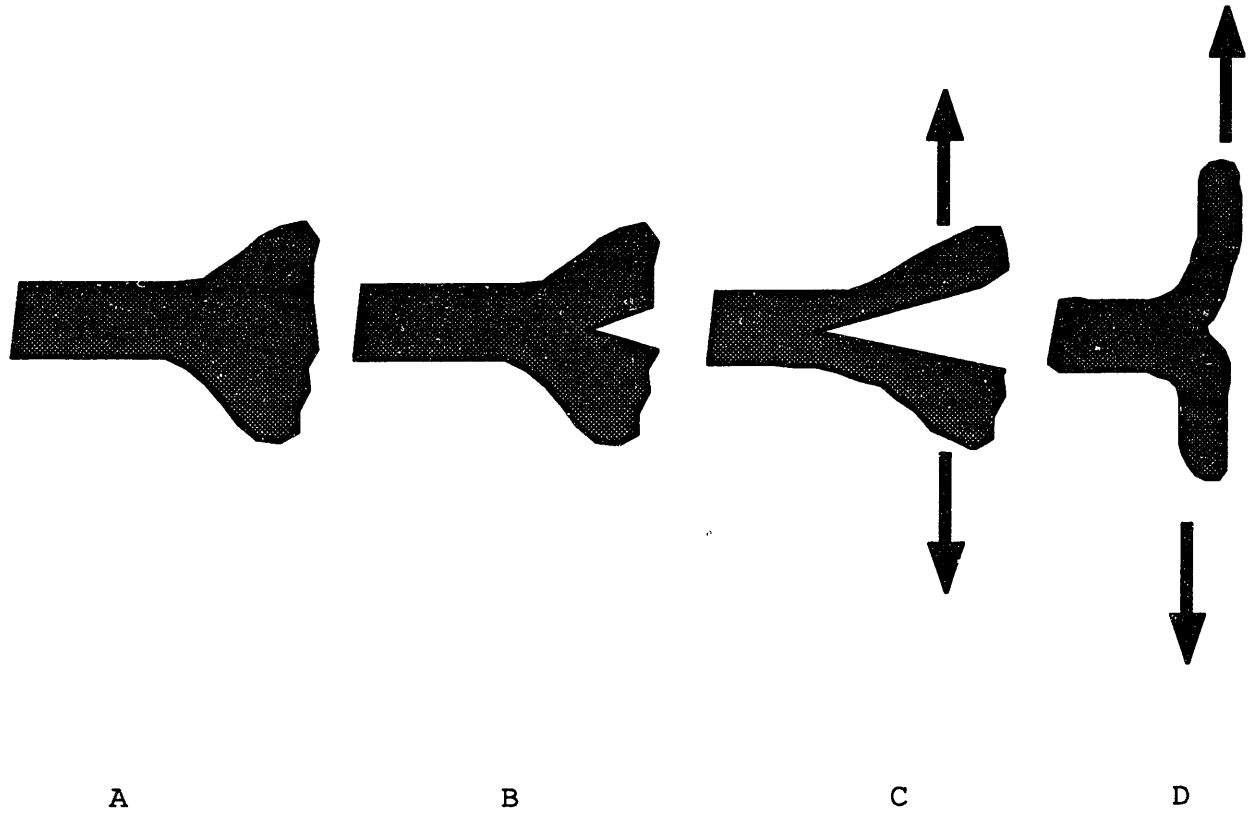


**Figure 3-7.** Schematic of lateral splitting test of single fiber. a) Flattening of fiber end b) Creating notch in flattened portion c) Pulling ligaments apart d) Propagating crack

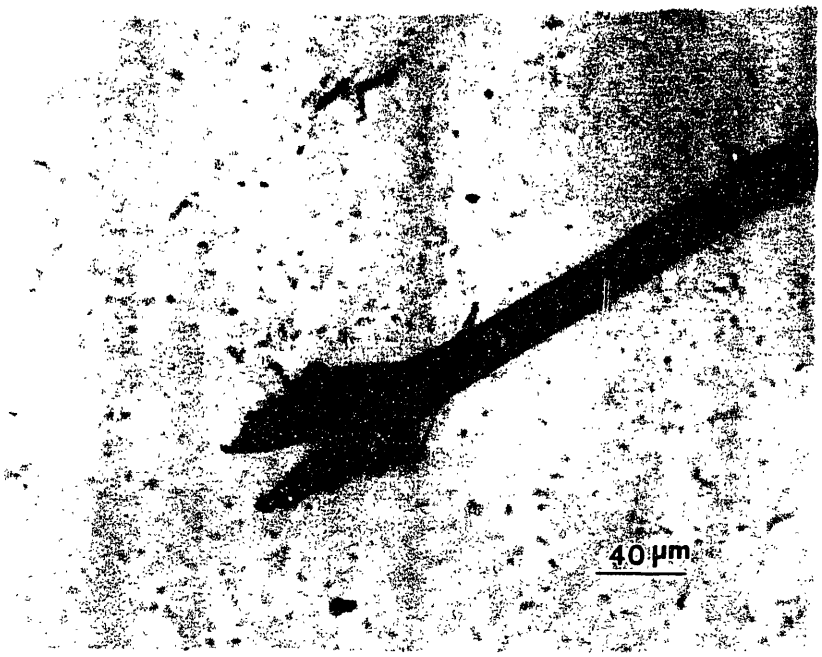


**Figure 3-8.** Optical micrograph of single fiber which has been flattened and then had a notch created in it using a micromanipulator.

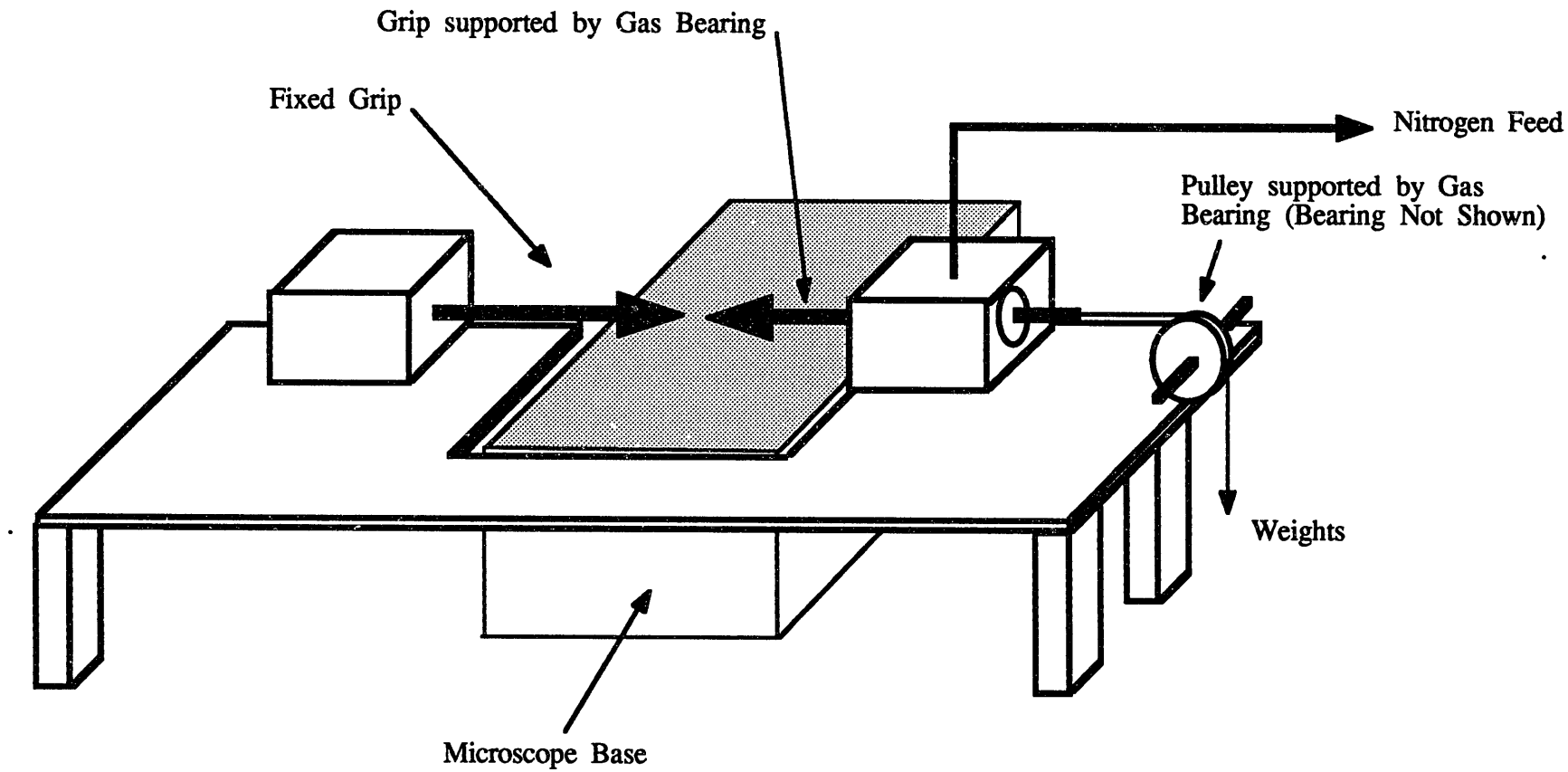


**Figure 3-9.** Schematic diagram of device used for transverse testing and three point bending.

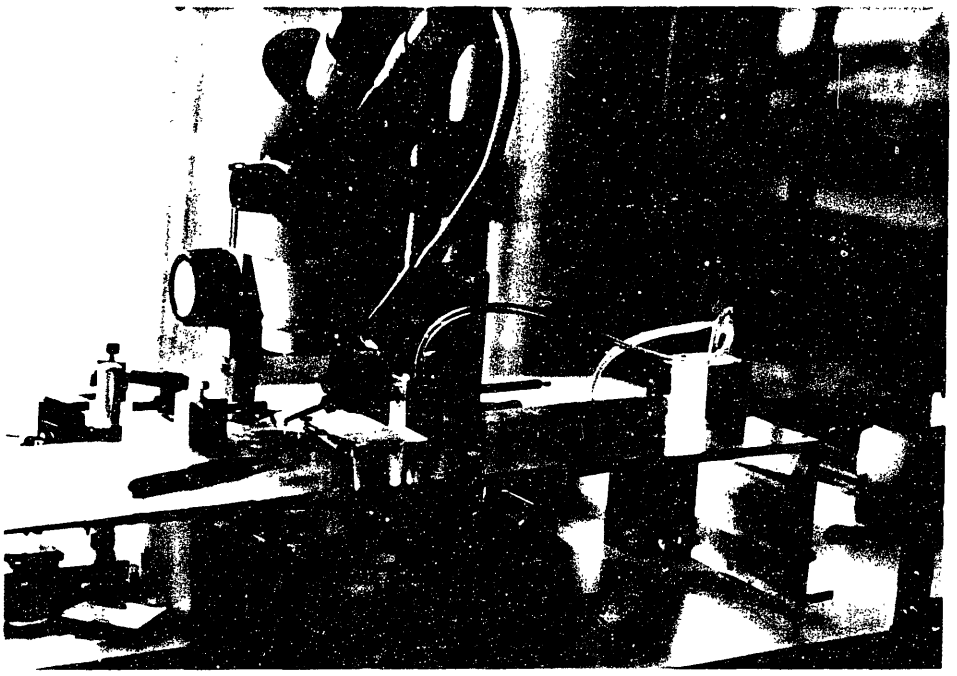

**Figure 3-10.** Photo of device used for transverse testing and three point bending.

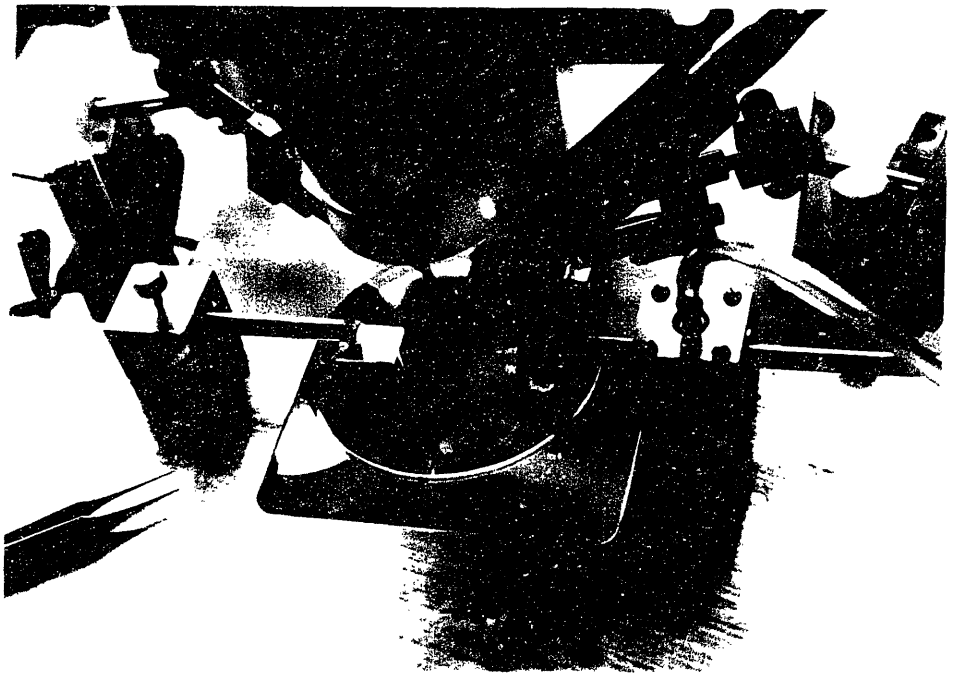

**Figure 3-11.** Photo of device used for transverse testing and three point bending.

procedure is observed with an optical microscope equipped with a closed circuit video system. The incremental weights are measured on a chemical balance which is inexpensive, accurate and easy to use. Their value, divided by the diameter of the fiber split, provides a number to represent the lateral integrity of the fiber: the opening mode axial crack initiating force, normalized by diameter.

In recognition of the fact that this test does not measure the true transverse tensile strength (it is actually a kind of micro fracture toughness test) this number has been named the Transverse Strength Index (TSI).

### 3.4.3. Compressive Modulus

The apparatus also can be used for single fiber three point bending tests. The fixed grip is replaced by a fiber support block. A hooked probe is attached to the movable grip. A fiber is placed on the platform with the hooked probe beneath it. When weights are added to the bucket the hooked probe loads the fiber at its midpoint. Deflections are measured with a video micrometer and kept small so that linear behavior occurs. A schematic of the bending device is given in Figure 3-12. A micrograph of the fiber support block is shown in Figure 3-13 and micrographs of a fiber being loaded are given in Figures 3-14 and 3-15.

If the angle of rotation of the fiber, $\theta$ (Figure 3-12), is small, then the basic differential equation for bending holds:

$$\frac{\partial^2 \delta}{\partial x^2} = -\frac{M}{EI} \qquad (3.2)$$

where $\delta$ is the deflection, x is the distance along the fiber, M is the bending moment, E is the modulus and I is the moment of inertia. The equation of the load deflection curve can be derived by double integration of equation 3.2

$$P = \frac{48 EI}{L^3} \delta \qquad (3.3)$$

where P is the load and L is the span.

Integration of equation 3.2 gives the angle of rotation of the fiber

$$\theta = \frac{P L^2}{16 E I} \qquad (3.4)$$

If $\theta$ is large ($\tan \theta \neq \theta$), then the analysis employed to derive equation 3.3 is not valid. Typical fiber diameters in the three point bend test are 10 - 30 um. The span is 800 - 1100 um and loads are usually less than 5 mN. With such typical values entered into equation 3.4, the angle of rotation is sufficiently small to employ basic elastic analysis.

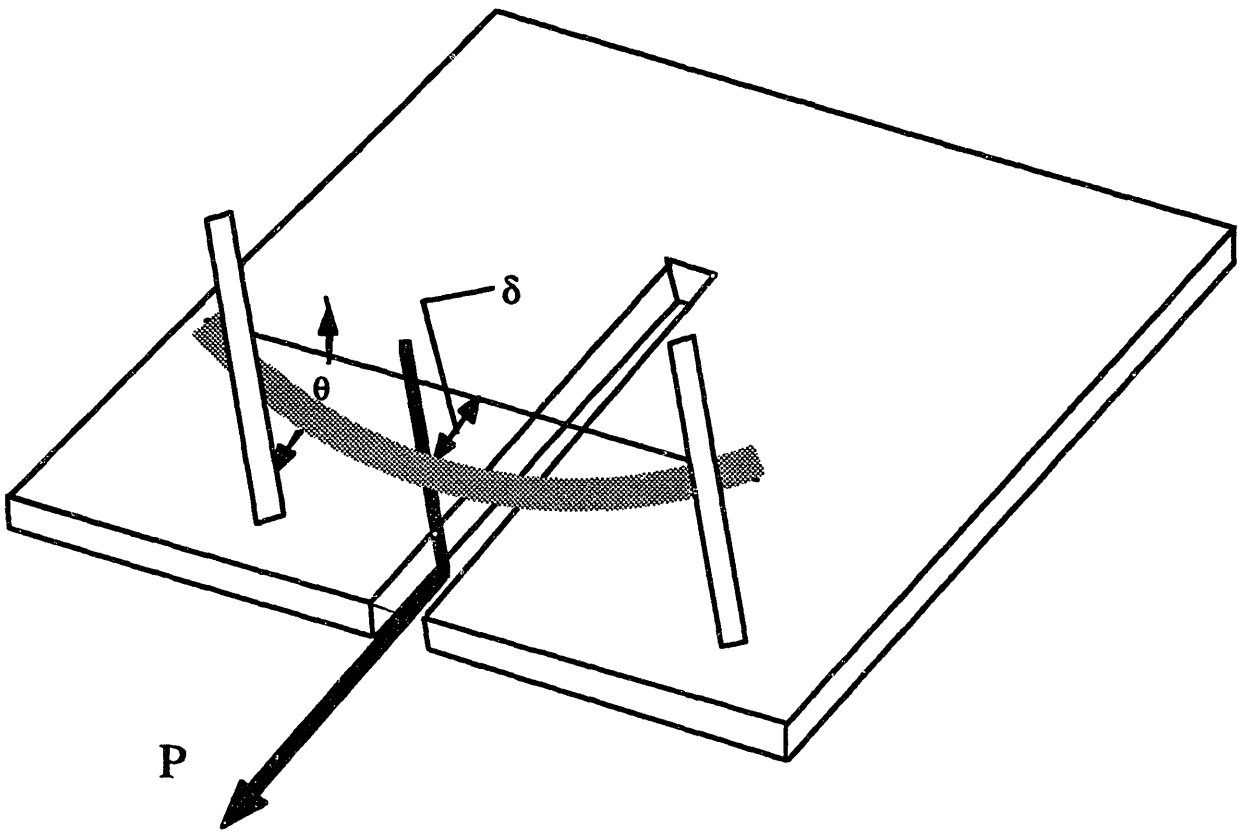


**Figure 3-12.** Schematic diagram of three point bend device

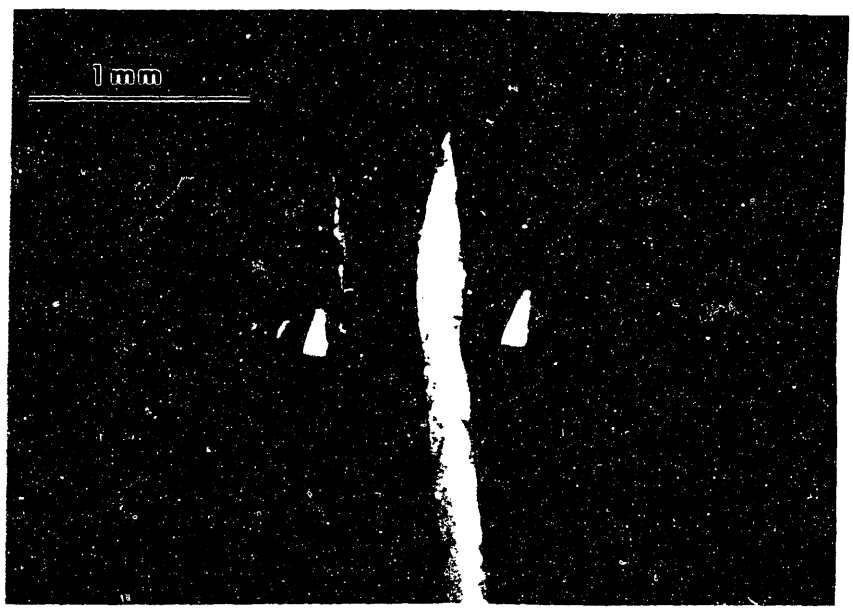


**Figure 3-13.** SEM micrograph of fiber support block. Span is about 950 um.

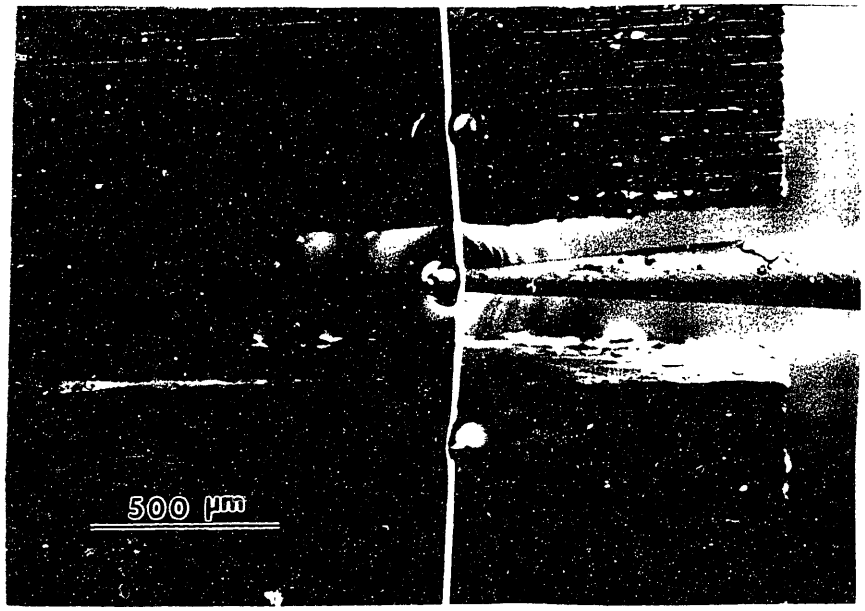


**Figure 3-14.** SEM Micrograph of single fiber being tested in three point bend configuration.

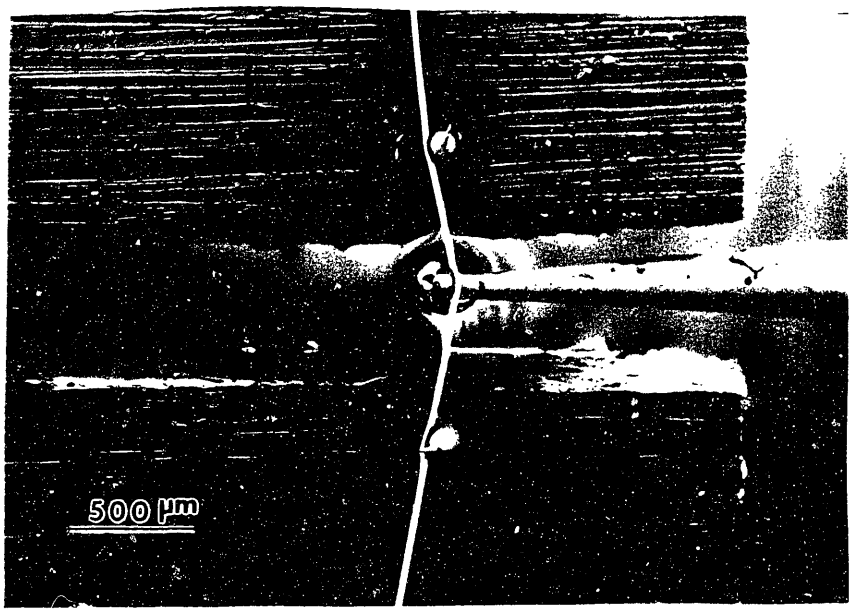


**Figure 3-15.** SEM Micrograph of single fiber being tested in three point bend configuration. Deflection is about 100um.

Equation 3.3 assumes that all deformation is due to flexure only; shear effects are not considered. Modified for shear deformation, equation (3.3) becomes

$$P = \frac{48 E I}{L^3} \delta \left( 1 + \frac{E d^2}{G L^2} \right)^{-1} \qquad (3.5)$$

where d is the fiber diameter and G is the shear modulus. Typical values of G are about two orders of magnitude less than E [8]. However, since the span in this case is about 950 um and the fiber diameter is typically 10 to 20 um, comparison of equation 3.3 and 3.5 show that shear effects are negligible for this particular testing geometry.

Equation 3.3 cannot be solved directly for the modulus as the moment of inertia with respect to the neutral axis is unknown. When the tensile and compressive moduli differ, the neutral axis of the fiber shifts away from the centroidal one, and the expression for the fiber bending stiffness becomes:

$$(EI)_f = E_C I_C + E_T I_T \qquad (3.6)$$

Where the subscripts f, c and T refer to fiber, compression and tension. The moment of inertia for each of the latter two is with reference to the displaced neutral axis and the magnitude of its displacement from the centroidal one is a function of the relative magnitudes of $E_C$ and $E_T$. Thus, if $E_T$ is known from another test, a tensile one, then Equation 3.6

contains only one unknown, $E_c$, but the algebra involved in obtaining an expression for $E_c$ becomes quite complicated, especially if the beam cross section is circular rather than rectilinear. Such is the case with many fibers, so the details of the solution are presented below.

In working out the solution for the anisotropic beam, a fiber with a circular cross section, it was also of interest to see how well this could be approximated by a rectilinear cross section, either a square circumscribed about the circle or one inscribed within it. This was motivated by the relative simplicity of the squares analyses.

Recalling equation 3.6, since $I_f=I_t+I_c$, 3.6 can be simplified to:

$$E_f I_f = (E_t - E_c) I_t + E_c I_f \qquad (3.7)$$

With the flexural rigidity measured from the three point bending test and the tensile modulus evaluated from a tension test, we can solve 3.7 for the compressive modulus if the appropriate moments of inertia are known.

### 3.4.3.1 Rectangular Model

If the cross section of the fiber is approximated by a rectangle which circumscribes the circle (Figure 3-16), the moments of inertia for the three rectangular sections

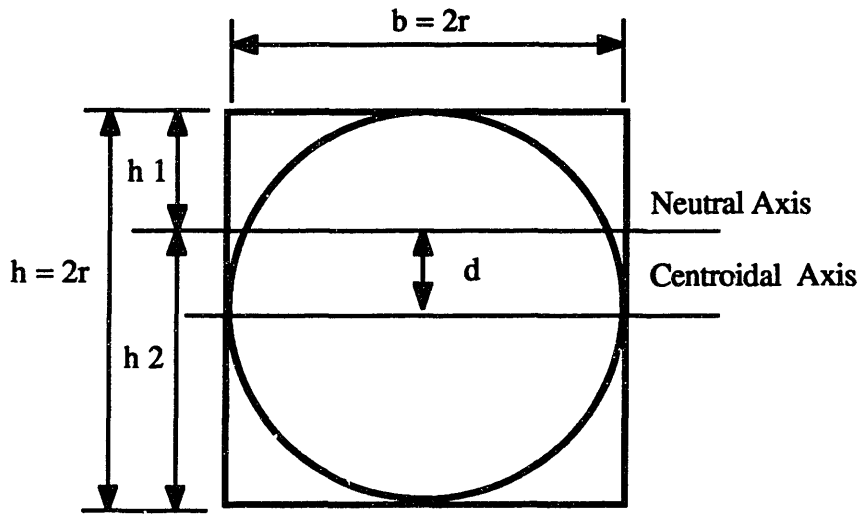


**Figure 3-16.** Rectangular cross-section around the neutral axis

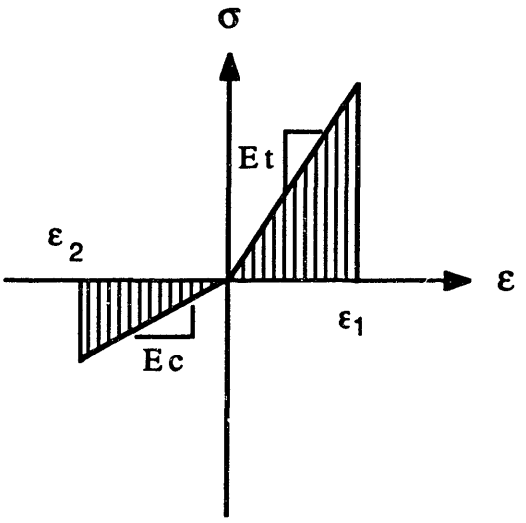


**Figure 3-17.** Tension-Compression Stress-Strain Diagram For Material With Unequal Tensile and Compressive Moduli Subjected to a Bending Moment

(total section, compressive section and tensile section) can be found by the parallel axis theorem (3.8) and the equation for the moment of inertia of a rectangle around its centroid (3.9):

$$I_x = I_{xc} + Ad^2 \tag{3.8}$$

where $I_x$ is the moment of inertia of a section about axis x, $I_{xc}$ is the centroidal moment of inertia of the section and A is the area. For rectangular shapes

$$I_{x_c} = \frac{bh^3}{12} \tag{3.9}$$

Thus, for the moment of inertia of the cross section around the neutral axis, $I_f$, the moment of inertia of the tensile section , $I_t$, and the moment of inertia of the compressive section around the neutral axis, $I_c$ we obtain:

$$I_f = \frac{4r^4}{3} + 4r^2d^2 \tag{3.10}$$

$$I_t = \frac{2\pi(r - d)^3}{3} \tag{3.11}$$

$$I_c = \frac{2\pi(r + d)^3}{3} \tag{3.12}$$

Since the shift in the neutral axis, d, cannot be directly measured, another method must be used to determine it. If the beam is subjected to a positive bending moment, for

equilibrium the two shaded areas under the stress-strain curve (Figure 3-17) must be equal. Hence

$$\frac{\sigma_t \varepsilon_1}{2} = \frac{\sigma_c \varepsilon_2}{2} \tag{3.13}$$

From Hooke's Law :

$$\sigma_t = E_t \varepsilon_1 \qquad \sigma_c = E_c \varepsilon_2 \tag{3.14}$$

also :

$$\varepsilon_1 = -\kappa h_1 \qquad \varepsilon_2 = -\kappa h_2 \tag{3.15}$$

where $\kappa$ is the curvature. Substituting equations (3.14) and (3.15) into equation (3.13), gives:

$$E_t h_t^2 = E_c h_c^2 \tag{3.16}$$

Which can also be expressed as:

$$\frac{E_t}{E_c} = \frac{h_c^2}{h_t^2} = \frac{(r+d)^2}{(r-d)^2} = \frac{d^2 + 2rd + r^2}{d^2 - 2rd + r^2} \tag{3.17}$$

Collecting terms, gives:

$$\left(\frac{E_t}{E_c} - 1\right) d^2 - \left(\frac{2E_t}{E_c} + 2\right) r\, d + \left(\frac{E_t}{E_c} - 1\right) r^2 = 0$$

(3.18)

Solving equation 3.18 for d, using the quadratic fcrmula, yields:

$$d = r\left(\frac{\sqrt{E_t} - \sqrt{E_c}}{\sqrt{E_t} + \sqrt{E_c}}\right)$$

(3.19)

(note that the root selected is the one for which $d \leq r$) Substitution of equations (3.10)-(3.12) and (3.19) into equation (3.6) gives the flexural rigidity :

$$E_f I_f = \frac{2r^4}{3}(E_t - E_c)(1 - z)^3 + \frac{4r^4}{3}E_c(1 + 3z^2)$$

(3.20)

where

$$z = \left(\frac{\sqrt{E_t} - \sqrt{E_c}}{\sqrt{E_t} + \sqrt{E_c}}\right)$$

Appropriate numerical methods can be used to evaluate (3.20) for $E_c$.

### 3.4.3.2 Circular Model

The same analysis as applied to a rectangular section can be applied to a section which is circular (Figure 3-18).

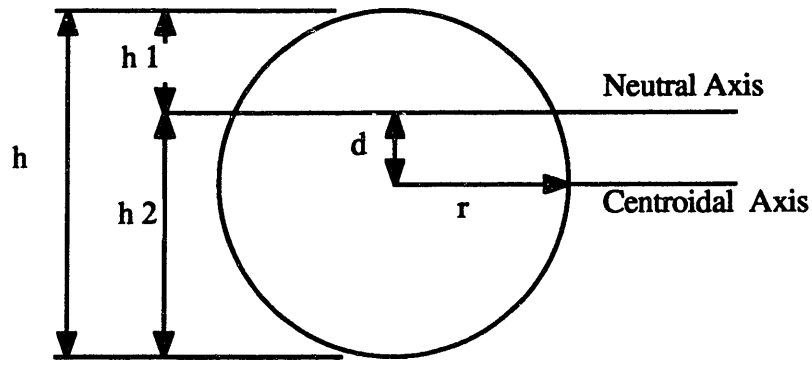


**Figure 3-18.** Circular Cross-Section

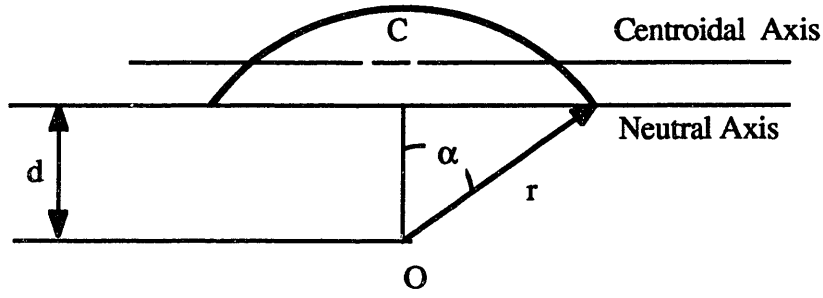


**Figure 3-19** - Circular Segment

For a circle:

$$I_f = \frac{\pi r^4}{4} + \pi r^4 z^2 \tag{3.21}$$

For $I_t$ we use a circular segment (Figure 3-19). Applying the parallel axis theorem we find that

$$I_t = r^4\left[\frac{1}{8}(2\alpha - \sin 2\alpha)\left(1 + \frac{2\sin^3\alpha\cos\alpha}{\alpha - \sin\alpha\cos\alpha}\right) - \frac{8}{9}\frac{\sin^6\alpha}{2\alpha - \sin 2\alpha}\right] + \frac{r^2}{2}(2\alpha - \sin 2\alpha)\left[r\left(\frac{4\sin^3\alpha}{6\alpha - 3\sin 2\alpha}\right)\right]^2 \tag{3.22}$$

Where:

$$\alpha = \cos^{-1}\frac{d}{r} = \cos^{-1} z \qquad \left(\alpha \le \frac{\pi}{2}\right) \tag{3.23}$$

Substituting (3.21) - (3.23) into (3.7) we arrive at the expression for the flexural stiffness of an anisotropic beam with a circular cross section

$$E_f I_f = (E_t - E_c)\left\{\begin{array}{c} r^4\left[\frac{1}{8}(2\alpha - \sin 2\alpha)\left(1 + \frac{2\sin^3\alpha\cos\alpha}{\alpha - \sin\alpha\cos\alpha}\right) - \frac{8}{9}\frac{\sin^6\alpha}{2\alpha - \sin 2\alpha}\right] + \\ \frac{r^2}{2}(2\alpha - \sin 2\alpha)\left[r\left(\frac{4\sin^3\alpha}{6\alpha - 3\sin 2\alpha} - \cos\alpha\right)\right]^2 \end{array}\right\} + E_c\left(\frac{\pi r^4}{4} + \pi r^4 z^2\right) \tag{3.24}$$

Again, appropriate numerical methods can be used to evaluate Equation 3.24 for $E_c$.

A validity check of the analysis is shown in Figure 3-20. Here each curve represents a single value of the normalized bending stiffness, $(EI)_f/r^4$, and shows how the tensile and compressive moduli vary as the stiffness remains constant. The curves are symmetrical about the 45° diagonal as they should be, hence the validity check.

Figure 3-21 shows a plot of flexural rigidity versus compressive modulus for different cross sections. The circumscribed square is seriously in error and while it is not shown, the inscribed one is also; the magnitudes of the errors change, depending on the particular fiber being analyzed, but they are always significant. In contrast, a square cross section having the same area as the circular cross section gives a nearly identical solution, at least for the case presented. How broadly this equivalence can be generalized or extended is not known, but for the fibers of interest it seems to be a good approximation.

Figure 3-22 shows the fiber compressive modulus as a function of the normalized bending stiffness, $(EI)_f/r^4$, where r is the fiber radius. Curves for two fiber tensile moduli are plotted: 124 GPa (18 Msi) is typical for Kevlar® 49 and 276

GPa (40 Msi) represents PBO. Both refer to circular cross-section fibers and both can be fit by the polynomial expressions shown. This presentation of the analysis is convenient for interpreting experimental measurements made on fibers: to obtain a compressive modulus one simply takes the measured value of (EI), divides it by $r^4$ and substitutes it into the expression derived from the tensile modulus of the fiber of interest. Figure 3-22 does imply one very sensitive feature of this whole approach to determining a fiber's compressive modulus: errors in the fiber diameter are raised to the fourth power, so accuracy in this measurement is very important. Use of an SEM is recommended. The potential magnitude of the error associated with improper radius measurement is shown in Figure 3-23[15]: a 0.5 um difference in the radius can lead to almost 100 percent error in compressive modulus in some cases. This also emphasizes the need for a uniform cross section in the analysis invoked. For a more detailed description of error sources in the three point bending test the reader is referred to Appendix I. Finally, a validity check on the three point bend test procedure was made: glass fibers which are isotropic and well characterized were tested. A measured flexural modulus for the glass fibers identical to the tensile modulus would indicate a satisfactory testing process.

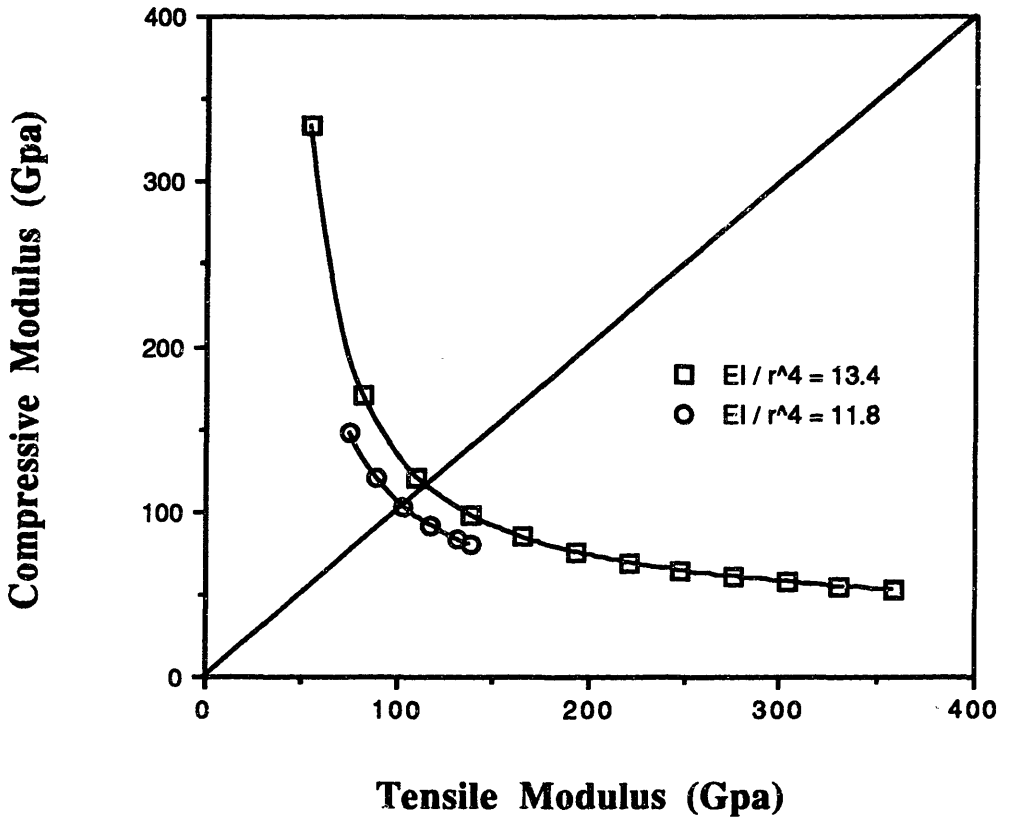


**Figure 3-20.** Compressive Modulus versus Tensile Modulus for Fibers With Normalized Flexural Rigidities Typical of Kevlar® (11.8) and PBO(13.4).

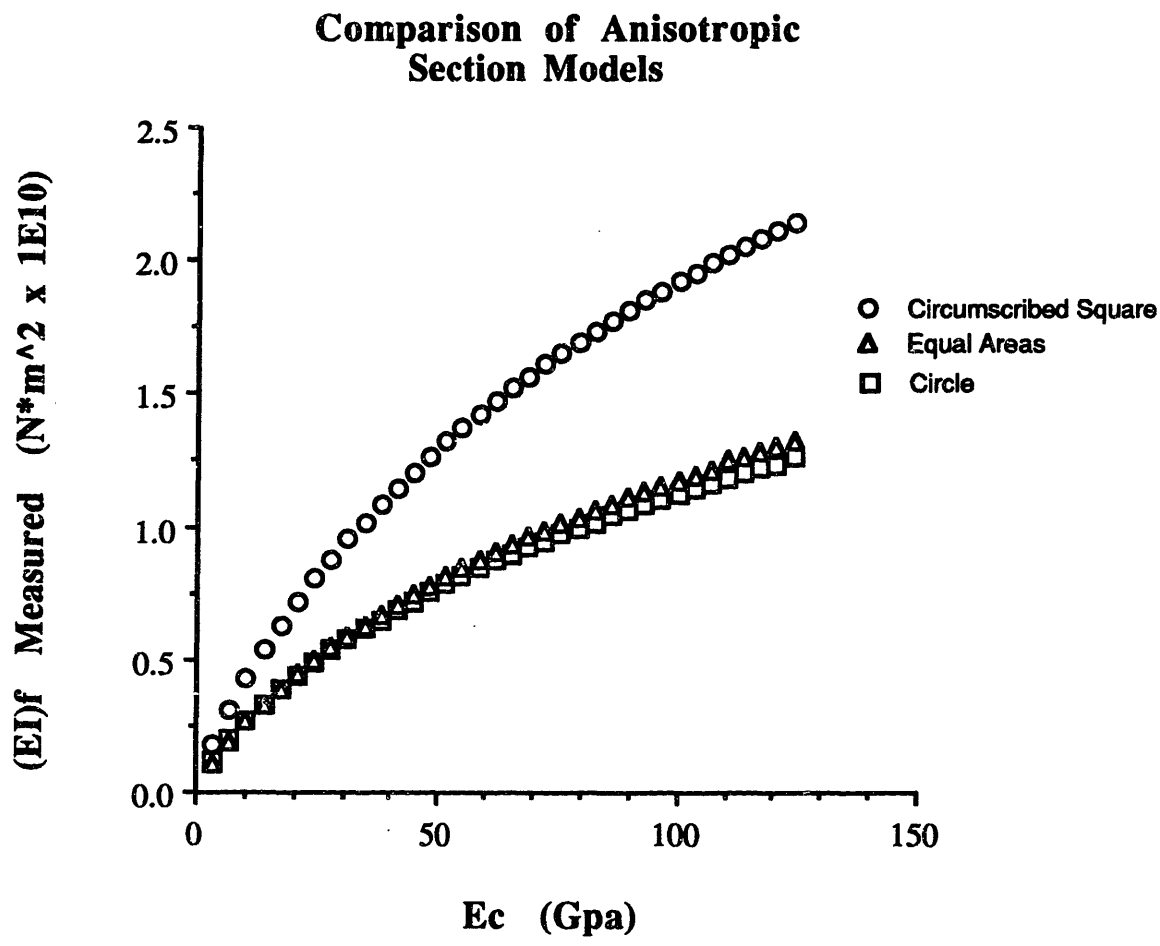


**Figure 3-21.** Flexural rigidity versus compressive modulus for different cross section

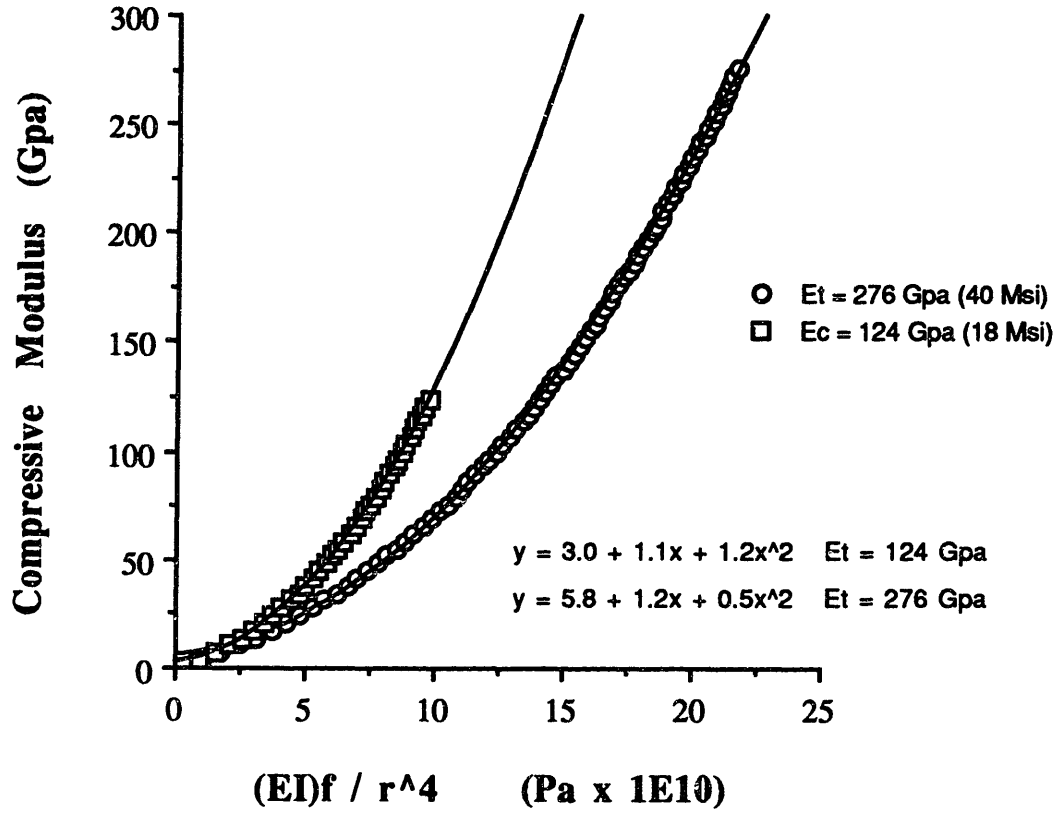


**Figure 3-22.** Normalized bending stiffness for fibers of different tensile modulus.

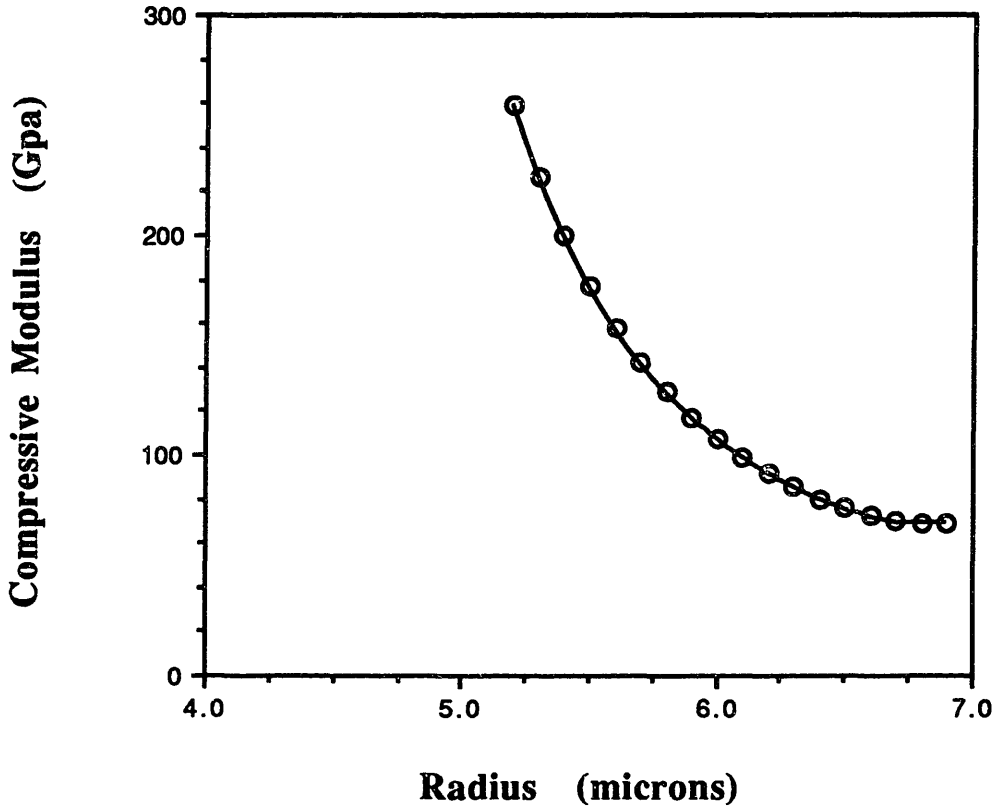


**Figure 3-23.** Compressive Modulus as a Function of Fiber Radius for a Measured Flexural Rigidity, EI, Typical of PBO Fibers.

## 3.5. Results and Discussion

### 3.5.1. Axial Compressive Strength

#### 3.5.1.1. Recoil Testing

It has been found that using FI-RE-CUT the success rate for correctly cutting fibers is nearly 100 percent for Kevlar® 49 and about 80 percent for PBO and other stiff experimental fibers, compared with about 80 percent and 30 percent, respectively, using other methods. Typical values of the compressive strength from the tensile recoil test are given in Table 3-1.

#### 3.5.1.2. Composite Testing

A typical Stress - displacement curve for a mini-composite is given in Figure 3-24. Specimen failure is defined as the onset of nonlinear behavior. This is also marked by visible failure in the composite by formation of a global kink band. Compressive strengths were obtained using a simple rule of mixtures approach which assumed that the epoxy matrix exhibited linear behavior well beyond the strains required for fiber failure (this was verified by compression testing neat epoxy samples).

The results for PBO and Kevlar® fibers, given in Table 3-2 are in reasonable agreement with single fiber compressive

strengths obtained from tensile recoil testing. The Kevlar® values are also similar to those reported by the manufacturer[16]. The increase in fiber compressive strengths from composite data over those from recoil testing may be caused by the increased lateral support provided by the matrix to the composite fibers.

### 3.5.2. Transverse Strength

Table 3-3 presents the results from lateral testing. The various PBO fibers listed have the same composition but were processed under different conditions. The difference in the transverse strength index (TSI) between these fibers indicate that the TSI can be used to evaluate changes in processing parameters. It does not appear that there exists any relationship between TSI and fiber compressive strength. It is interesting to note that PBO-1 and Kevlar® 49 have similar TSI values. If the TSI were based on intermolecular strength, one would expect the Kevlar® 49, a polyamide capable of hydrogen bonding, to have a higher value than PBO. Since this is not the case, one can conclude that lateral properties are more likely based on interfibrillar than intermolecular strength. Hence, attempts at improving lateral (and compressive) strength by introducing primary valence bonding in the transverse direction (interchain) will

**Table 3-1.**

Compressive Strength From Tensile Recoil Test

| Fiber | Compressive Strength [MPa(Ksi)] |
|---|---|
| PBO-1 | 172 ± 5 (25) |
| PBO-2 | 414 ± 4 (60) |
| PBO-3 | 152 ± 6 (22) |
| PBO-4 | 324 ± 5 (47) |
| PBO-5 | 227 ± 6 (31) |
| PBO-6 | 165 ± 6 (24) |
| Kevlar® 29 | 365 ± 10 (53) |
| Kevlar® 49 | 379 ± 10 (55) |

**Table 3-2.**

Compressive Strength of Fibers From Mini-Composites

| Fiber | Compressive Strength [MPa(Ksi)] |
|---|---|
| PBO-1 | 220 ± 11 (32) |
| Kevlar® 49 | 448 ± 13 (65) |

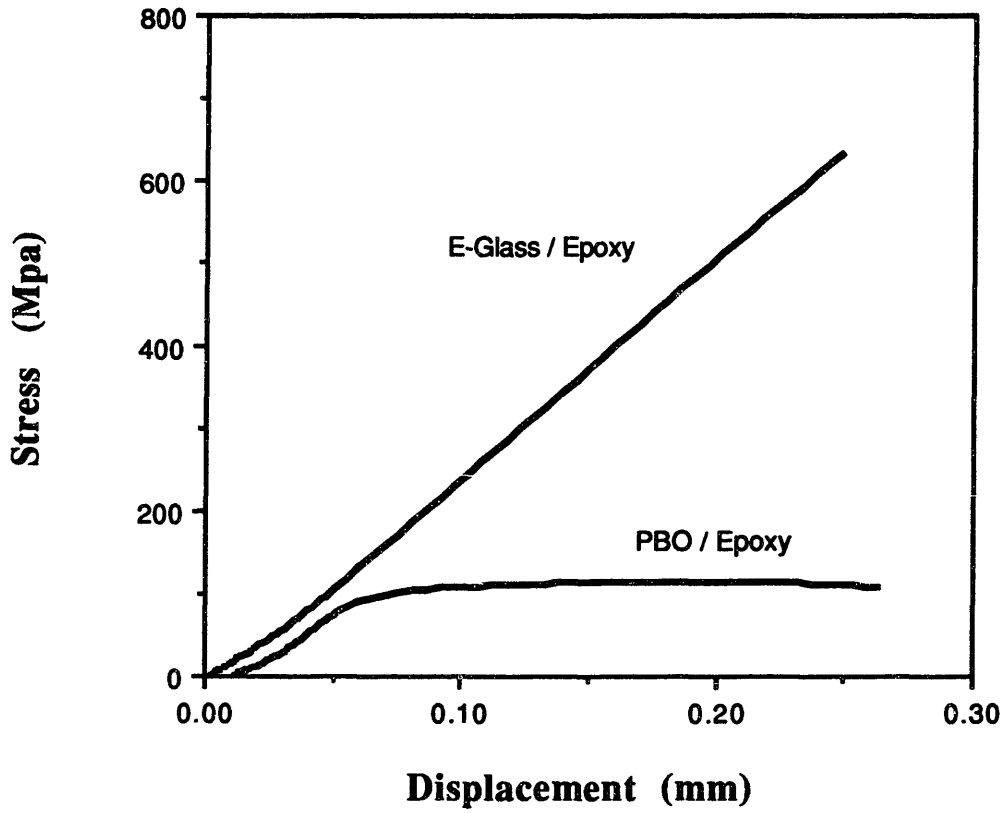


**Figure 3-24.** Stress-Deflection plot from compression testing of mini-composites

**Table 3-3.**
Transverse Strength Index for Several
High Performance Fibers

| Fiber Designation | Fiber Diameter (um) | Transverse Strength Index [N/m (lb/in)] |
|---|---|---|
| Spectra | 35 | 349 ± 44 (1.99) |
| Kevlar® 49 | 12 | 519 ± 42 (2.96) |
| PBO-1 | 24 | 491 ± 47 (2.80) |
| PBO-3 | 16 | 272 ± 21 (1.55) |
| PBO-4 | 17 | 278 ± 24 (1.59) |
| PBO-5 | 24 | 285 ± 15 (1.63) |
| PBO-6 | 27 | 339 ± 38 (1.93) |

Note: PBO-2 was not included in this study as an insufficient quantity of it was available for TSI evaluation.

be ineffective as interfibrillar interactions will be unaffected. This has been the case in several studies[2,24].

### 3.5.3. Compressive Modulus

Figure 3-25 shows the results for three point bending of single glass fibers. Since the glass fibers are isotropic, equation 3.3 can be solved directly for Ef. This is done by using a least squares analysis line fit to the load data .

The slope of the line of the load - deflection curve is then given by

$$\text{Slope} = \frac{48\,E\,I}{L^3} \qquad (3.22)$$

which is solved for E since I and L are known. The result is an average flexural modulus of 75.8 GPa (11 Msi) which is in good agreement with literature values for the tensile modulus of E-glass.

Figure 3-26 shows flexural data for Kevlar® fibers. The least squares fit for the Kevlar® 149 fibers uses the first three data points only as the fibers exhibited non-linear behavior at higher loads as shown in Figure 3-27, most likely as a result of kink band formation. Figure 3-28 shows the three point bending for PBO fibers. The difference in the slopes of the curves comes from the variation in fiber diameter.

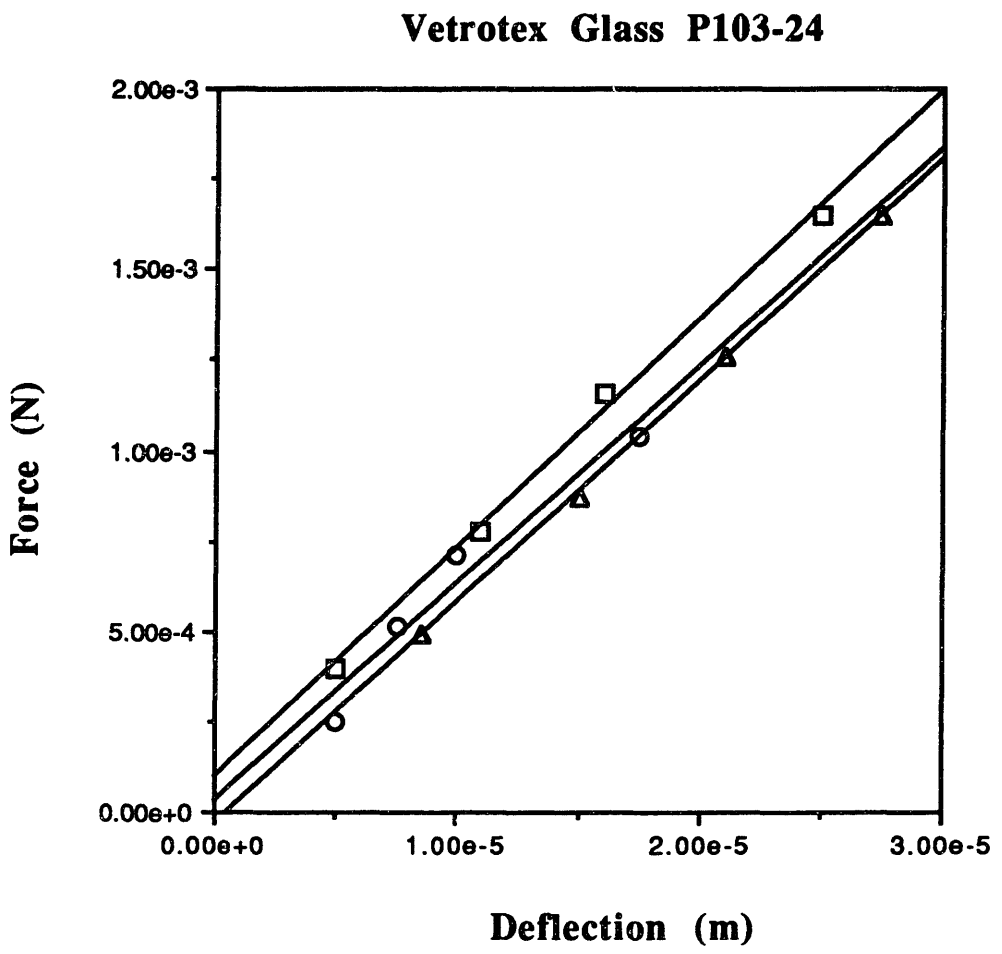


**Figure 3-25.** Load-Deflection plot from three point bending on single glass fibers

Using the analysis described, the values of compressive modulus for several fibers are given in Table 3-4. All values of tensile moduli employed in the calculations are those provided by the manufacturers. Tensile moduli were not explicitly measured in this study. As can be seen, in all cases the values of the compressive modulus are less than the tensile ones and in one instance, greatly so. While there has arisen the assumption that the two should be equal[3] in fact just the opposite is to be expected. The microstructure of these fibers is highly fibrillar and while the polymer chains are oriented along the fiber axis, the alignment probably is not perfect nor uniform. Thus, at the chain level, a pull will tend to improve the alignment and a push, to reduce it. It is also clear if the molecules involved have a non symmetric potential well that different tensile and compressive moduli will be expected, except in the absolute limit of zero strain. Further, the Kevlar® microstructure exhibits a pleated sheet[17] form which, under tension, will open and flatten, becoming stiffer, whereas, when compressed, it will fold more closed and decrease in stiffness.

Another interesting feature of the data is the apparent sensitivity of the compressive modulus. The two PBO cases, while identical in composition, underwent somewhat different processing in the fiber drawing stage and this was reflected

**Table 3-4.**
Compressive Modulus for Several High Performance Fibers

| Fiber | Assumed Tensile Modulus, $E_t$ [GPa(Msi)] | Compressive Modulus, $E_c$ [GPa(Msi)] | Ratio $E_c/E_t$ |
|---|---|---|---|
| PBO-1 | 276 (40) | 40 (6) | 0.15 |
| PBO-2 | 276 (40) | 240 (35) | 0.87 |
| Kevlar® 29 | 96 (14) | 90 (13) | 0.94 |
| Kevlar® 49 | 124 (18) | 90 (13) | 0.73 |
| Kevlar® 149 | 179 (26) | 55 (8) | 0.31 |

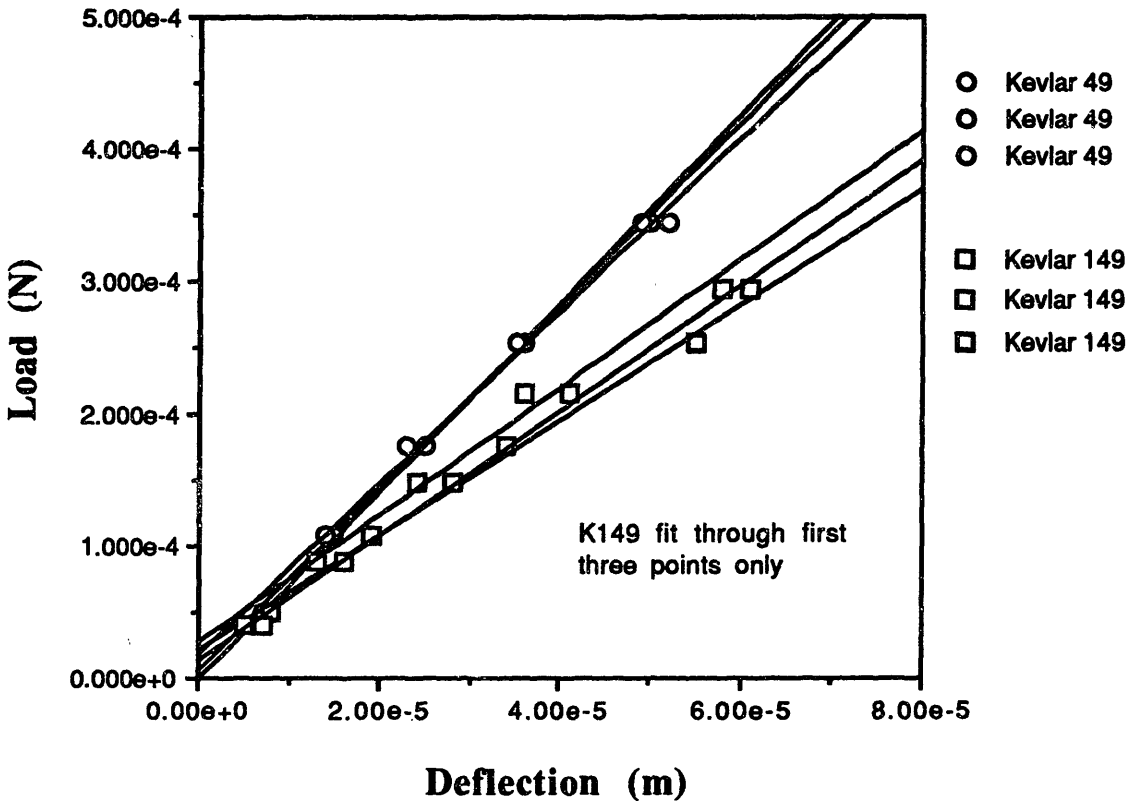


**Figure 3-26.** Load-Deflection plot from three point bending on single Kevlar® fibers

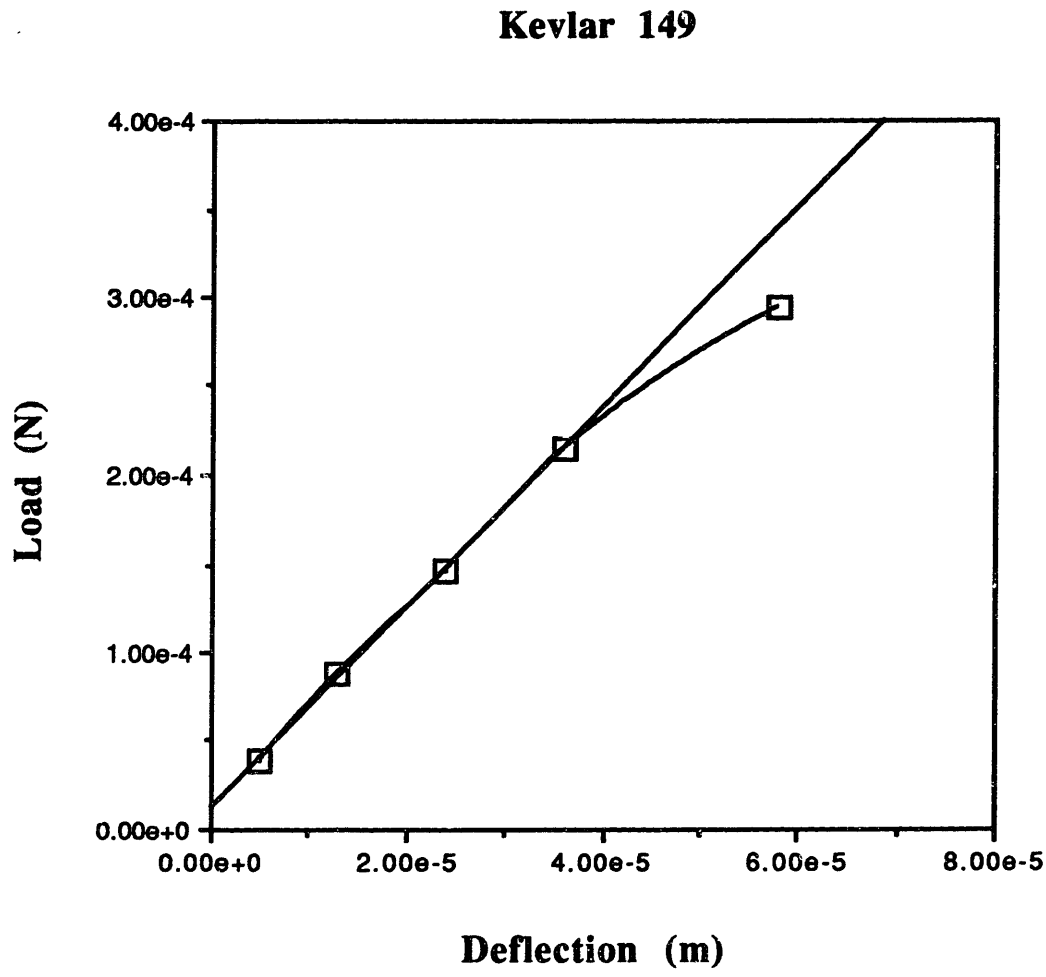


**Figure 3-27.** Load-Deflection plot from three point bending on single Kevlar® 149 fiber.

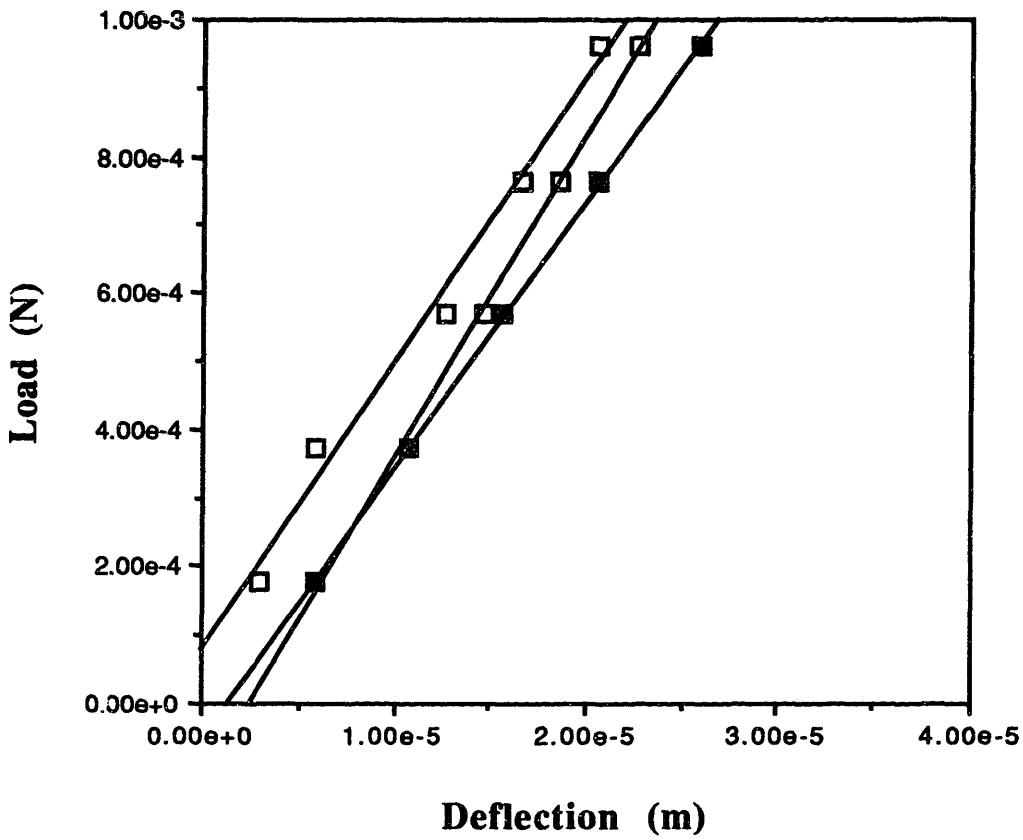


**Figure 3-28.** Load-Deflection plot from three point bending on single PBO fibers

in the compressive modulus values. By other methods, the microstructural and morphological changes accompanying the difference can be explored, but the simple bending test revealed that the two fibers had marked differences in mechanical properties; this was confirmed by differences in compressive strength behavior also (Table 3-1).

Some other interesting three point bending experiments can be envisioned: experimentation with shorter spans which will produce significant shear deformations is being conducted; it may be possible to determine the shear modulus directly in this manner.

Finally, another feature of the single fiber bending test is proving to be interesting: its use to study compressive failure. Bending fibers until visible kink band formation can be a useful method for determination of compressive strength. The current loading geometry makes this difficult, however, because the loading probe is located at the point of maximum stress and tends to make kinks difficult to see. A four point bending configuration would be more suitable for a compressive strength test and it is under development[15].

# Chapter 4. Modeling of Fiber Compressive Failure

## 4.1. Evidence of Fibril Buckling

It is well known that high performance polymer fibers fail in compression by kink band formation[18,3]. Kinking has been described as a buckling failure on several different microstructural scales: Deteresa et al[3] developed a model for kink formation based on the buckling of single polymer chains while Cohen and Thomas[19] described microfibrils as the buckling entity. The former model concludes that the compressive strength should be equal to the shear modulus and although this has not proven to be the case, data exists that show a linear correlation between the two. Although they recognized the fibril as the buckling entity, the latter researchers made no attempt to model the compressive strength of fibers as a function of fibrillar microstructure. Kumar[20] discussed fibril buckling but concluded that it was not a viable mechanism to explain similarities in compressive strength among PBO fibers with different tensile moduli.

Figure 4-1 is a SEM micrograph of a PBO fiber which has been split with a micromanipulator ; the fibrillar structure of the fiber is evident on the split surface. The rear surface

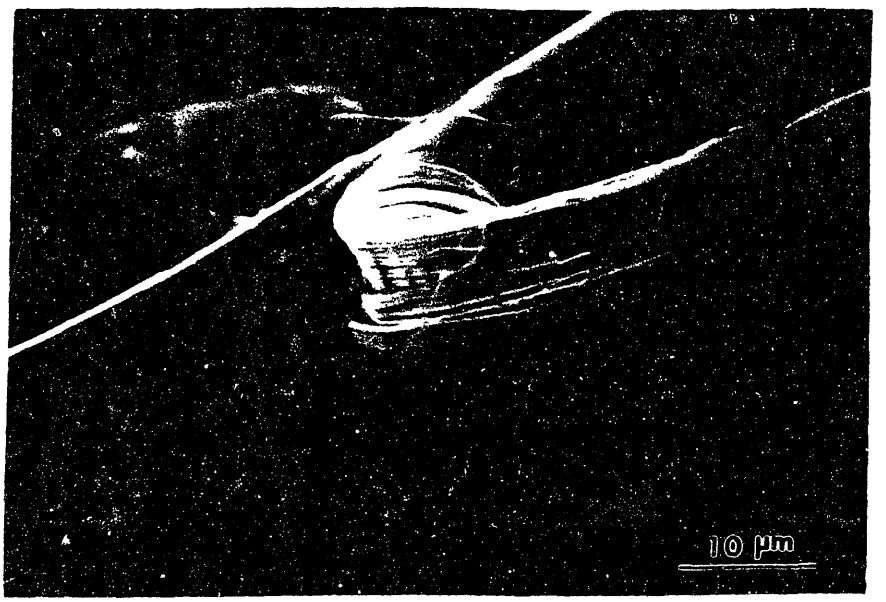


**Figure 4-1.** SEM Micrograph of Single PBO Fiber split with micromanipulator.

of the fiber is in compression and kink bands have formed. These kinks have propagated through the fiber and buckled fibrils are also visible on the split surface. Such visible evidence (along with that from others[17,18]), which is clearly indicative of fibril failure within the kink, has motivated modeling of compressive failure by fibril buckling in this research.

## 4.2. Modeling with Euler Buckling

The most simple model for buckling is that given by Euler[21]. The critical buckling load for a column is defined as the load applied to the column which, when removed, causes the column not to return to its original position. At loads higher than the critical value, the column becomes unstable and will collapse by bending. Examining Figure 4-2, we can see that this will occur when the applied moment (P*y) is greater than the restoring moment (M). Assuming small deformations, the internal moment, M, is given by

$$EI \frac{\partial^2 y}{\partial x^2} = -M \qquad (4.1)$$

Setting this equal to the external moment gives

$$EI \frac{\partial^2 y}{\partial x^2} + Py = 0 \qquad (4.2)$$

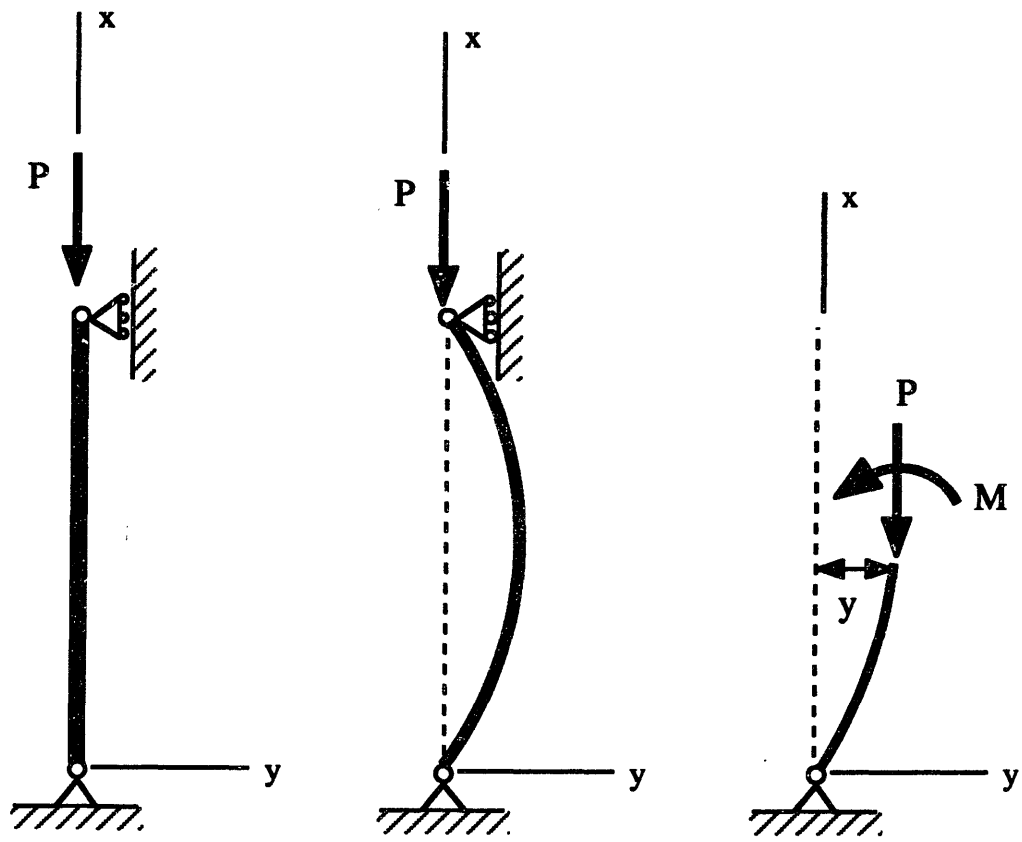


**Figure 4-2.** Schematic of Simply Supported Column

which is a second order homogeneous linear differential equation and can be solved to yield

$$P = \frac{n^2\pi^2EI}{L^2} \qquad (4.6)$$

where n is the number of half sine waves or buckling modes. The smallest value of the buckling force is given when n=1.

Obviously, no lateral loading of the fibril is considered in the Euler analysis. This implies that the fiber is transversely isotropic (Chapter 2) and that no coupling exists between axial and radial stresses. A cylindrically orthotropic system could have substantial lateral tensile stress develop on the fibrils as a consequence of axial compressive loading, and the critical buckling load would be greatly reduced.

With respect to fibril buckling, the parameters necessary for prediction of critical buckling loads are the fibril compressive modulus, $E_c$, the fibril moment of inertia, I, and the fibril single mode buckling length L.

The compressive modulus is obtained from single fiber three point bending tests described in Chapter 3. Here it is assumed that the individual fibrils have the same compressive

modulus as the bulk fiber. The fibril moment of inertia is given by

$$I = \frac{\pi r^4}{4}$$

where no shift in the neutral axis is considered for axial loading. The fibril diameter is found by splitting individual fibers and measuring the diameters with an SEM. A typical micrograph is shown in Figure 4-3.

The single mode buckling length for a single fibril can be found in a number of different ways. The first has been performed on Kevlar® 49 fibers and entails peeling a sheath of fibrils from the fiber as shown in Figure 4-4. The high curvature at the peel point causes the fibrils to buckle. A composite micrograph of a sheath of fibrils is given in Figure 4-5. The single mode buckling length L, or arc length of the buckled fibril, is easily calculated by measuring the chord length, 2b, and the departure, $\delta$, of the arc from the chord as shown in Figure 4-6. Using this method on 10 different buckled Kevlar® 49 fibrils from Figure 4-5 gives an average buckled length of 1510 nm with a standard deviation of 224 nm.

Another method for determination of the buckled length has been employed on PBO fibers. In this process a section of the skin is peeled from the fiber. In PBO, the skin buckles in regular arrays as shown in Figures 4-7 and 4-8.

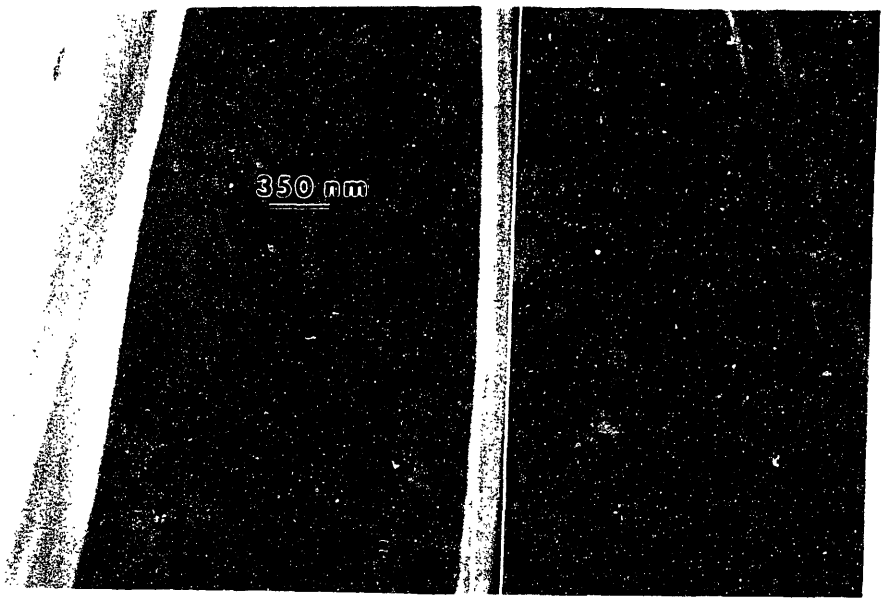


**Figure 4-3.** SEM Micrograph of single Kevlar® 49 fibril from a fiber split with a micromanipulator.


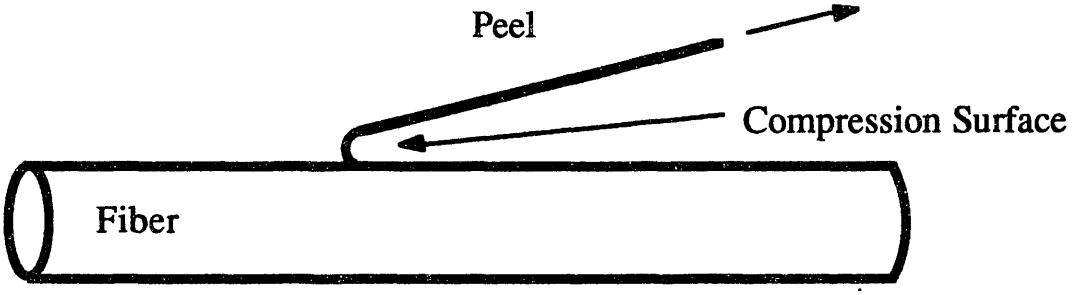


**Figure 4-4.** SEM Micrograph of sheath of fibrils peeled from Kevlar® 49 fiber as shown in schematic. Buckling of fibrils in high curvature region is evident.

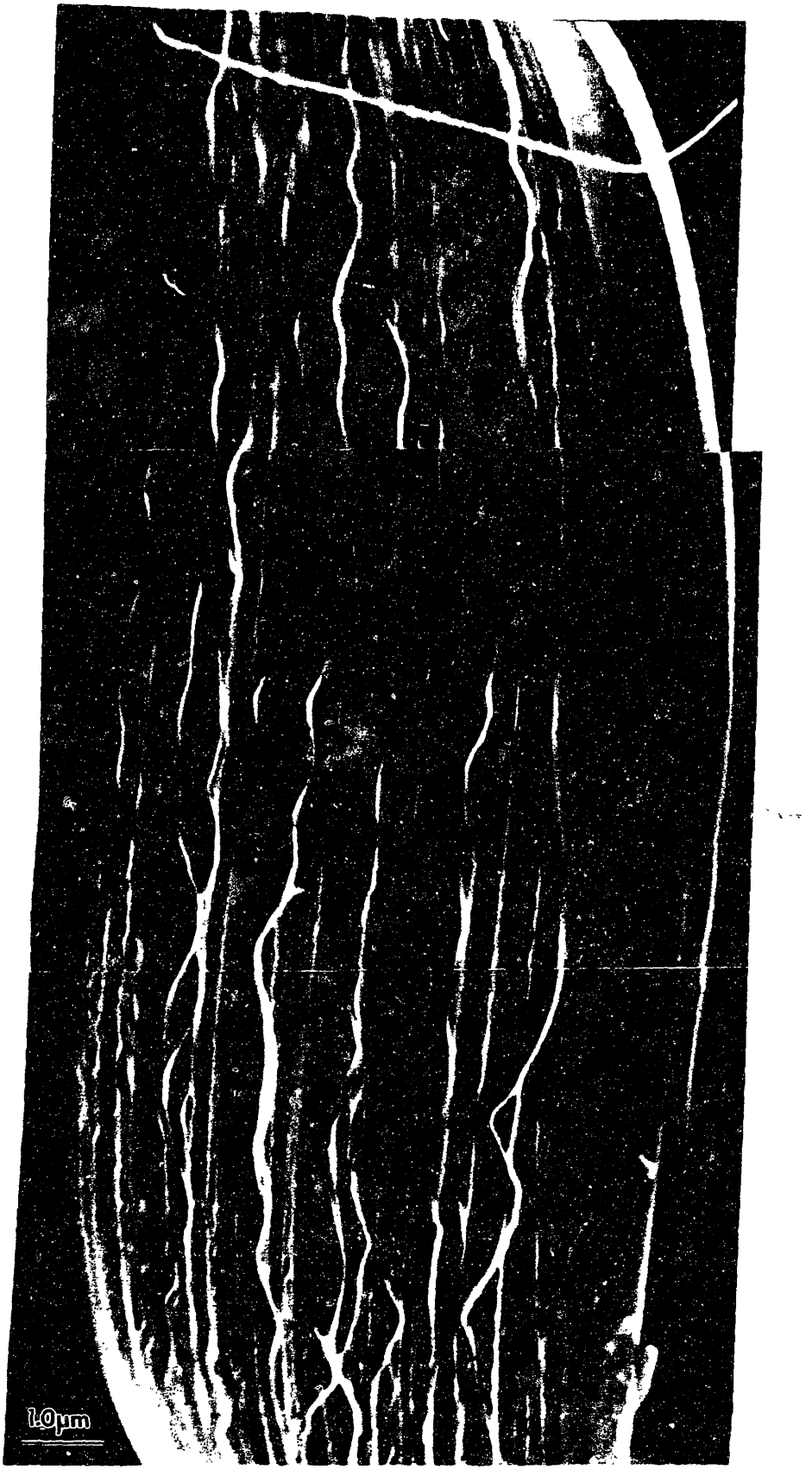


**Figure 4-5.** SEM Micrograph of sheath of fibrils peeled from Kevlar® 49 fiber.

This R4† effect seems to be more prominent in PBO than Kevlar® fibers. If it is assumed that the fibrils behind the skin buckle over the same length as the skin then the periodic spacing of the R4 effect can be used as the single mode buckling length.

The buckling length can also be determined by plasma etching of previously compressed fibers. It has been shown by DeTeresa *et.al* that fibers which are compressed to kink formation and subsequently placed in tension show unfolding or reversal of kinks[8]. If these fibers are etched with an $O_2CF_4$ plasma, small pits appear at the kink boundary[22] as shown in Figure 4-11. Since fibrillation during compressive failure causes an increase in fibril surface area, the buckled region is etched at a higher rate causing pit formation. The diameter of the pits are indicative of the length of the buckled fibril. Since the ultimate pit size is a function of etchant and exposure time, this method can only be used qualitatively for comparison of fibers exposed to similar conditions.

† This is called the R4 effect since it was first observed by an undergraduate research student: **R**odrigo **R**. **R**ubiano's **R**ipples.

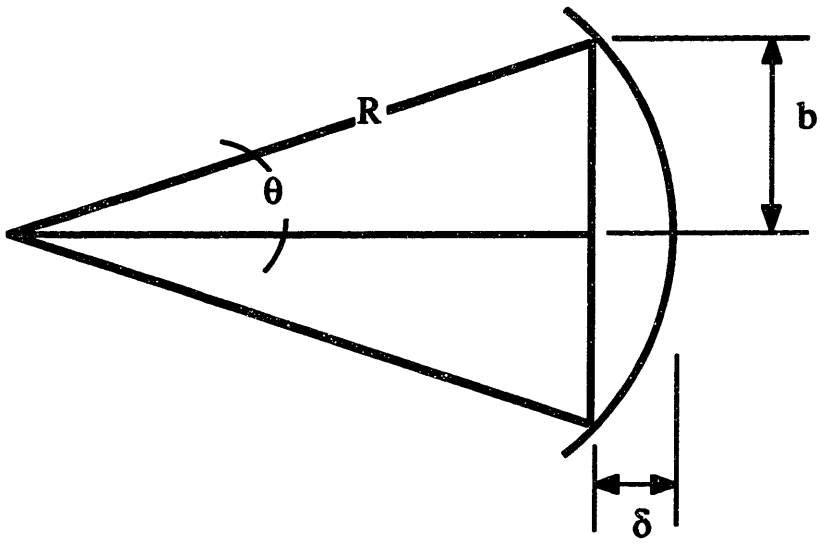


$$R = \frac{\delta^2 + b^2}{2\delta} \qquad \theta = \sin^{-1}\frac{b}{R} \qquad L = R * 2\theta$$

**Figure 4-6.** Method of determination of buckled (arc) length of single fibril.

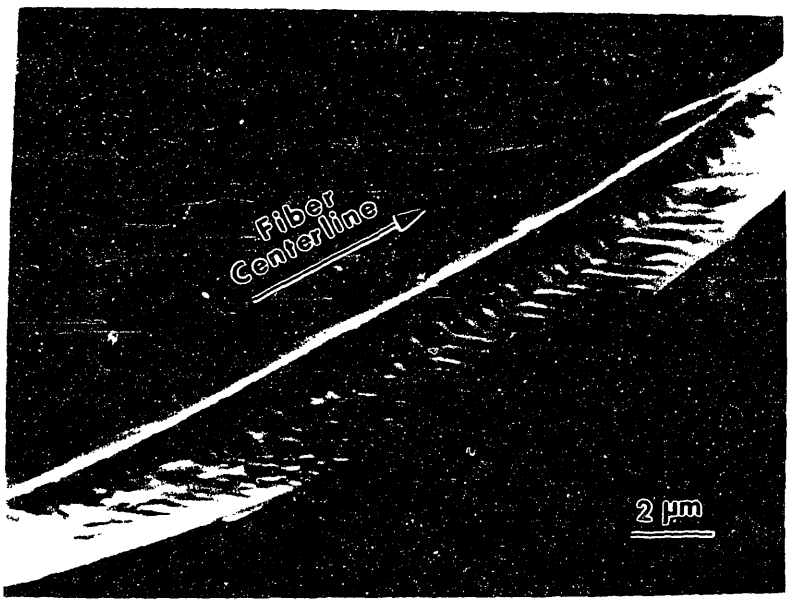


**Figure 4-7.** SEM Micrograph of Arrays Of Buckled Rows In The Skin of a PBO Fiber Which Has Been Peeled Off The Core.

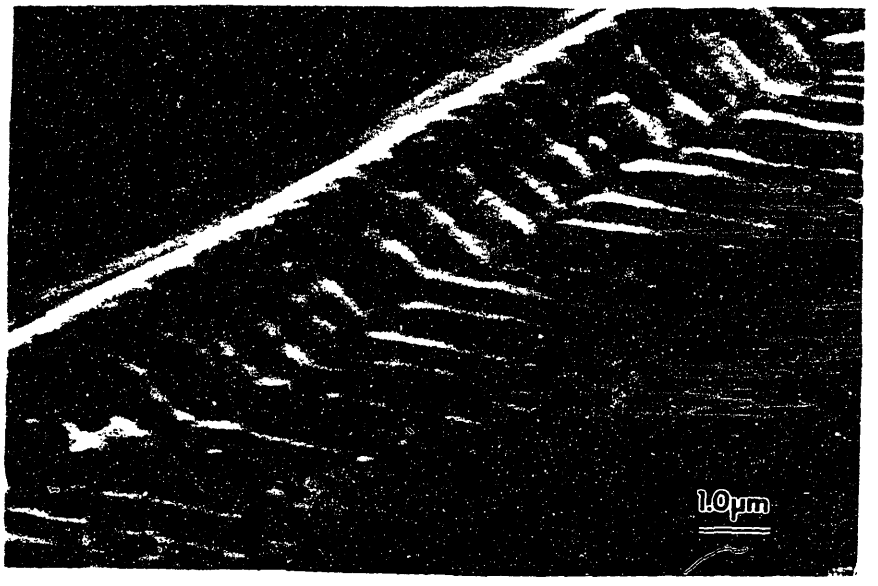


**Figure 4-8.** Same as Above, Higher Magnification.

## 4.3. Results and Discussion

Table 4-1 presents the results of the Euler buckling analysis applied to Kevlar® 49 and PBO fibrils. The single mode buckling length was found by the sheath peeling and R4 method for Kevlar® and PBO respectively. The fiber compressive strength is calculated by multiplying the single fibril strength by the ratio of fiber to fibril area (number of fibrils).

It is clear that the predicted load for compressive failure overestimates the measured one. A number of reasons are available to explain this:

1) The size of the fibril is not single valued. Actually a distribution of fibril diameters exists.

2) The compressive deformation in the fibrils is not elastic as assumed in the Euler analysis. The analysis is based on stability considerations and is valid for long slender columns. The slenderness ratio of the fibrils is very low, on the order of about 20 - 25. (The slenderness ratio is the length of the column ,L,divided by the radius of gyration ,R, of the cross section in the plane of buckling). The value of the slenderness ratio above which Eulers formula applies can be estimated by

$$\left(\frac{L}{R}\right)_{min} = \sqrt{\frac{\pi^2 E}{\sigma_{ucs}}}$$

**Table 4-1.**
Euler Analysis of Single Fibrils Using
Sheath Peeling and R4 methods.

| Fiber | Fibril Diameter (nm) | Fibril Length (nm) | Comp. Modulus (GPa) | Calc. Compress Strength (MPa) | Measd Compress. Strength (MPa) |
|---|---|---|---|---|---|
| Kevlar 49 | 160±20 | 1510±220 | 90 | 620±205 | 345±35 |
| PBO-1 | 220±30 | 1400±200 | 40 | 620±276 | 207±35 |

Note: Measured Compressive Strength From Tensile Recoil.
(Fiber Diameters: Kevlar® 49=12um, PBO-1=18um)

which conservatively assumes that non -linear behavior occurs after compressive failure. For Kevlar® and PBO this value is about 50. Examination of Figure 4-9 indicates that the Euler analysis will overestimate the compressive strength for typical fibrils. This overestimation is derived from the fact that crushing is also involved in fibril failure. In order to consider this type of behavior, the compressive stress - strain curve for a single fibril/fiber would have to be known.

The agreement of the model with other experimental observations is encouraging: it postulates that the kink band initiates on the fiber surface, where the low degree of lateral support leads to small critical buckling loads. Kink bands do start on the fiber surface as can be seen in Figure 4-10.

Perhaps the best use of the model is in the investigation of processing variations on the mechanical properties of a fiber of given composition. One such study was conducted on four types of PBO fibers, each subjected to different processing conditions. The fibers were simultaneously subjected to an $O_2CF_4$ plasma for 20 minutes to obtain the fibril buckling length. Figures 4-11 to 4-14 are SEM micrographs of the pits created from plasma etching. The lengths of the pits are similar to kink lengths in PBO fibers measured by others[23].

Split fibers were used to measure fibril diameters. Table 4-2 presents the results of the analysis. Due to the aforementioned uncertainty in the plasma etching method (section 3.5.3), the predicted fiber compressive strengths are given on a ranked basis only. The fibril peel and R4 methods measure actual buckling entities and hence are more accurate. Nonetheless, the relative measurement provided by the plasma etching is effective: the predicted rank in the compressive strength is in excellent agreement with the measured one, indicating the merit of the model.

Despite the fact that the model is useful in ranking ultimate compressive strength of single fibers, its utility in determining the absolute ultimate compressive strength may be limited. To improve the model would require knowledge of fibril compressive stress-strain behavior, the nature of fibril-fibril interactions, and the compliance coefficient for axial lateral interaction, $S_{z\theta}$. Identification of these items would allow for more exact modeling of these complex systems.

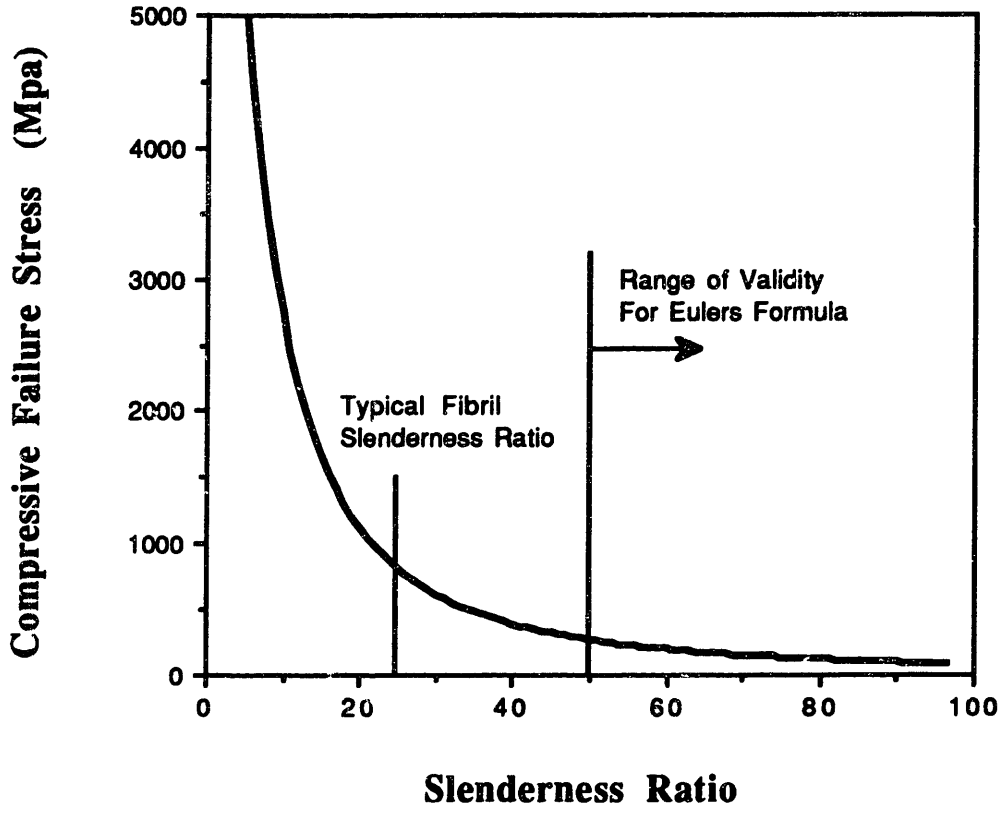


**Figure 4-9** Eulers Curve for Fiber with Compressive Modulus of 89.5 GPa

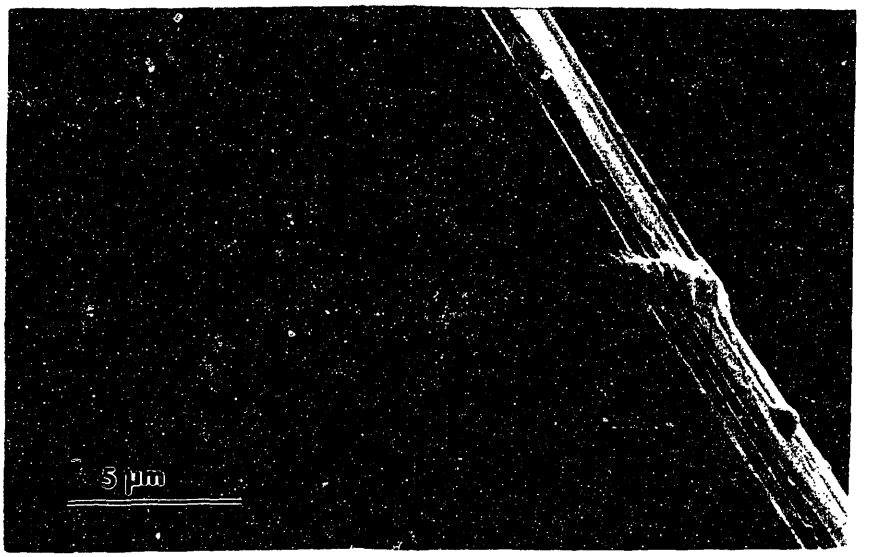


**Figure 4-10** SEM Micrograph of Kink Band Initiating on Exterior of PBO Fiber

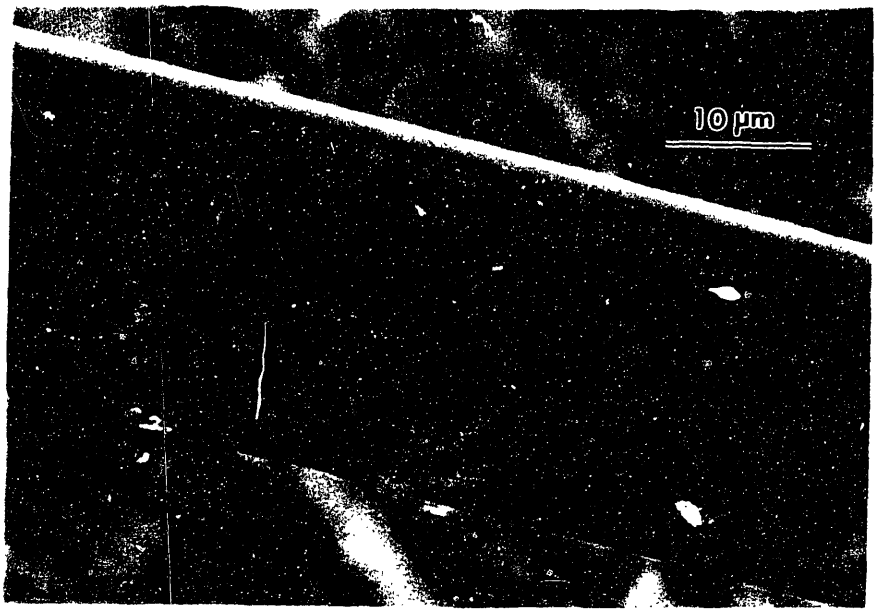


**Figure 4-11**. SEM Micrograph of Pits Along Kink Boundary in Plasma Etched PBO Fiber.

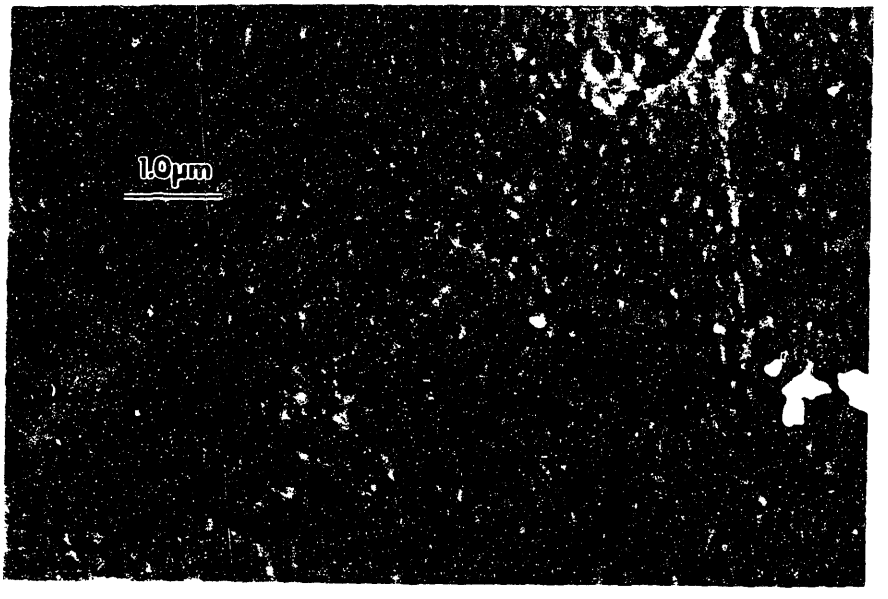


**Figure 4-12**. SEM Micrograph of Pits Along Kink Boundary in Plasma Etched PBO-6 Fiber.

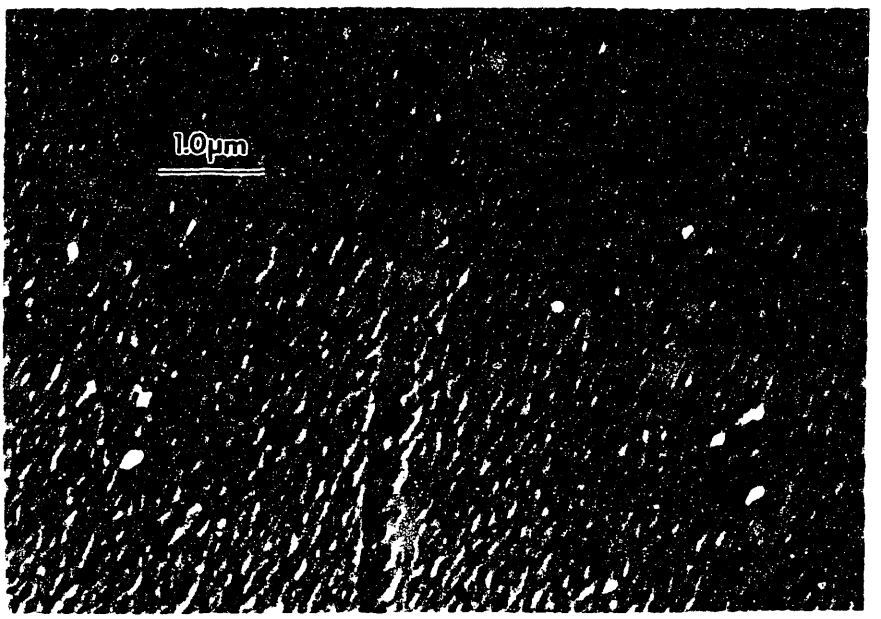


**Figure 4-13.** SEM Micrograph of Pits Along Kink Boundary in Plasma Etched PBO-5 Fiber.

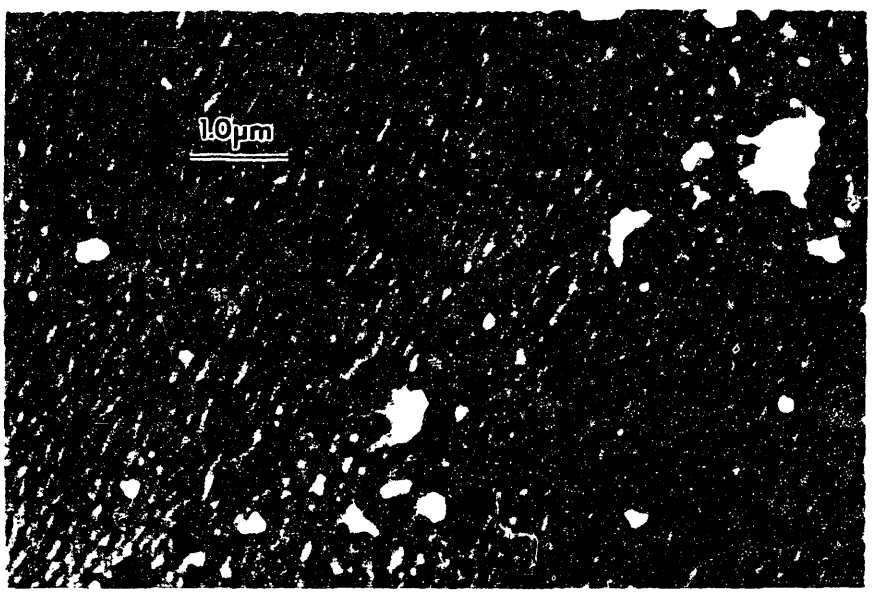


**Figure 4-14.** SEM Micrograph of Pits Along Kink Boundary in Plasma Etched PBO-4 Fiber.

**Table 4-2.**
Euler Analysis of Single Fibrils Using Plasma Etching Method For Single Mode Buckling Length.

| Fiber | Fibril Diameter (nm) | Fibril Length (nm) | Measured UCS [MPa (ksi)] | Measured Rank in UCS | Predicted Rank in UCS |
|---|---|---|---|---|---|
| PBO-3 | 220 | 590 | 152 (22) | 4 | 4 |
| PBO-4 | 230 | 350 | 324 (47) | 1 | 1 |
| PBO-5 | 180 | 360 | 214 (31) | 2 | 2 |
| PBO-6 | 250 | 660 | 165 (24) | 3 | 3 |

# Chapter 5. Improving Fiber Compressive Strength

## 5.1. Methods of Improvement

### 5.1.1. Chemical Methods

As discussed in Chapter 4, several researchers have recognized that buckling of polymer chains[3] or fibrils[19] is responsible for the compressive failure in high performance polymer fibers. Others predicted that the introduction of lateral covalent bonding between chains would delay buckling and improve the compressive strength. Bhattacharya *et. al.* introduced flourene moieties into Poly(p-phenylene benzobisthiazole) (PBT) fibers[2] for lateral crosslinking while Chuah *et. al.* crosslinked PBT copolymers via labile methyl groups[24]. Both studies showed minimal improvement in compressive strength; in fact, the axial tensile strength was reduced because of the reduction in packing ability. The lack of improvement from interchain crosslinking is further indication that compressive properties are governed by fibrillar morphology, thus a method to laterally reinforce the fibrils was sought.

### 5.1.2. Rigid Coatings

Examination of the model developed in section 4.2 indicates that lateral restraint of a column will increase its critical buckling load. If the model is modified to include lateral, elastic support, as shown in Figure 5-1, the critical buckling load is[25]

$$P_{cr} = \frac{\pi^2 EI}{L^2}\left(n^2 + \frac{\beta L^4}{n^2 \pi^4 EI}\right) \qquad (5.1)$$

where $\beta$ is the modulus of the elastic foundation and all other variables are as given previously. By choosing a high modulus material for the foundation, the buckling load can be increased by

$$\left(\frac{\beta L^4}{n^2 \pi^4 EI}\right) * 100 \qquad (5.2)$$

percent. Note, however that by increasing $\beta$ there is a condition at which $P_{n=1} < P_{n=2}$ i.e

$$1 + \frac{\beta L^4}{\pi^4 EI} = 4 + \frac{\beta L^4}{4\pi^4 EI} \qquad (5.3)$$

$$\frac{\beta L^4}{\pi^4 EI} = 4 \qquad (5.4)$$

Thus if only stability is considered, the maximum increase in single mode buckling strength is 500 percent. Since kinking initiates on the fiber exterior where

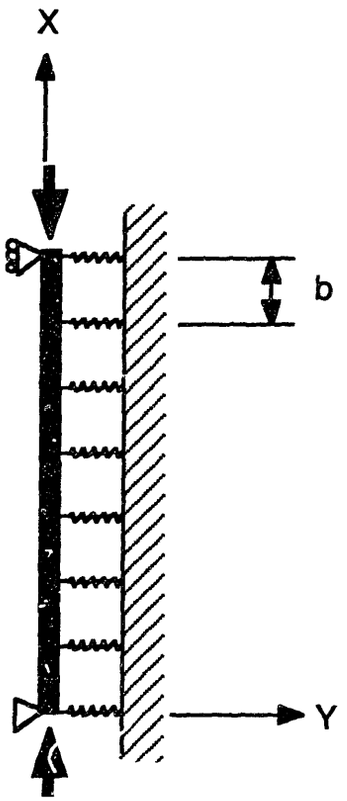


**Figure 5-1.** Modification of Fibril Model To Consider Lateral Support By An Elastic Foundation. Each spring has a spring constant k. The modulus of the foundation, $\beta$, is given by $\beta = k / b$

the lateral support is minimal, application of a rigid coating to the fiber surface should increase the compressive strength.

### 5.1.2.1. Coating Selection

Equation 5.1 indicates that any material of finite modulus applied to the fiber should increase its compressive strength. However, the coating itself also carries an axial load so a high modulus is desirable to prevent buckling of it. Strength of materials calculations indicate that the coating will carry an axial load given by

$$P_c = P_{applied} * \left( \frac{E_c A_c}{E_c A_c + E_f A_f} \right) \qquad (5.5)$$

where P is force, E is the modulus, A is the cross sectional area and the subscripts c and f refer to the coating and fiber. This shows that coating materials with high moduli are desirable for lateral support (equation 5.1) but they will acquire a higher proportion of the applied axial forces which may lead to their premature buckling.

A schematic of some of the forces on the coating is given in Figure 5-2. The lateral forces come from fibrils attempting to buckle and the hoop forces are derived from the lateral expansion of the fiber. If the coating and the fiber have different thermal expansion coefficients, residual

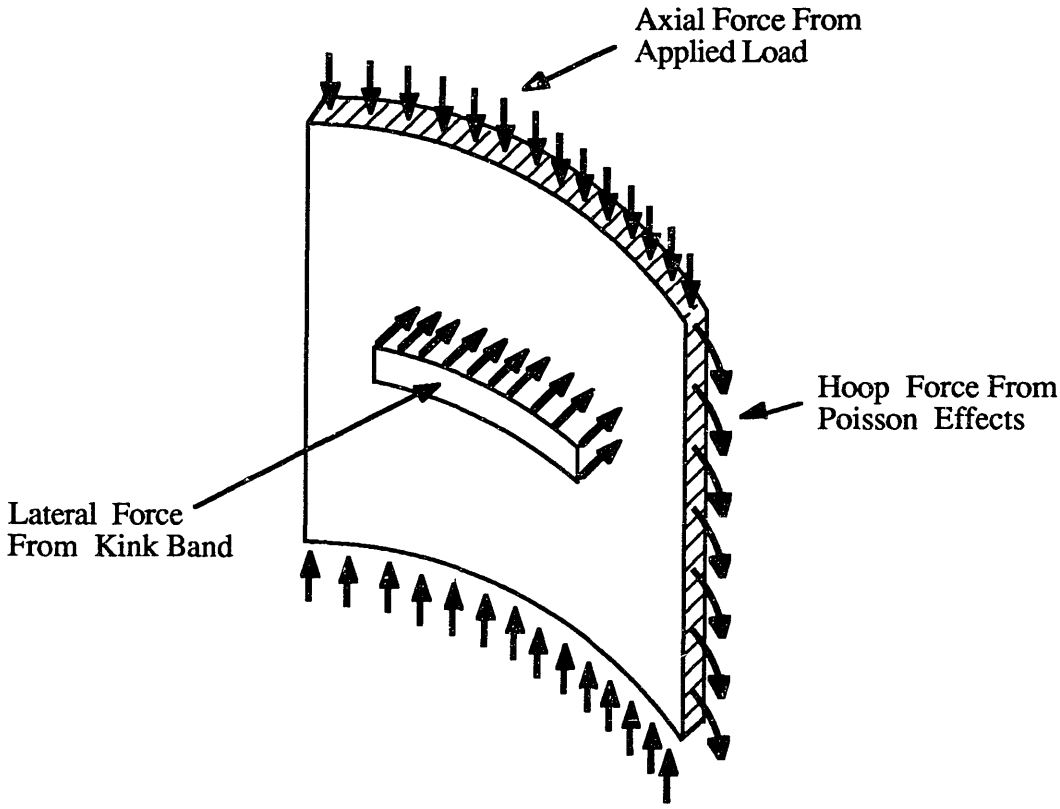


**Figure 5-2.** Schematic of Forces on Thin Rigid Coating Applied to Fiber (Fiber Not Shown).

stresses will result from temperature excursions. These forces are given by

$$P = \frac{(\alpha_f - \alpha_c)\,\Delta T}{\frac{1}{E_c A_c} + \frac{1}{E_f A_f}} \qquad (5.6)$$

where $\alpha$ is the thermal expansion coefficient, $\Delta T$ is the change in temperature and the subscripts are as defined previously. The appropriate stress can be found by dividing by either the fiber or coating cross sectional area. To minimize the stress, coating materials with thermal expansion coefficients similar to those of the fiber are desirable.

Good adhesion between the coating and the fiber surface is necessary for the reinforcing concept to be effective. If the outer fibrils are not constrained and can start to bend, they will buckle. Similarly, the coating derives lateral support from the fiber only if the two are well adhered. Absent good adhesion, the coating idea is not effective.

A rigid coating also reduces the fiber radial coefficient of thermal expansion (CTE) which is very large, typically greater than 40 ppm/°C. Since the fiber transverse modulus is so low, the high modulus coating restrains the fiber. Finite element calculations performed by Jao[26] show that for a fiber with a transverse modulus of 4 GPa and a coating thickness of 1 percent of the fiber diameter the radial CTE

is significantly reduced with high modulus coatings. These results are shown in Figure 5-3. Figure 5-4 shows that the reduction in radial CTE is a strong function of the fiber transverse modulus. It also indicates that the axial CTE will not be reduced by the rigid coating because of the higher fiber modulus in that direction. Finally, finite element calculations show that even if the coating cracks axially at 45° intervals around the fiber circumference, the radial CTE increases only by a few percent if the coating remains well adhered to the fiber surface.

## 5.2. Experimental

### 5.2.1. Coating Deposition

High modulus ceramic coatings were applied to fibers using physical vapor (PVD) deposition techniques as outlined in United States Patent 5021258[27]. The PVD process is unique in that it permits deposition of high melting point ceramic materials without subjecting the polymer substrate to appreciable temperature differentials. A Temescal electron beam evaporator with special fixtures designed to rotate the fibers for uniform coating deposition was used. The ceramic used for most of the study was aluminum oxide (alumina or $Al_2O_3$) The bulk properties of alumina obtained from the literature[28] are given in Table 5-1. The properties listed are for crystalline $\alpha$-alumina which was the evaporant source.

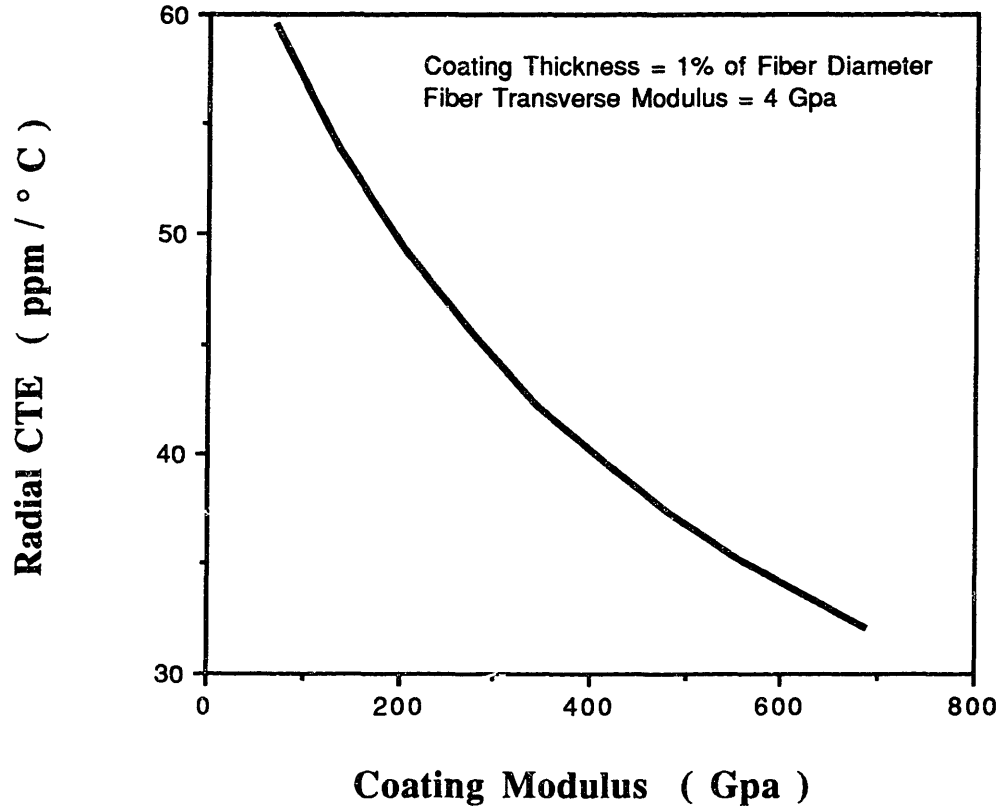


**Figure 5-3.** Radial CTE as a Function of Coating Modulus Generated By Finite Element Model.

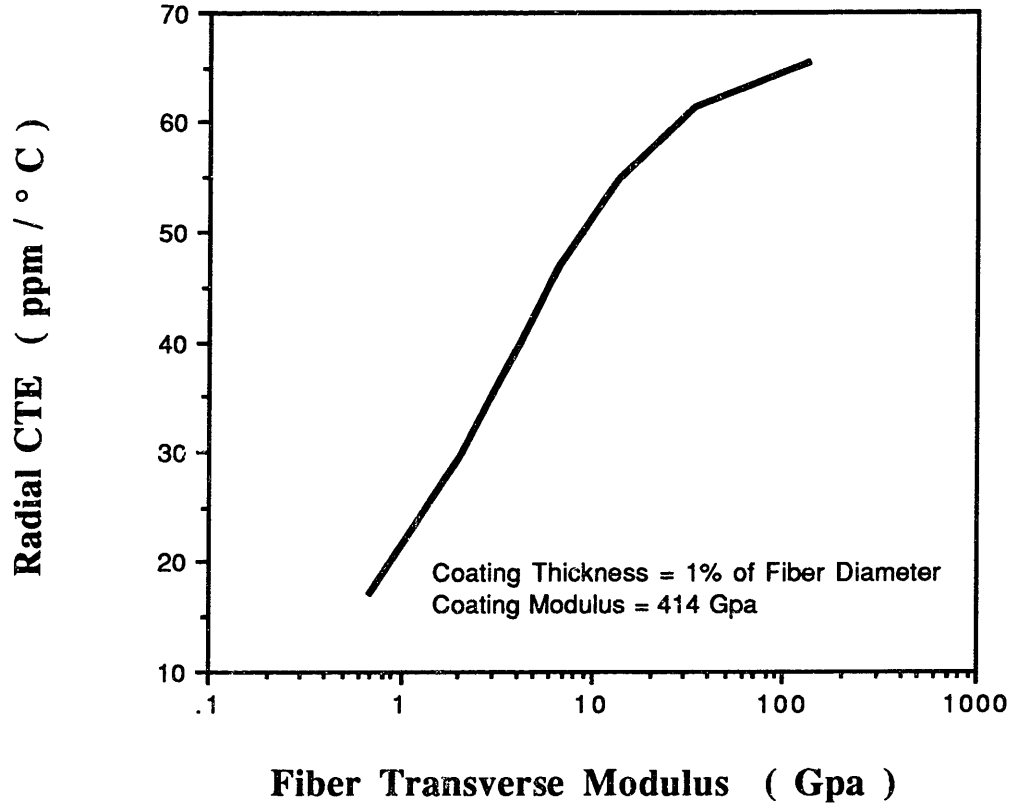


**Figure 5-4.** Radial CTE as a Function of Fiber Transverse Modulus Generated By Finite Element Model.

However, X-ray diffraction studies indicated that the deposited material was amorphous. SEM observations of the coatings showed they are homogeneous and uniform both axially (Figure 5-5) and circumferentialy (Figure 5-6).

Figure 5-6 shows an alumina coated glass fiber which was frozen in liquid nitrogen and fractured to produce the surface shown. (A glass fiber was used for this illustration because it is easier to prepare.) The coating thickness on glass slides placed adjacent to the fibers during deposition was used to measure the coating thickness on the fibers. The glass slides provided a flat substrate on which a Dektak® profilometer was used to measure the thickness.

### 5.2.2. Property Evaluation

The compressive strength of coated fibers was evaluated by the tensile recoil test. Flexural properties of coated fibers were determined with the single fiber three point bending test. The radial thermal expansion was observed by using a hot stage in an SEM and measuring the change in fiber diameter with heating. Fibers were dried under vacuum prior to testing to avoid dimensional changes from water expulsion. No composites were made with coated fibers as the many thousands of fibers required for a single specimen could not be coated by the batch electron beam process in reasonable times periods.

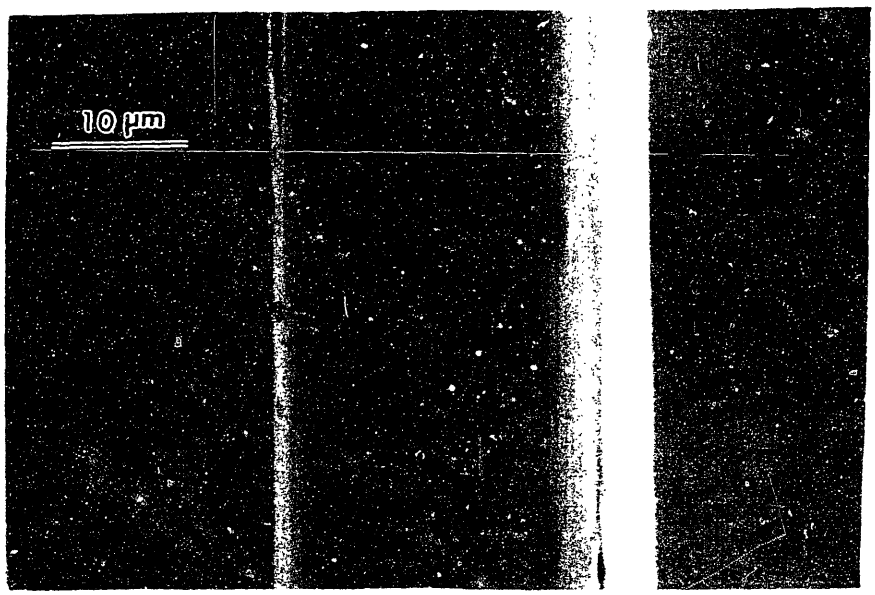


**Figure 5-5**. SEM Micrograph of Alumina Coating on PBO Fiber Applied by Physical Vapor Deposition. Coating is Smooth and Homogeneous.

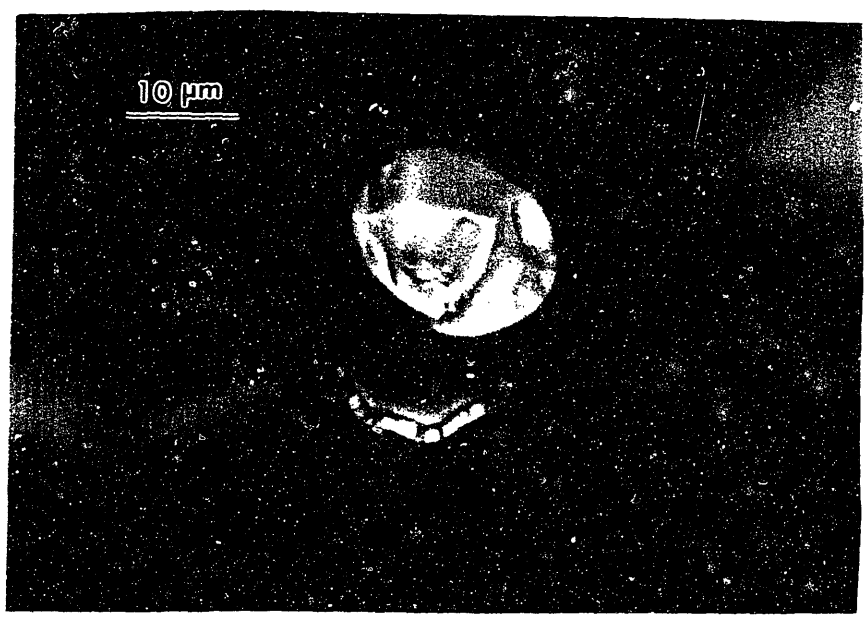


**Figure 5-6**. SEM Micrograph of Alumina Coating on Glass Fiber Applied by Physical Vapor Deposition. Coating is Uniform Around Fiber Circumference.

**Table 5-1.**
Mechanical Properties of Alumina
Used For Rigid Coating on Fibers

| | |
|---|---|
| Modulus Of Elasticity | 372 GPa (54 Msi) |
| Compressive Strength | 2.4 GPa (350 Ksi) |
| Tensile Strength | 207 MPa (30 Ksi) |
| Coefficient of Thermal Expansion | 7 ppm/°C |

## 5.3. Results and Discussion

### 5.3.1. Effect of Coatings on Fiber Strength

A range of coating thicknesses was applied to both single PBO and Kevlar® 49 fibers[29]. The ultimate compressive strength versus coating thickness for PBO is given in Figure 5-9.

A linear fit correlates well to the data and the line extrapolates back almost exactly to the compressive strength of the uncoated fiber. The compressive strength of the PBO is more than doubled with a coating thickness of 8000 Å. SEM micrographs of failed coated fibers are given in Figures 5-7 and 5-8. Kink bands are discernible beneath the failed coating and the excellent adhesion is apparent. In fact, the adhesion was so good that attempts were made to coat more traditional engineering polymers to be certain that good adhesion was not unique to high performance polymer fibers. Alumina coatings were successfully applied to flat plates of poly-styrene, poly-carbonate, poly-methylmethacrylate, poly-styrene acrylonitrile and poly-ethylene: adhesion was excellent in all cases. A study was initiated to investigate the source of the adhesion and preliminary secondary ion mass spectrometry and x-ray photoelectron spectroscopy data indicate that primary valence bonding existed between the alumina and the polymers. The studies were not fully conclusive as the minute volume fraction of ceramic/polymer interface caused analytical difficulties. It is suspected

that the atomic oxygen which is known to be present during electron beam evaporation of alumina[30] is responsible for the formation of primary bonds.

The improvements in compressive strength for Kevlar® 49 were not as consistent as those observed for PBO. Sometimes the Kevlar® fibers would show large increases in compressive strength and other times almost none. Eventually it was determined that the reason for the inconsistent behavior was poor adhesion between the fiber and coating. Morgan[31] et al found large amounts of residual sulfur and sodium in Kevlar® while Penn[32] et al found stearic and palmitic acids. We confirmed the presence of sulfur and sodium by a neutron activation study. The stearic and palmitic acids are used as lubricants during processing and their presence creates a weak boundary layer on the fiber surface which inhibits coating adhesion. PPTA fibers made without such lubricants were obtained from DuPont and the limited data obtained indicate that improvements in their compressive strength are similar to those observed in PBO.

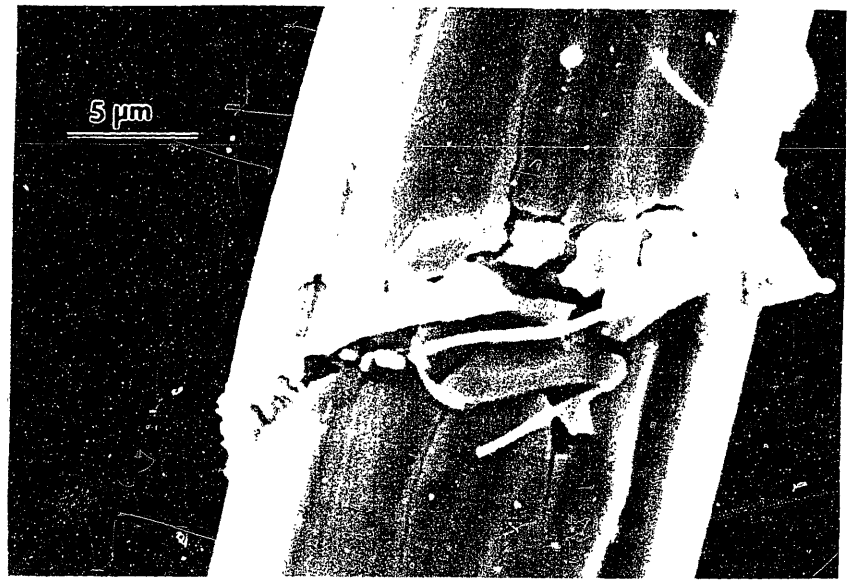


**Figure 5-7.** SEM Micrograph of Failed Alumina Coated PBO Fiber. Good Adhesion of Coating is Evident.

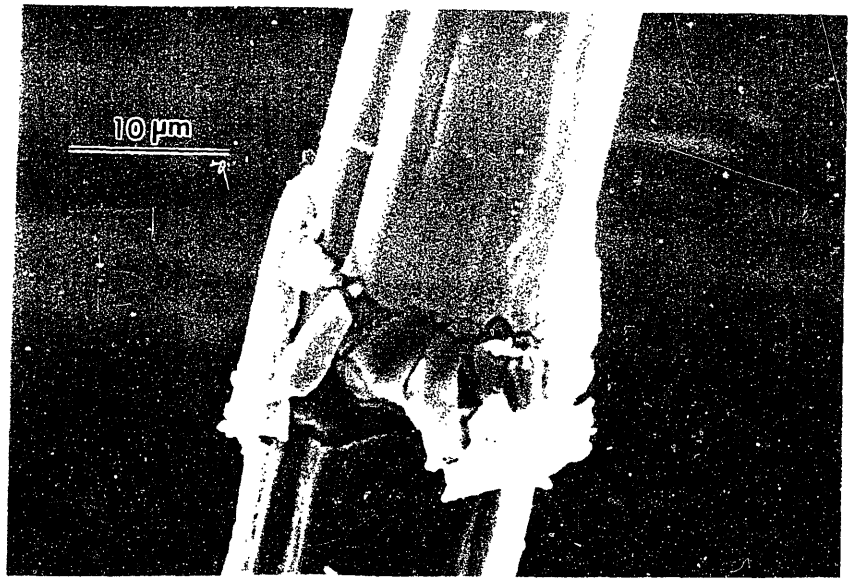


**Figure 5-8.** SEM Micrograph of Failed Alumina Coated PBO Fiber. Good Adhesion of Coating is Evident.

Since the rigid ceramic coating is brittle, some concern existed that, in tension, its fracture would cause premature failure of the fiber. Figure 5-10 shows that this does not occur. The data indicate no significant difference between the two.

Well adhered rigid ceramic coatings significantly improve the compressive strength of PBO fibers. This improvement is not accompanied by a decrease in tensile strength as was found in the other studies cited[2,24]. It has also been observed by Chang[33] that cracking in the coating caused by tensile loading or by thermal cycling does not degrade the improvement in compressive strength provided the coating remains well adhered.

### 5.3.2. Effect of Coatings on Fiber CTE

Uncoated fibers and coated fibers were heated in a SEM from 25° C to 400° C at about 25° C/min. A micrograph of a coated fiber at 400°C is given in Figure 5-11. The axial cracking is a result of the large radial expansion of the fiber; the critical cracking temperature is dependent on coating thickness. This cracking at elevated temperatures can also be used to indicate adhesion: a poorly adhered coating will show a single axial crack and spall free while a well adhered one will give multiple cracks, while remaining in place.

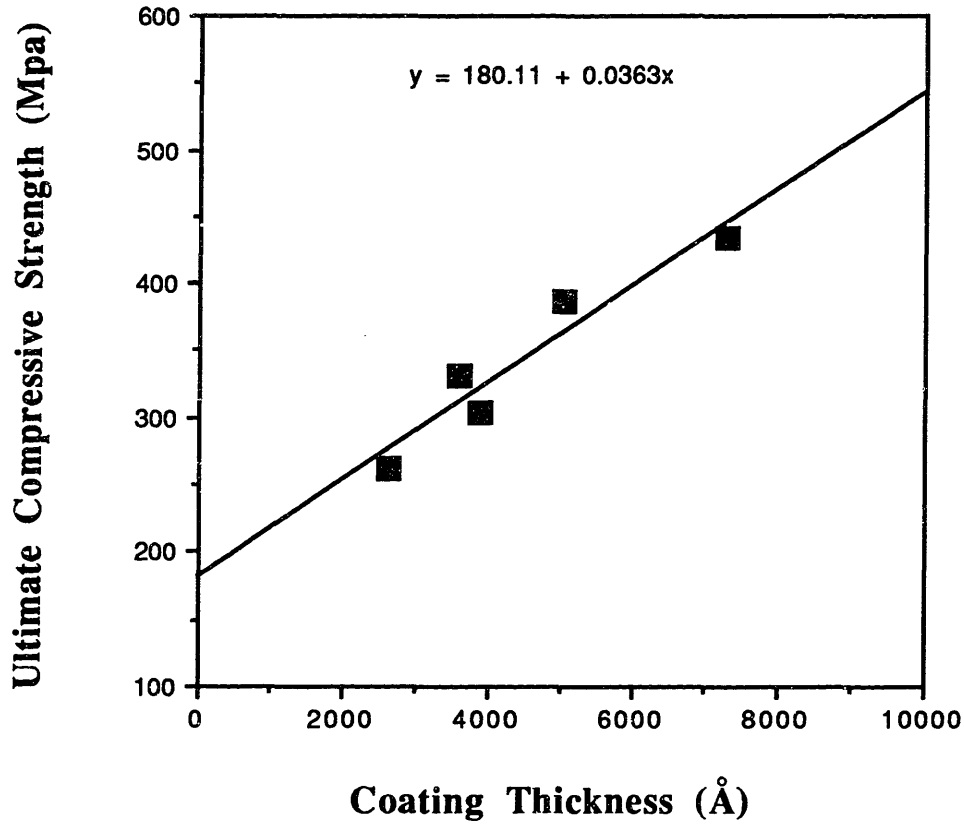


**Figure 5-9.** Ultimate Compressive Strength versus Alumina Coating Thickness For PBO Fibers.

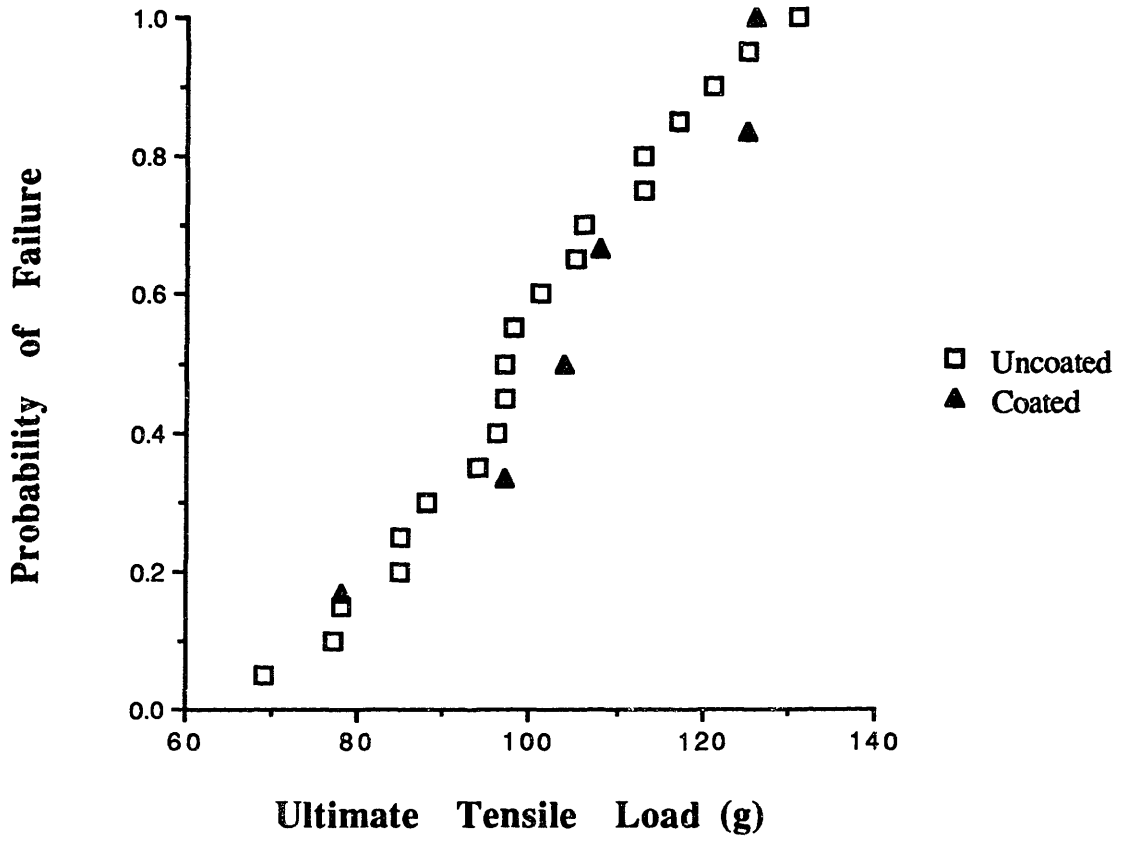


**Figure 5-10.** Cumulative Distribution Function Of Ultimate Load For Uncoated and Alumina Coated PBO Fibers in Tension.

Figure 5-12 presents the percent change in fiber diameter for PBO fibers, both uncoated and coated with 6000Å (3% of fiber diameter). All data were fit linearly by the least squares method. The slope of the lines m, divided by 100, is the radial CTE in ppm / °C. The coated fibers show a reduction in radial CTE by a factor of 2. Cracking begins in the coated fibers at about 250° C, but no substantial deviation in expansion is observed, in good agreement with the finite element predictions.

Figure 5-13 presents the percent change in fiber diameter for Kevlar® 49 fibers both uncoated and coated with 3500Å (3% of fiber diameter). The more than three fold decrease in radial CTE is more dramatic in the Kevlar® system. Since less axial cracking was observed in the Kevlar® system its adhesion was worse than that of the PBO. This indicates that good adhesion is not as critical in reduction of radial CTE's as it is for improvement of compressive strength. It is encouraging to observe that a problem long associated with high performance polymer fibers, large radial CTEs, can be solved by the application of rigid coatings.

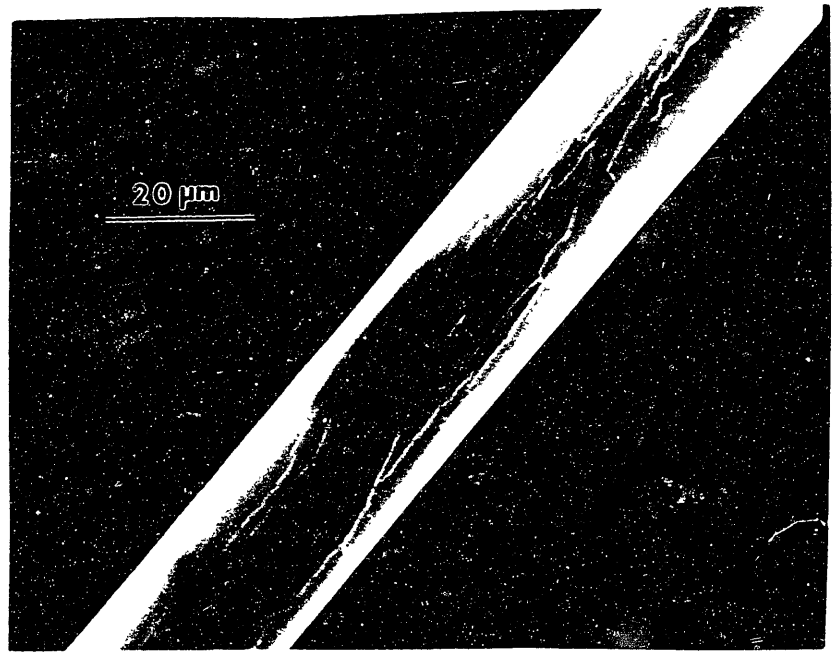


**Figure 5-11.** SEM Micrograph of Alumina Coated PBO Fiber Heated In-Situ to 400°C.

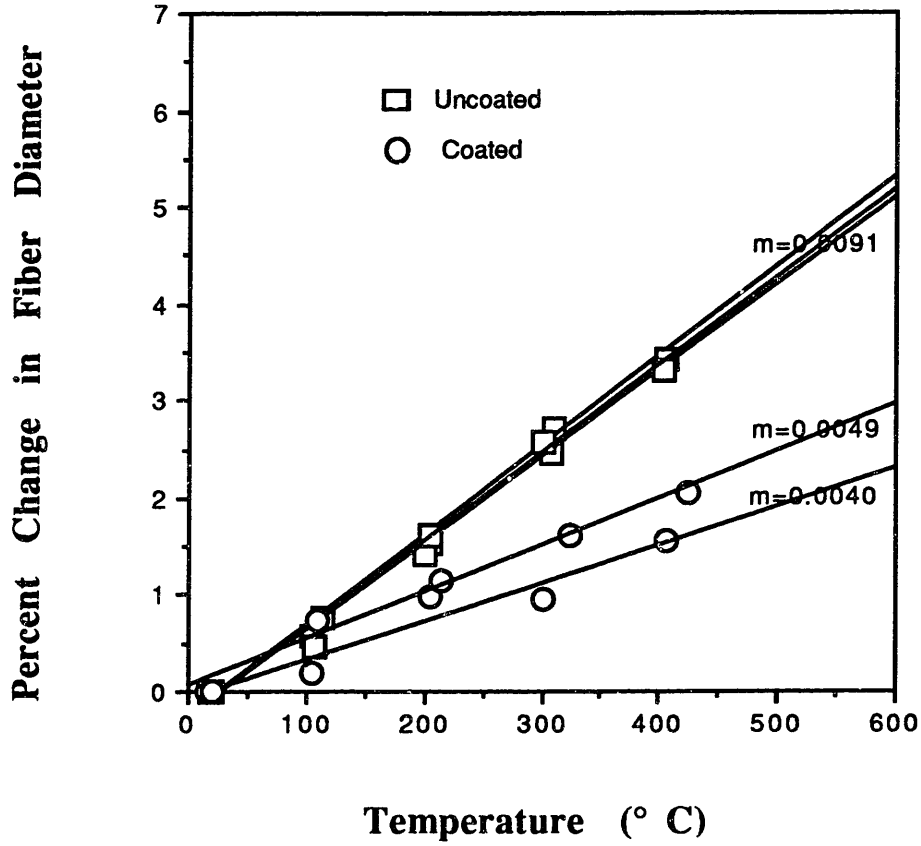


**Figure 5-12.** Percent Change in Fiber Diameter With Temperature For Uncoated and Alumina Coated PBO Fibers. (m=slope).

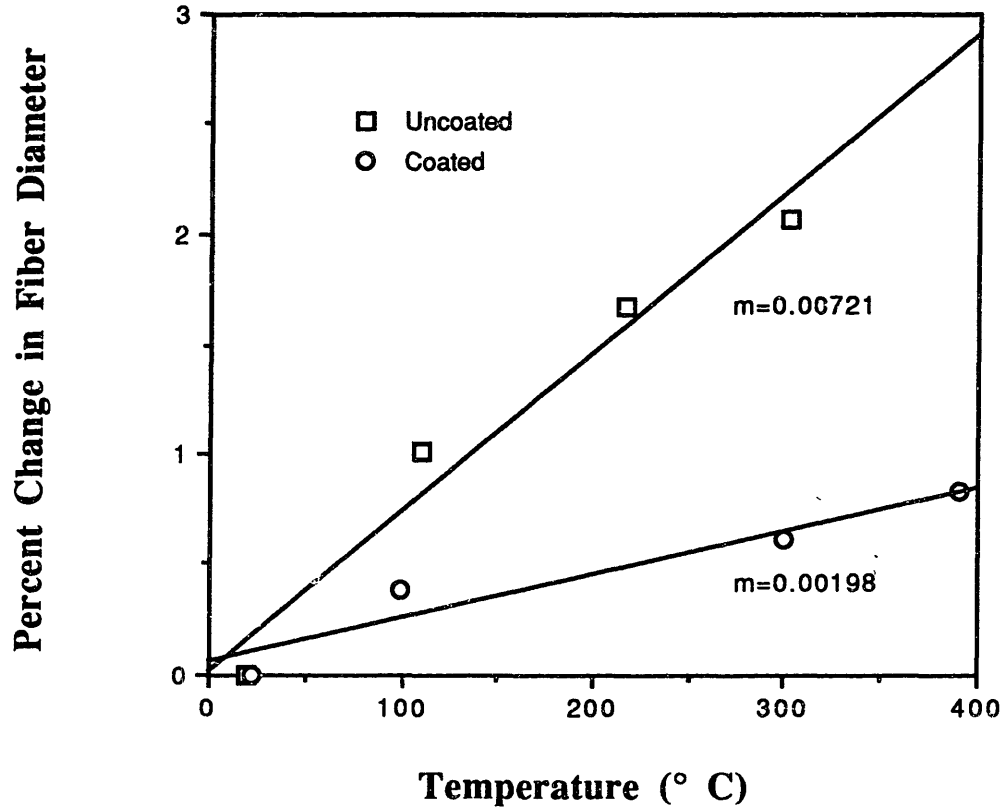


**Figure 5-13.** Percent Change in Fiber Diameter With Temperature For Uncoated and Alumina Coated Kevlar® 49 Fibers. (m=slope).

### 5.3.3. Effect of Coatings on Flexural Behavior

The presence of a high modulus material distant from the neutral axis of a beam will increase its flexural rigidity EI. This produces lower deflections for the same load. Figure 5-14 is a flexural load-deflection plot for PBO fibers uncoated and coated with 8000 Å of alumina. The increase in rigidity of the coated fiber shows the improvement in flexural behavior. The increase can also be used to determine the in-situ modulus of the coating by use of a transformed section method in which the coating is virtually transformed into a mechanically equivalent area of the fiber. Recognizing that the axial force on the coated fiber cross section must be zero it follows

$$E_c \int_c y\,dA + E_f \int_f y\,dA = 0 \qquad (5.7)$$

If n, the modulus ratio, is defined as

$$n = \frac{E_c}{E_f} \qquad (5.8)$$

then equation 5.7 can be rewritten as

$$\int_c n\,y\,dA + \int_f y\,dA = 0 \qquad (5.9)$$

where A is area and y is the distance to the neutral axis. Equation 5.9 indicates that the position of the neutral axis remains unchanged if each area element of the coating is multiplied by n. Hence, the coated fiber can be modeled as a single material (fiber) with a moment of inertia

$$I = \frac{\pi (d + 2 n t)^4}{64} \qquad (5.10)$$

where d is the fiber diameter, and t is the coating thickness.

The anisotropic nature of the high performance polymer fibers creates uncertainties in the appropriate fiber modulus to be used in equation 5.8 since three different moduli are involved: $E_{t,fiber}$, $E_{c,fiber}$ and $E_{coat}$. Instead, three point bend tests were conducted on coated glass fibers since glass is an isotropic material. A plot of the load-deflection data for a 24 um diameter E-glass fiber is given in Figure 5-15. From the slope of the linear fit, we can find the moment of inertia from equation 3.22 since the modulus and span are known. Equation 5.10 can then be solved for the modulus ratio since the coating thickness is known. Using this method, the in-situ modulus of the coating was found to be 310 GPa (45 Msi) to 345 GPa (50 Msi) which is in reasonable agreement with the modulus of the bulk material ( 372 GPa [54 Msi]) reported previously.

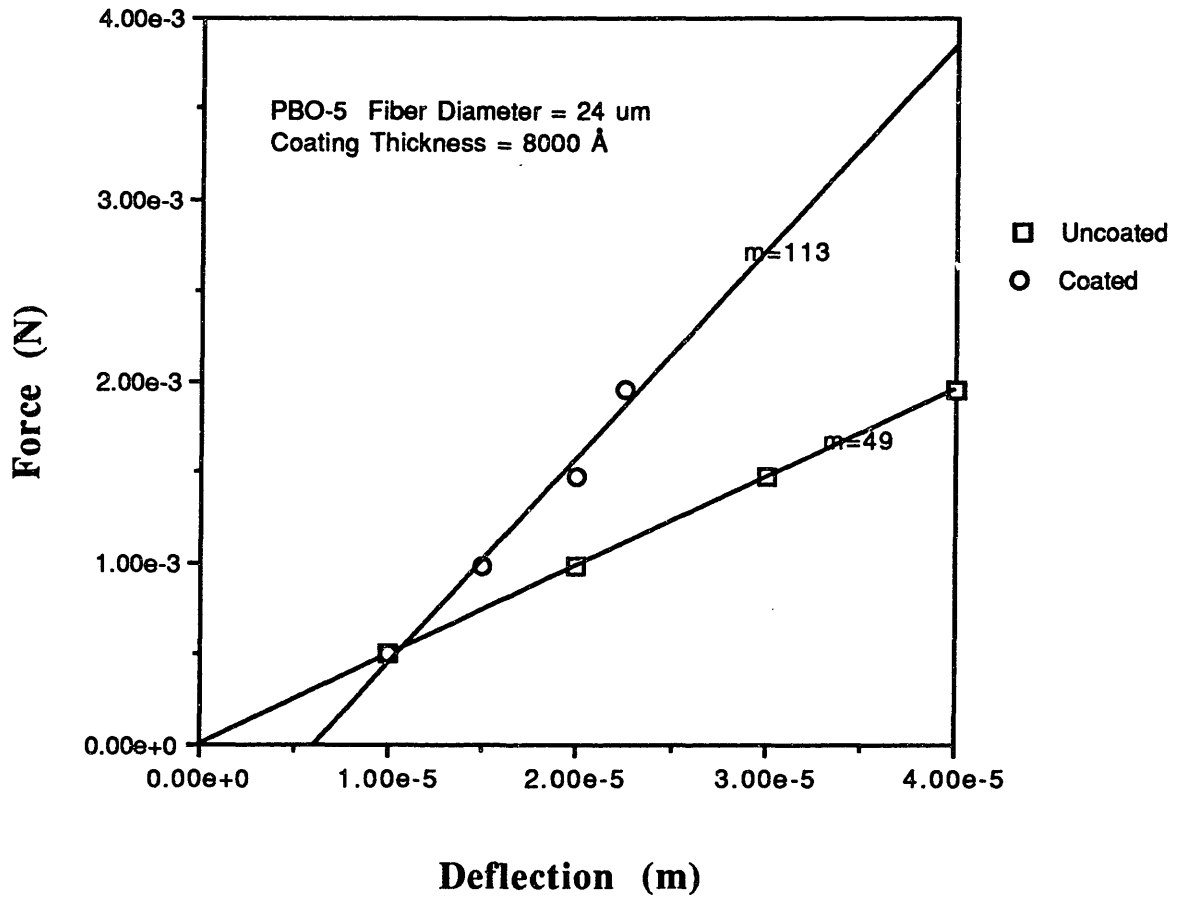


**Figure 5-14.** Load Deflection Plot For Uncoated and Alumina Coated PBO-5 Fibers. (m=slope).

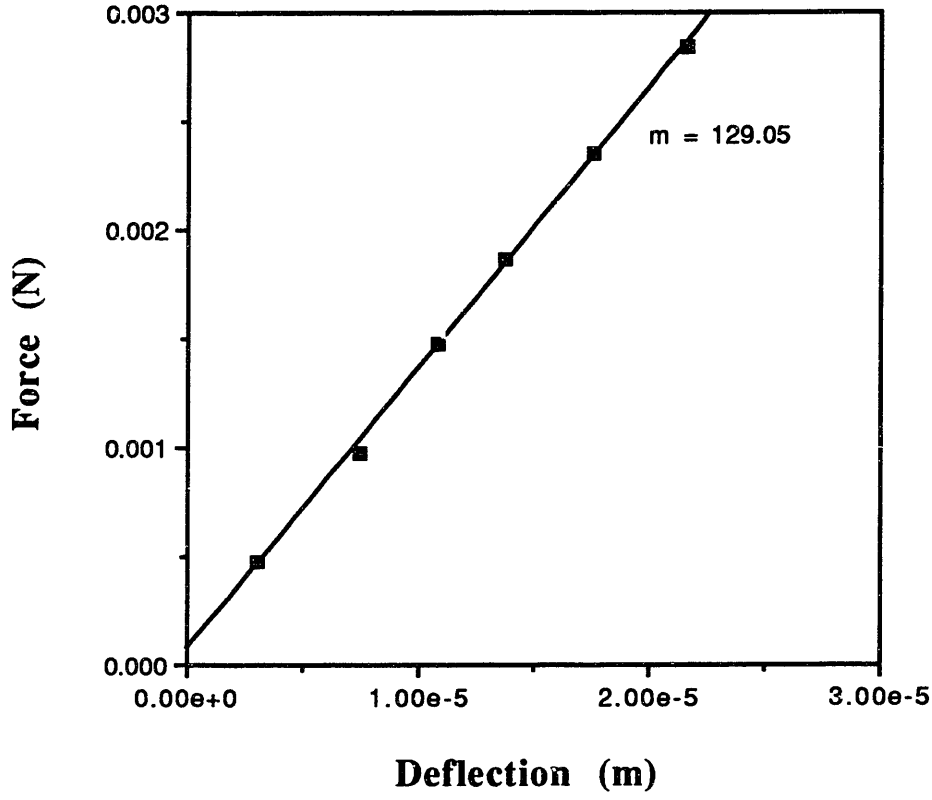


**Figure 5-15.** Load Deflection Plot For an Alumina Coated E-Glass Fiber. (m=slope).

### 5.3.4. Mechanism of Improvement

The motive for the rigid coating was to provide lateral restraint of the outer fibrils and thereby increase the compressive strength of the fibers. It is possible, however, that the high modulus coating simply takes load away from the fiber thus allowing the system to sustain a higher load; a rule of mixtures (ROM) type of behavior. This alternate explanation of its action had to be explored.

#### 5.3.4.1. Rule of Mixtures

Equation 5.5 shows that for a coating of 4000Å thickness and 345 GPa Modulus on a fiber of 20 um diameter and 70 GPa compressive modulus (typical of PBO) approximately 29 percent of the load is borne by the coating. Since the strength of the fiber is increased by more than 80 percent at this thickness it is unlikely that a ROM type of behavior is occurring. Alternatively, it is possible to find a coating modulus value such that the system does follow a ROM. Using equation 5.5, an analysis was conducted to examine stress levels in the fiber and in the coating for different coating moduli. The study chose coating properties and then found the load required to reach the ultimate stress level in either the fiber or the coating for a given coating thickness. Figure 5-16 displays the results: measured values

of coated fiber ultimate compressive strength and the data generated by using equation 5.5. (On the figure, the coating modulus, Ec, and strength, Sc, are given for each line in GPa.) The analysis shows that in order to obtain behavior similar to that which was measured, the coating must have a modulus of more than 950 GPa (138 Msi) and a compressive strength of 3.8 GPa (551 Ksi). These are much higher than their known, in-situ values. Much closer to the known values is the set represented by the triangle (Δ), which is far below the experimentally measured data. This casts strong doubt on the relevance of the simple rule of mixtures to the system; either a more complicated rule is required , or the true action of the coating is to provide the stabilizing constraint against buckling. The latter appears more probable.

### 5.3.4.2. Lateral Restraint

Implementing a model to validate the lateral restraint hypothesis is difficult. If we assume that the coating restrains kink formation until it fails (coating failure controls), then the appropriate model would be a thin cylindrical shell supported on its interior by an elastic foundation. This shell would be loaded as in Figure 5-2. We could also attempt to model the outer fibrils as columns supported by an elastic foundation as depicted in Figure 5-1.

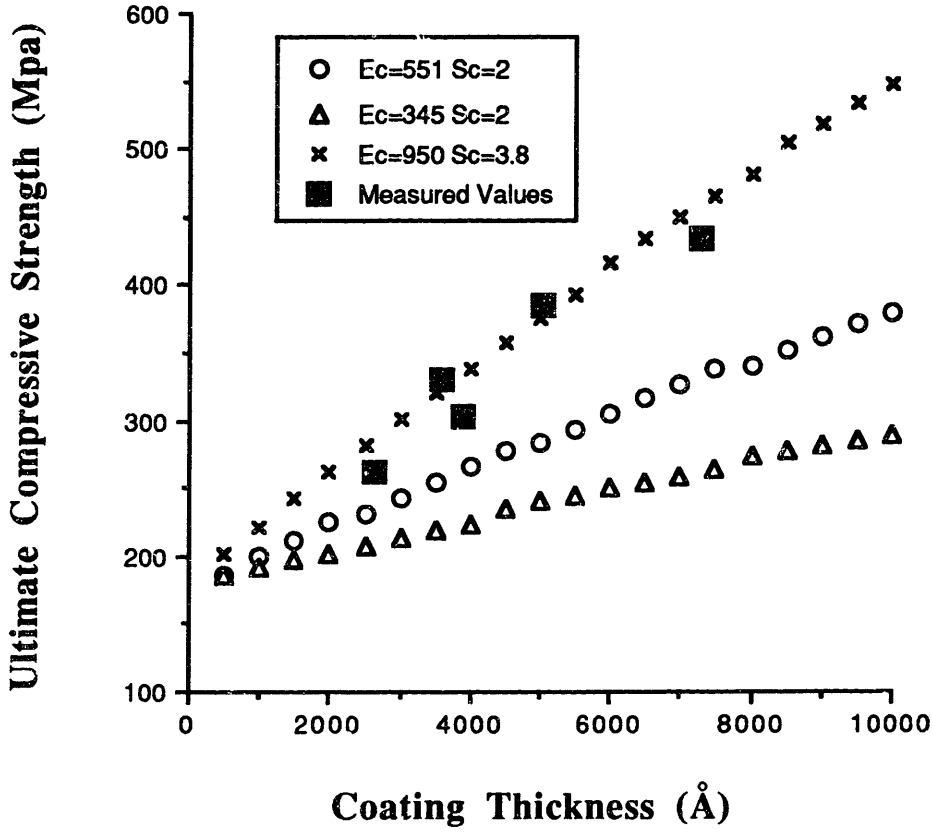


**Figure 5-16.** Ultimate Compressive Strength vs. Coating Thickness: measured data and values calculated from rule of mixtures (Ec=Coating Modulus, Sc=Coating Compressive Strength) Units:Gpa

Unfortunately, since the restraint conditions and the magnitudes of the lateral forces imposed by the kinks are unknown, predicting the coated fiber behavior based on these models would degenerate into seeing how the starting assumptions play out in the results. It would not be conclusive.

At this point it is believed that the correct explanation of the coating effect is its stiffening of the surface against compressive buckling. This derives from several factors. There is abundant evidence that the compressive failure mechanism is fibril buckling, which is why chemical crosslinking between polymer chains is ineffective. The buckling initiates kink bands at or near the surface of the fiber and a stiff coating on the surface delays it. The coating functions even though tensile preloading or temperature excursions may crack it extensively; the reinforcement action is very localized, consistent with the dimensions of fibrils. Good adhesion of the coating is essential to its function, since it is attached to only one side of the fibril rather than entirely surrounding it.

### 5.3.5. Effect of External Stresses on Residual Strength of Coated Fiber

Since the coating is brittle, in work done by Chang[33] it was cracked extensively, either by loading the fiber in tension to near its breaking point or by heating it such that

significant differential thermal expansion occurred. The fibers used PBO with a baseline compressive strength of about 80 Mpa as measured by the tensile recoil method. The fibers were coated with various uniform thicknesses of ceramic and pulled to about 80% of their breaking load, producing uniformly spaced circumferential cracks as shown in Figure 5-17. Then these were tested in tensile recoil with the results shown in Figure 5-18. Within the scatter of the data, the precracked fibers showed the same strength improvement as did the uncracked ones, especially with the thicker coatings. Though cracked, the coating remained well adhered to the fiber, with no spalling evident, and the width of the cracks was very small, of the order of 2500 Å. This crack width is much less than the 15,000 Å length of the buckling fibril elements in PBO observed by us but on the same order of buckling fibrils observed by others[23]. The elements remain constrained by the coating despite the cracks. This suggests that it is the larger scale buckling elements that we observed which control the compressive strength.

Using coated fibers from the same population, a number were exposed to elevated temperatures: 150°C and 250°C for 30 minutes in air. No special steps accompanied cooling; the specimens were simply removed from the oven. Heating caused the fibers to contract axially and expand radially, both at rates different from the ceramic coating, and the result was

a series of axial cracks as seen in Figure 5-11. No spalling occurred and the cracked coating continued to inhibit the radial thermal expansion of the fiber. When these fibers were tested in tensile recoil, the compressive strengths were nearly the same as for the uncracked coated fibers as shown in Figure 5-19. The axial cracks were narrow, about 2500 Å, and followed a circuitous path on that scale of dimension; they were not perfectly straight. The small gap and the irregular path apparently combined to preserve the constraining action of the coating on the fibril elements.

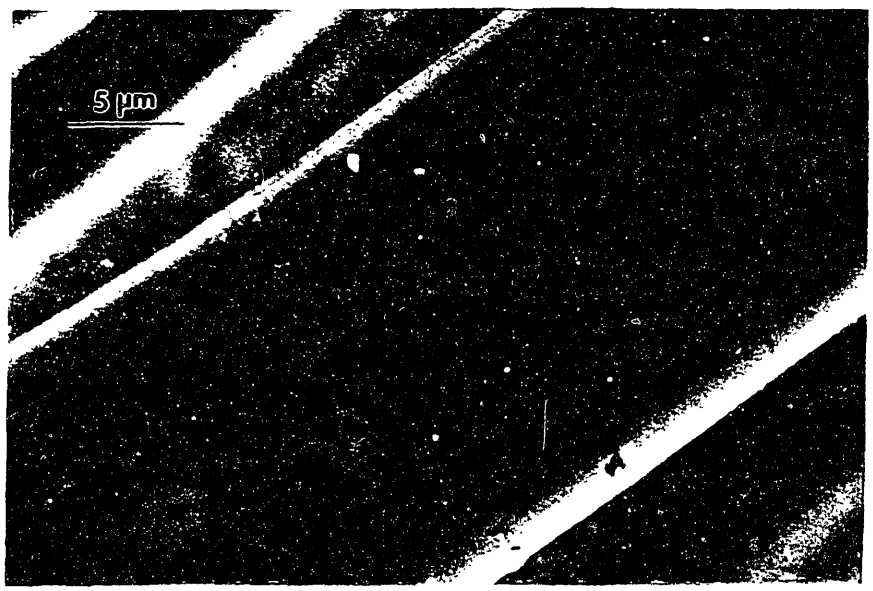


**Figure 5-17.** Circumferential Cracks in Coating on PBO Fiber From Tensile Loading.

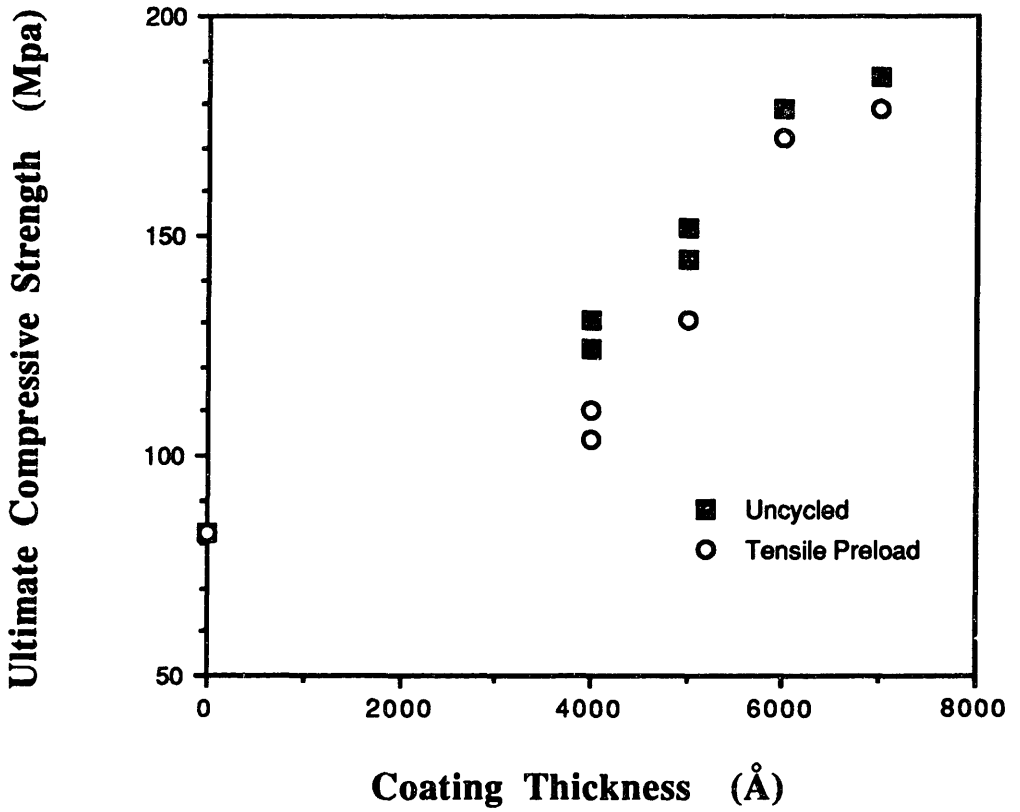


**Figure 5-18.** Ultimate Compressive Strength vs. Coating Thickness in PBO Fiber both Unloaded and After a 60g Tensile Preload.

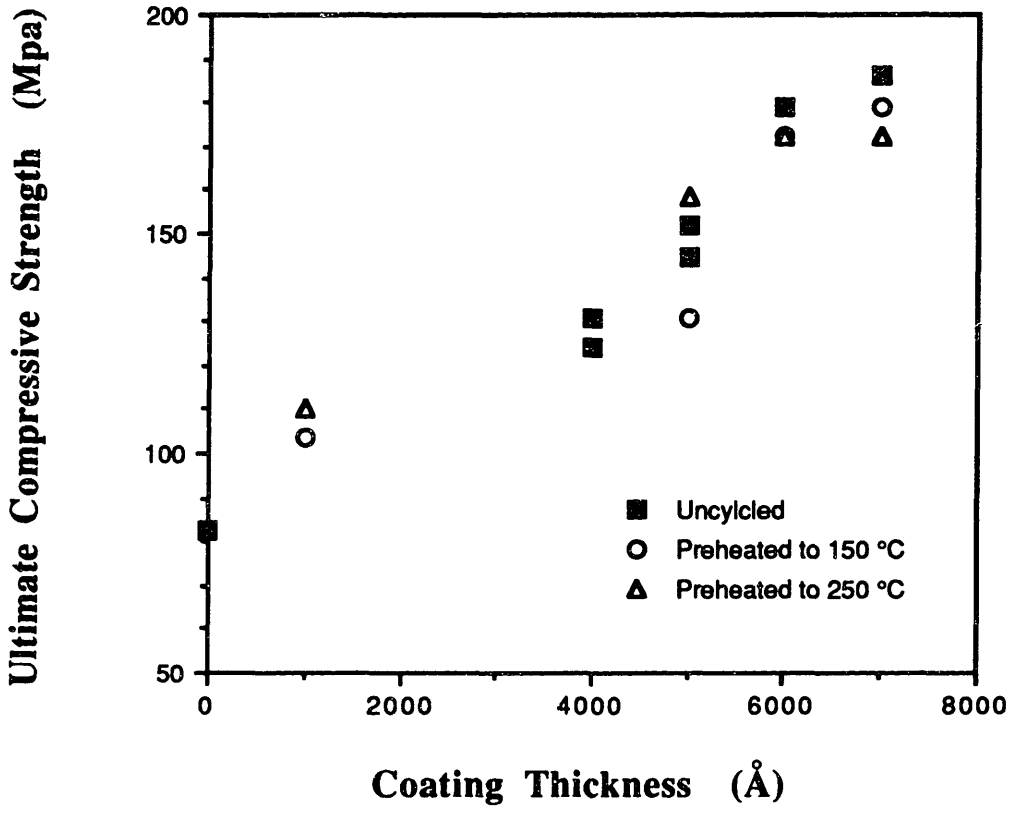


**Figure 5-19.** Ultimate Compressive Strength vs. Coating Thickness in PBO Fiber Before and After Heating in Air..

# Chapter 6. Conclusions

New methods have been developed to evaluate the mechanical properties of high performance polymer fibers. A device which simplifies recoil testing by symmetrical cutting of the fiber was made and it gives a more accurate measurement of the axial compressive strength. Load spikes created by non-symmetric cutting are nearly eliminated in Kevlar® fibers and greatly reduced for PBO fibers.

To evaluate the transverse strength of single fibers, a test was developed in which an opening mode crack is propagated axially in the fiber. The crack initiation force normalized by the fiber diameter provides a measure of a transverse fiber mechanical property. The loads involved are extremely small and difficult to measure. To determine critical crack propagating force an instrument which operates with dead weights was constructed. Gas bearings were used on all translational parts to minimize frictional forces. Because the test does not measure the true transverse tensile strength the numbers obtained have been termed the Transverse Strength Index (TSI). The TSI can be used to evaluate changes in processing parameters. No relationship between the TSI and the fiber compressive strength is evident.

Values of the TSI obtained for fibers with strong intermolecular bonding (aramids) are similar to those without (PBO) suggesting that the lateral properties are more likely based on interfibrillar than intermolecular strength.

A modification to the transverse testing apparatus enables three point bending of single fibers. Load deflection curves are generated by adding incremental weights and measuring the corresponding deflection with a video micrometer. Analysis shows that shear effects are minimal and basic elasticity is valid. The equations for bending of a material of circular cross section with different tensile and compressive moduli were derived. They are complex and were solved both numerically and graphically. Isotropic glass fibers were tested to check the performance of the device. The values for the glass modulus were in excellent agreement with the published ones. High performance fibers had compressive moduli that were less than their tensile ones. The ratio of compressive to tensile moduli is sensitive to processing conditions: for Kevlar® 29 Ec/Et is 0.94 while for Kevlar® 149 it is 0.31. PBO fibers processed under different conditions showed similar effects: ratios of Ec/Et ranged from 0.15 to 0.87. Future bending work should focus on shorter spans to examine shear effects. A four point bending test has been developed; with it a single fiber can be tested to compressive failure, thus replacing the cumbersome recoil test.

The modeling of fiber compressive behavior through a simple buckling of the fibrils has been successful. The fibril diameters are determined from SEM observation of fibers split with a micromanipulator. The fibril compressive modulus is assumed to be that of the fiber as obtained from the three point bend test. The fibril buckling lengths have been determined in several ways: plasma etching, buckled peels and the R4 effect. The model overestimates fiber compressive strength but it is useful in ranking the compressive behavior in fibers of the same composition subjected to processing variations which alter their fibrillar morphology.

The model, coupled with the observation of external kink band initiation, suggested that the fiber compressive strength could be improved by the application of rigid exterior coatings. When alumina was applied to the fiber surface, using physical vapor deposition, the fiber compressive strength improved significantly. The increase is linear with coating thickness from about 1000 Å to 8000 Å. The observed improvement exceeds that predicted by the rule of mixtures, indicating that the coating does restrain fibril buckling and does not simply carry load away from the fiber. The coating also reduces, by a factor of 2, the radial coefficient of thermal expansion of the high performance fibers. Cracks in the coating from tensile preloading or from high temperature

exposure do not significantly degrade the improved compressive performance.

Further work should be done to examine effects of different coatings (of both higher and lower moduli) on fiber compressive, flexural and thermal characteristics.

# Appendix

Error In Single Fiber
Bending Experiments

The potential for error in the single fiber three point bending experiments is significant. Inaccurate measurements in deflections and load are both sources of error but, as exemplified in Figure 3-23, the largest is in the fiber diameter evaluation. Since the flexural properties are related to the moment of inertia which is fourth order dependent on the diameter, small errors tend to propagate quickly. Hence, it is critical that the fiber diameter is measured accurately. It is also imperative that the cross section of the fiber is uniform along its length. This can be a significant problem in experimental fibers made in batch processing. A good illustration of the potential error caused by nonuniform cross sections is given in Figure A-1, which shows the calculated compressive modulus for a series of PBO fibers from the same lot. The scatter is large and unacceptable. Figure A-2 shows the calculated compressive modulus for the same group of fibers after they have been screened in an SEM: fibers with a nonuniform cross section over their test length have been omitted. The scatter is minimized and the calculated compressive modulus statistically significant. It.is evident then, that careful execution of single fiber three point bending can yield useful data. For a thorough discussion on this topic the reader is referred to [15].

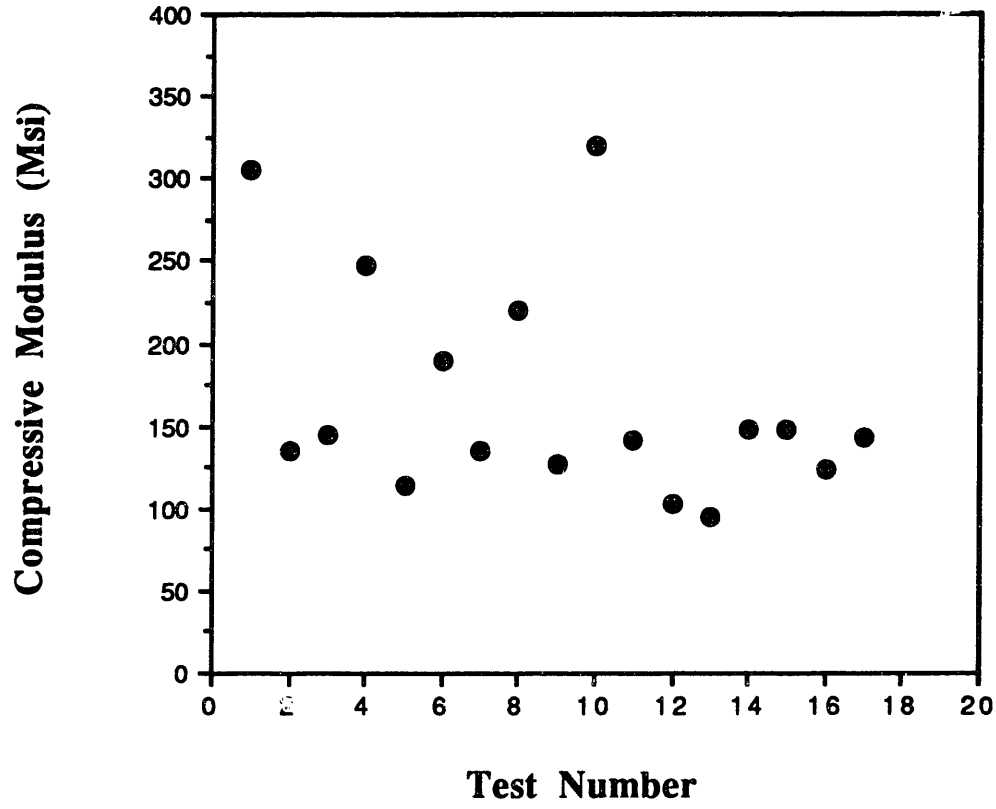


**Figure A-1.** Variation in compressive modulus for PBO fibers of the same lot. Fibers with nonuniform cross sections are included..

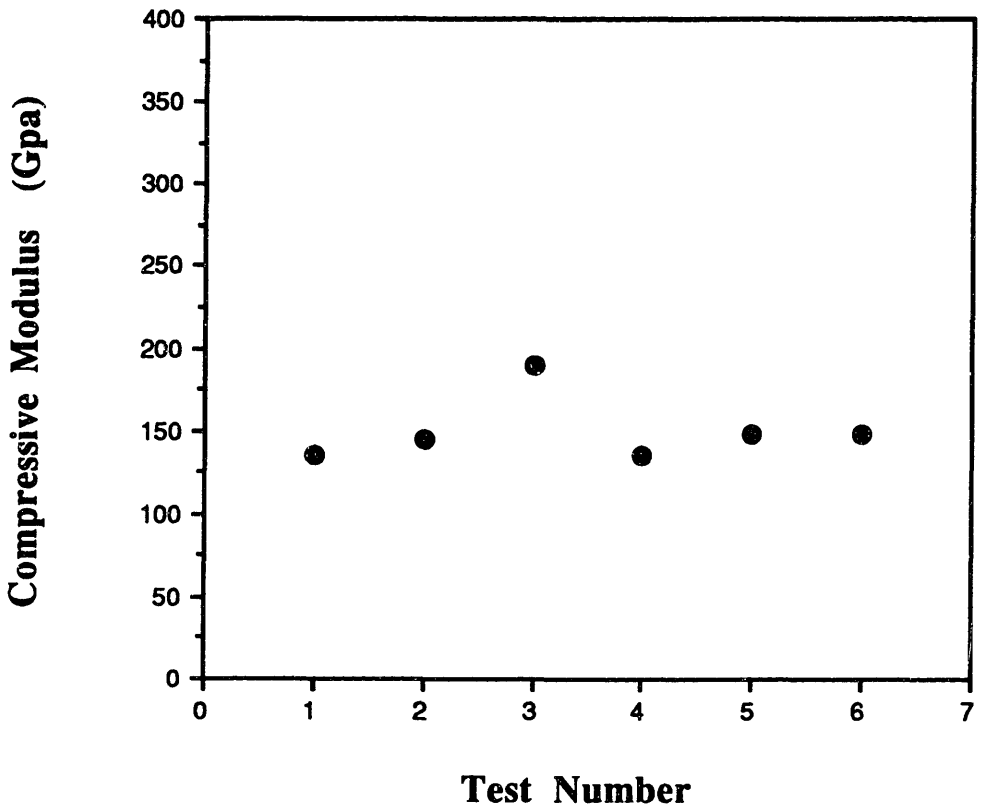


**Figure A-2.** Variation in compressive modulus for PBO fibers of the same lot. Fibers with nonuniform cross sections have been omitted..

# References


1 Chatzi, E.G. and Koenig, L.J., Polym.-Plast. Tech., **26**, 229 (1987)

2 Bhattacharya S., Chuah, H.H, Dotrong, M., Wei, K.H., Wang, C.S., Vezie, D., Day, A., Adams, W.W., Procs. A.C.S. Div. Poly. Mats. Sci. and Eng., **60**, 512 (1989)

3 Deteresa, S.J., Porter, R.S., and Farris, R.J., J. Mat. Sci., **20**, 1645 (1985)

4 Allen, S.R., PhD Thesis, UMASS, 1983

5 Dobb,M.G., Johnson,D.J., and Saville,B.P, J. Polym. Sci., Polym. Symp., **58**, 237 (1977)

6 Likhnitskii, S.G, Theory of Elasticity of an Anisotropic Body, MIR Publishers, Moscow (1981)

7 Sinclair, D.J., J. Appl. Phys., **21**, 380 (1950)

8 Deteresa, S.J., Allen, S.R., Farris, R.J., and Porter, R.S., J. Mat. Sci., **19**, 57 (1984)

9 Deteresa, S.J., Porter, R.S., Farris, R.J., J. Mat. Sci., **23**, 1886 (1988)

10 Allen, S.R., J. Mat. Sci., **22**, 853 (1987)

11 Phoenix, S.L., and Skelton, J., Text. Res. Jour. ,**44**, 934 (1974)

12 Bazhenov, S.L., Kozey, V.V and Berlin, A.A., J. Mat. Sci., **24**, 4509 (1989)

13 Piggot,M.R., Harris,B., J. Mat. Sci., **15**, 2523 (1980)

14 Freeston, W.D., Text. Res. Jour., **42**, 314 (1972)

15 Fahey, M. PhD Theses, MIT In Press

16 Kevlar 49 Data Manual, Dupont

17 Dobb, M.G., Johnson, D.G., and Saville, B.P., J. Poly. Sci, Poly. Phys. , **15**, 2201 (1977)

18 Dobb, M.G.,Johnson,D.J.,and Saville, B.P., Polymer, **22**, 960,(1981)

19 Cohen, Y., and Thomas,E.L., Macromolecules,**21**,433(1988)

20 Kumar,S., SAMPE Quart., Jan. 1989

21 Van den Broek, J.A., Amer. Jour. Phys., **15-4**,309(1947)

22 Pit formation during plasma etching was first observed by Giles Dillingham of Dow Chemical Company as part of an adhesion study.

23 W.W. Adams and D.L. Vezie, 49th EMSA proceedings, 1040, 1991

24 Chuah, H.H, Tsai, T.T, Wei, K.H., Wang, C.S., Arnold,F.E., Procs. A.C.S. Div. Poly. Mats. Sci. and Eng., **60**, 517 (1989)

25 S.P. Timoshenko, J.M. Gere, Theory of Elastic Stability, McGraw Hill, New York (1961)

26 Jao, S., Studies of Interface Properties and Influence of Fiber Coating In Composite Materials, PhD Thesis, MIT, (1989)

27 US Patent 5021258, F.J. McGarry, June 1991

28 HandBook Of Materials Science, **V2**, CRC Press, 1975

29 Spectra polyethylene fibers from Allied Signal were also coated with Alumina. Adhesion to Spectra was excellent. Spectra fibers were not evaluated for compressive strength however because their irregular cross section makes stress calculations very cumbersome.

30 Skvortsov, N.N., Skeber, V.A., Ustinov, Y.K., and Yalyshko, S.V., Sov. J. Opt. Tech., 56 (7) 1989

31 Morgan, R.J., Mones, E.T., Steele, W.J., and Deutscher, S.B., Polym. Prepr., **21-2**, 264 (1980)

32 Penn, L. and Larsen, F., J. Appl. Polym. Sci., **23**, 59 (1979)

33 Chang, B., Effects of Temperature and Tensile Loading on The Compressive Strength Of Ceramic Coated Poly(p-phenylene benzobisoxazole) Fibers, BS Thesis,MIT, (1991)